ABSTRACT

Title of Dissertation: Analysis and Optimization of Input Trajectories for Parameter Identifiability in Multi-Compartment Dynamic System Models

Mahsa Doosthosseini
Doctor of Philosophy, 2021

Dissertation Directed by: Professor Hosam K. Fathy
Department of Mechanical Engineering

This dissertation examines the interconnected problems of (i) analyzing and (ii) optimizing the impact of a multi-compartment dynamic system's input history on the identifiability of its parameters. Identifiability refers to the feasibility and accuracy with which a system's parameters can be uniquely estimated from input-output test data. The shape of a system's input history versus time often affects identifiability. This makes it possible to optimize this input shape for identifiability, in a manner analogous to the use of a cardiac stress test to better diagnose patients with heart disease.

The research in this dissertation makes four contributions to the literature, motivated by the following four practical research questions. First, is it possible to characterize CO_2 gas transport dynamics in a laboratory animal where the peritoneal perfusion of a perfluorocarbon (PFC) is used as a potential treatment for hypercarbia? Second, how does the shaping of chemotherapeutic treatment affect the accuracy with which drug resistance dynamics can be estimated in a partially drug-resistant cancerous tumor? Third, can the dynamic cycling of a lithium-sulfur (Li-S) battery be tailored to maximize the accuracy

with which its parameters are estimated? Finally, can Pontryagin methods from optimal control theory yield fundamental insights into the structure of the ambient temperature cycling trajectory that maximizes the identifiability of a lithium-ion battery model's thermal parameters?

In addressing the above practical research questions, this dissertation navigates a progression of four fundamental topics in the field of multi-compartment dynamic system parameter identification and identifiability. Specifically, the dissertation's examination of peritoneal CO_2 gas transport dynamics highlights and motivates the importance of analyzing multi-compartment dynamic system identifiability. The subsequent examination of the identifiability of drug resistance dynamics in cancerous tumors highlights the degree to which input shaping can negatively affect parameter identifiability. In contrast, the examination of parameter identifiability for Li-S batteries highlights the potential of input shaping to improve identifiability significantly for multi-compartment systems. Finally, the dissertation's examination of thermal battery parameter identifiability highlights the degree to which the fundamental tool of Pontryagin analysis can help gain insight into optimal input shaping for identifiability. In summary, the work in this dissertation explores a progression of fundamental topics in the area of dynamic system parameter identifiability while highlighting the broad applicability of this area to different practical domains.

Analysis and Optimization of Input Trajectories for Parameter Identifiability in Multi-Compartment Dynamic System Models

by

Mahsa Doosthosseini

Dissertation submitted to the Faculty of the Graduate School of the
University of Maryland, College Park in partial fulfillment
of the requirements for the degree of
Doctor of Philosophy
2021

Advisory Committee:
Dr. Hosam K. Fathy, Chair/Advisor
Dr. Joseph S. Friedberg
Dr. Jin-Oh Hahn
Dr. Simona Onori
Dr. Monifa Vaughn-Cooke

Dean's Representative:
Dr. Alisa Morss Clyne

© Copyright by
Mahsa Doosthosseini
2021

Acknowledgments

There are so many that I would like to thank, there is so much that I am thankful for. First, I would like to thank my parent. I would not be who I am today without the love, support, encouragement, and trust of my parents, Mamanam Susan and Babam Gholam Ali. I also have a very special thanks to my spouse, Behzad who is always here for me, for my dreams to help me make them true, and for our life to be beautiful. I am also thankful to my parent in-law, Ozrah and Esmaeil, my sisters and brothers in-law, Elham, Elahe, Shahrzad, Behnam, Reza, Bahram, Mohammad, Shahram, Hossein, Maryam, Zeinab, Zahra and their sweet children for their love and belief. I would also like to thank my family, my aunts and uncles, Farahnaz, Fatemeh, Parastoo, Nasim, Mahnaz, Shahnaz, Sharareh, Soheila, Fariba, Azam, Haniye, Ali Agha, Aghaye Kantouri, Fariborz, Faramarz, Abbas, Habib, Ebi and their wonderful children for their love, kind accompanying and guidance all along my life. I would like to give this moment as a gift to my grandmother, Mamanbozorg, who is not here with us, but she and her true love live forever in my heart.

There is one person who I owe him my gratitude who have made this moment possible for me, and I would like to say a million thank you to him, my advisor and mentor, Dr. Hosam Fathy. His patient guidance, continuous encouragement, and timely criticism have helped me grow both as a researcher and as a person. He has set the

standards high for me through his dedication to teaching and mentoring, and his diligence in scientific writing. I am grateful to my committee members, Dr. Joseph S. Friedberg, Dr. Jin-Oh Hahn, Dr. Simona Onori, Dr. Monifa Vaughn-Cooke and Dr. Alisa Morss Clyne for their insights and critique regarding my doctoral research. I would also like to thank Dr. Christopher Rahn for his guidance and help while pursuing my MS degree in Penn Sate University and for his kind support after my graduation. I am also thankful to all other faculty and staff at the University of Maryland including Majid and Kevin who have taught, advised, or helped me during my graduate school. Having been a part of the COOL lab, I would like to express my gratitude to my COOL colleagues Partha, Michelle, Adillah, Chu, Manuel, Miguel, Tim, Xiaoling, Deba, Zahra and Behzad: Thank you all and hopefully I will get to collaborate with each one of you at some point. Behzad, I can't tell you how excited I am to see you in this great lab because I know that you are going to do some really COOL stuff there. I have special friends back home in Iran, and here in US, and I would like to thank them for their love and support, Elham and Shima, my better than a sister friends, and Meisam, Saman, Hossein, Soheil, Mahsa, Mehrdad, Neda, Hamid, Mohammad and Shadi, and last but not least Melody. Finally, I would like to thank the NSF for their financial support through the identifiability grant.

Table of Contents

List of Tables

List of Figures

List of Abbreviations

FIM	Fisher Information Matrix
CRLB	Cramér-Rao Lower Bound
Lis	Lithium-sulfur
ARDS	Acute respiratory distress syndrome
PFC	Perflurocarbon
ECMO	Extra-coupled membrane oxygenation
DAQ	data Aquisition System
PCB	Printed Circuit Board
SPI	Serial Peripheral Interface
GUI	Graphical User Interface
PWM	Pulse With Module
PI	Proportional Integral
PMP	Pontryagin Minimum Principle

Chapter 1: Introduction

1.1 Motivation and Vision

This dissertation focuses on the impact of input shaping on the observability and **identifiability** of multi-compartment, nonlinear dynamic system models. This problem is particularly important in situations where the accurate modeling of such systems is needed for subsequent model-based monitoring and control. Identifiability is an established concept from the fields of system dynamics and information theory [1, 2]. It refers to the degree to which one can estimate a model's internal variables from input-output data. One can classify these internal variables into constant parameters versus time-varying state variables. The terms "parameter identifiability" and "state observability" refer, respectively, to one's ability to estimate these two types of internal variables from input-output data. This research also studies combined state/parameter identifiability. This is a broader concept that refers to one's ability to estimate a given model's state variables and parameters simultaneously.

Analyzing identifiability for a particular model is, fundamentally, an exercise in uncertainty quantification. The importance of this exercise stems in part from its potential to serve as a starting point for uncertainty propagation. For example, knowing the uncertainties in one's estimates of a model's internal variables, one can ask: how do these

errors propagate to induce further errors in the model's future predictions? To answer this question, one can use methods such as sensitivity analysis and Fisher Information analysis to obtain analytic bounds on parameter identifiability. This dissertation focuses on identifiability analysis for four main applications, all of them illustrating the close relationship between input structure and parameter identifiability. The first application focuses on the parameter identification and identifiability for a multi-compartment model of extracorporeal CO_2 removal dynamics in hypoxic and hypercarbic laboratory animals (more specifically, laboratory pigs). The second application focuses on the impact of input shaping on identifiability for drug resistance dynamics in cancerous tumors. The third application focuses on optimal input shaping for electrochemical battery model parameterization. The fourth application focuses on the structure of optimal input for parameter identifiability. Each of these application problems is discussed further below.

The first application of this dissertation is motivated by the following question: *can the respiratory dynamics of an extracorporeal laboratory animal CO_2 removal experiment be identified to better characterize the underlying mechanisms?* The primary functions of the respiratory system are to bring oxygen into the body (oxygenation), and expel carbon dioxide out of the body (CO_2 removal). Inhaled oxygen enters the lungs and reaches the alveoli (the small air sacs in the lungs that allow for rapid gaseous exchange). The walls of the alveoli share a membrane with the capillaries (a network of small blood vessels) that lets oxygen and carbon dioxide diffuse between the respiratory system and the bloodstream. If either of these two mechanisms – namely, oxygenation and CO_2 removal – fails to meet the body's demand, one effective treatment option is mechanical ventilation. However, mechanical ventilation can cause serious lung injury [3]. Another

option includes the direct oxygenation of the blood using techniques such as extracorporeal membrane oxygenation (ECMO) [4]. ECMO is a treatment that uses a pump to circulate blood through an artificial lung back into the bloodstream. This system provides heart-lung bypass support outside of the body. Unfortunately, ECMO is accompanied by extreme limitations that make it inappropriate for many patients [5]. Therefore, there is always a need for novel oxygenation and ventilation mechanisms and equipment to ease life for patients with respiratory illnesses. A third potential treatment is currently being explored by a large, collaborative team of surgeons, medical researchers, and control engineers. The particular technology of interest in this collaboration is the circulation of an oxygenated perfluorocarbon (specifically, perfluorodecalin) through the abdominal (specifically, peritoneal) cavity. The idea is to utilize diffusion dynamics within the peritoneal cavity to essentially create a "third lung", in a manner akin to the use of this cavity as a "third kidney" during peritoneal dialysis [6]. To date, experiments on large animals (specifically, pigs) have demonstrated the potential benefits of this technology for treating hypoxia and hypercarbia [7, 8]. However, the underlying dynamic mechanisms behind this novel extracorporeal oxygenation technology are not yet fully understood.

The main question behind the second application problem is: *to what extent does the chemotherapeutic drug delivery protocol for treating a partially drug-resistant cancerous tumor affect the identifiability of the tumor's drug resistance dynamics?* Motivation for examining this research problem stems from the fact that drug resistance is responsible for a significant portion of chemotherapeutic treatment failures. Drug resistance occurs because of various factors including changes in drug metabolism, mutations, genetic rewiring, and tumor heterogeneity [9]. Regardless of the specific cause of drug

resistance, the main outcome is that a portion of the cancerous cell population continues to suffer from defective apoptosis, even in the presence of a given drug. Therefore, understanding and predicting the behaviour of drug resistant cells is essential for determining an optimal chemotherapeutic treatment schedule. This study investigates the combined state and parameter identifiability of a partially drug-resistant tumor to gain insight into feasibility of accurate estimation of its dynamics. To the best of the author's knowledge, this problem has not been examined in the literature prior to this work.

The primary motivating questions behind the third and fourth applications are: *what is the shape of a periodic cycling input trajectory that maximizes parameter identifiability of an electrochemical battery?* Moreover, *how does the shaping of a cycling trajectory affect the accuracy with which the battery's parameters can be estimated?* Electrochemical batteries, such as lithium-ion and lithium-sulfur batteries, have high power and energy densities which make them attractive for many energy storage applications. However, aging, degradation and damage mechanisms are prevalent problems threatening the performance and longevity of these batteries. There is growing interest in the use of model-based online battery diagnostics and control in order to estimate the physical variables directly responsible for degradation and damage. Improving the accuracy with which a battery model's parameters are estimated has the potential to lead to more accurate battery performance prediction and control. The literature already examines the problem of optimizing the test cycles of electrochemical batteries in order to enable more accurate parametere estimation [10, 11, 12, 13, 14, 15, 16, 17, 18]. Such optimization has the potential to improve parameter estimation speeds and accuracies considerably, leading to better utilization of costly laboratory test setups and time. These potential benefits are

well-established in the literature for thermal, electrochemical, and multi-physics battery models. However, to the best of the author's knowledge, fundamental insights into the structure of information-maximizing lithium-ion battery test protocols are still relatively scarce in the literature. Also, the problem of optimal input shaping for maximizing parameter identifiability has not yet been studied for lithium-sulfur batteries, an important emerging battery technology.

1.2 Parameter Identifiability: Definitions and Approaches

Identifiability is a well-established concept in control theory, with important mathematical connections to other concepts such as observability and controllability [19, 20]. To illustrate this concept, consider the following (potentially nonlinear) dynamic system model:

$$\begin{aligned} \dot{\mathbf{x}}(t) &= f(\mathbf{x}(t), \mathbf{u}(t), \theta) \\ \mathbf{y}(t) &= h(\mathbf{x}(t), \mathbf{u}(t), \theta) \end{aligned} \tag{1.1}$$

The above model is presented in state-space form for simplicity, but the discussion that follows can be generalized to other types of models (e.g., differential algebraic equation models, partial differential equation models, etc.). In this model, $\mathbf{x}(t)$ is a vector of state variables, $\mathbf{u}(t)$ is a vector of known system inputs, $\mathbf{y}(t)$ is a vector of measurable output quantities, and θ is an unknown parameter vector that needs to be estimated based on experimental data. Broadly speaking, if there exists an admissible $\mathbf{u}(t)$ which can

transfer an initial state of interest to a target state in a finite time, the dynamic system in the Eq. (1.1) is *controllable*. Moreover, given an initial state $\mathbf{x}_0$ and an admissible control $\mathbf{u}(t)$, if the current system state $\mathbf{x}(t)$ can be determined from measurements of the system inputs and outputs in a finite amount of time, the system is *observable*[21, 22, 23]. Finally, for this general dynamic system, identifiability can be seen as the answer to a yes/no question: can one uniquely determine the parameter vector θ from the given system's input $\mathbf{u}(t)$ and the measurable system output $\mathbf{y}(t)$? If the answer is yes, then the parameter vector θ is *identifiable*[21]. Note that the above definitions of controllability and observability assume the parameter vector θ to be known, whereas the definition of identifiability assumes that this parameter vector is unknown. Therefore, in a broad sense, one can view identifiability as a prerequisite condition that must be met in order for one to pursue model-based observer/controller design.

There are two important questions that one can ask regarding a given model's parameter identifiability. First, is the problem of identifying or estimating the parameters mathematically solvable? Second, how accurately can this problem be solved? The former question, which focuses on feasibility, is known as the **structural identifiability** question. The latter question, which focuses on estimation accuracy, is known as the **practical identifiability** or (numerical identifiability) question.

Structural identifiability focuses on the question of whether or not the structure of a given model enables the solution of the underlying parameter estimation problem. The concept of structural identifiability was first introduced by Bellman and Åström at 1970 for linear models based on Laplace transforms [24]. Later, other linear and nonlinear structural identifiability methods were introduced based on power series ex-

pansions, similarity transformations, differential algebra, and the implicit function theorem [25, 26, 27, 28]. Ljung *et al.* also pioneered the concept of global identifiability [2, 29, 30]. There are two basic assumptions upon which structural identifiability analysis heavily relies:(i) the model structure is known and (ii) measurements are exact, with no measurement errors [21]. However, these two assumptions are clearly not valid in practice. For instance, in biomedical research, both model uncertainty and measurement error are usually large. Therefore, even when structural identifiability analysis suggests that model parameters can be uniquely identified, the estimates of model parameters may still be unreliable or inaccurate. Thus, it is necessary to evaluate whether structurally identifiable parameters can be reliably estimated with acceptable accuracy from noisy data. This is called *practical identifiability* analysis. The parameter identifiability studies in this dissertation fall under the practical identifiability category. Practical identifiability techniques encompass Monte Carlo simulation, correlation matrix methods, and sensitivity analysis methods [21, 31, 32]. In this work we apply sensitivity analysis to different dynamic systems in order to assess the identifiability of their parameters.

1.3 Sensitivity Analysis and Fisher Information

Sensitivity analysis methods are frequently used for analyzing dynamic systems' practical identifiability. This process typically begins with an assessment of the sensitivity of the system output to variations in the underlying parameters. Consider, for example, the dynamic system model in Eq. (1.1). For any given set of values of the parameter vector, θ, the model predicts a corresponding output history, $\mathbf{y}(t)$. The measured

output history, $\mathbf{y}_m(t)$, may not match this predicted history exactly. This mismatch can result from multiple factors, including modeling errors, parameter estimation errors, and measurement noise.

Consider a scenario where the output of the given dynamic system is measured at sampling instants separated by a constant sampling time, δt. Suppose that at each sampling instant, t_i, the relationship between the measured output and true output is given by:

$$\mathbf{y}_m(t_i) = \mathbf{y}(t_i) + \mathbf{v}(t_i), \tag{1.2}$$

where $\mathbf{v}(t_i)$ refers to the measurement noise process. The above equation implicitly assumes that the model in Eq. (1.1) describes the given system's dynamics exactly. Therefore, the only source of discrepancy between the true and measured dynamic system output trajectories is a sensor noise process, $\mathbf{v}(t_i)$. Different types of noise processes are possible. The discussion below assumes that the sensor noise process, $\mathbf{v}(t_i)$, is independent, identically distributed, and Gaussian, with a mean of zero and a variance of σ^2 (for the special case of a scalar output measurement). Stated mathematically, the discussion assumes that:

$$v(t_i) \sim N(0, \sigma^2) \tag{1.3}$$

The measured system output, $\mathbf{y}_m(t)$, is not guaranteed to equal either the true system output, $\mathbf{y}(t)$, or the predicted system output from Eq. (1.1). Discrepancies will exist between these various signals, caused by factors such as parameter estimation errors, modeling errors, and measurement noise. Let the likelihood function, $p(\mathbf{y}_m(t)|\theta)$, represent the likelihood that this mismatch is caused solely by measurement noise. One common parameter estimation approach - namely, maximum likelihood estimation - attempts to find the parameter values that maximize this likelihood function. Intuitively, maximizing the likelihood function furnishes a model whose output prediction errors are most likely to be caused by measurement noise, as opposed to parameter estimation errors. The choice of likelihood function depends on the nature of the underlying measurement noise process. Consider, for example, a system with a single output variable, $y(t)$, that is measured at N discrete instants of time, t_i. Suppose that the measurement noise at these instants in time is an independent, identically distributed, Gaussian process with zero mean and a variance σ^2, as discussed above. Then the likelihood function can be derived from the probability density function of the Gaussian noise process, as shown below [33]:

$$p(y_m(t)|\theta) = \left(\frac{1}{\sqrt{2\pi}\sigma}\right)^N \prod_{i=1}^{N} \mathrm{e}^{-\frac{(y_m(t_i)-y(t_i,\theta))^2}{2\sigma^2}} \tag{1.4}$$

In the above equation, the expression $y(t_i, \theta)$ is shorthand for the ideal predicted model output from Eq. (1.1) at time t_i, for a given value θ of the parameter vector. Maximizing the likelihood function is equivalent to maximizing its natural logarithm, given the monotonicity of logarithmic functions. This leads to the so-called log likelihood

function below:

$$\ln p(y_m(t)|\theta) = N \ln\left(\frac{1}{\sqrt{2\pi}\sigma}\right) - \sum_{i=1}^{N} \frac{(y_m(t_i) - y(t_i,\theta))^2}{2\sigma^2} \tag{1.5}$$

The goal of maximum likelihood estimation is to determine the specific set of parameters that maximizes the above likelihood function. In other words, maximum likelihood estimation solves the following problem:

$$\theta^* = arg\ max_\theta\ p(y_m(t)|\theta) \tag{1.6}$$

The above maximum likelihood estimation problem is analogous to classical least-squares estimation. In particular, maximizing the log likelihood function is equivalent to minimizing the sum of the squares of the model prediction residuals with respect to the unknown model parameters. This is true under the above assumptions regarding the measurement noise process - namely, that the measurement noise signal is a zero-mean, Gaussian, and independent, identically distributed (iid).

Fisher information quantifies the expected curvature of the likelihood function around the maximum likelihood estimate θ^*. The Fisher information matrix is defined as follows [34]:

$$\mathbf{F} = E\left\{\left(\frac{\partial}{\partial\theta}\ln p(y_m(t)|\theta)\right)^T\left(\frac{\partial}{\partial\theta}\ln p(y_m(t)|\theta)\right)\right\} \tag{1.7}$$

where the symbol E denotes the expectation operator [35]. Note that this definition of the Fisher information matrix is broadly applicable to different likelihood functions, and

hence to different noise processes.

By definition, the Fisher information matrix is positive semi-definite. The key idea behind Fisher information analysis is that the inverse of this matrix, if it exists, furnishes the well-known Cramér-Rao bounds on the best parameter estimation covariance achievable by any unbiased parameter estimator [34, 35, 36]. Stated mathematically:

$$\mathrm{cov}(\hat{\theta}) \geq F^{-1} \tag{1.8}$$

The above result is known as the Cramér-Rao theorem, and forms a key foundation for this dissertation. The main idea behind this research is twofold. First, this work aims to use Fisher information analysis to examine fundamental limitations on the accuracy with which multi-compartment dynamic system model parameters can be estimated. Second, this work also aims to examine the degree to which optimal input shaping can help improve this parameter estimation accuracy.

Fisher information analysis is often closely intertwined with sensitivity analysis. Consider, for example, a single-output dynamic system governed by Eq. (1.1), with an output noise process governed by Eq. (1.3). Let the symbol $Y(t, \theta)$ denote the predicted output of this system, without noise, at time t, for a specific assumed value of the parameter vector θ. Given the above output measurement noise assumptions, let $\mathbf{e}_i$ represent the ith Eucledian vector in the n-dimensional combined space of unknown parameters and initial values. For instance, let $\mathbf{e}_1 = [1, 0, 0, 0, 0]^T$, $\mathbf{e}_2 = [0, 1, 0, 0, 0]^T$, and so on. Moreover, let $Y(k\delta t, \theta)$ represent the true value of the output, Y, at time $t = k\delta t$, for a given

set of unknowns, θ. Then the sensitivity function $s_i(k\delta t)$, can be defined as follows:

$$s_i(k\delta t) = \lim_{\delta\theta_i \to 0} \frac{Y(k\delta t, \theta + \mathbf{e_i}\delta\theta_i) - Y(k\delta t, \theta)}{\delta\theta_i}, \tag{1.9}$$

where $\delta\theta_i$ represents an infinitesimal change in the ith unknown parameter. Given the above sensitivity function, one can construct the following sensitivity matrix:

$$\mathbf{S} = \begin{bmatrix} s_1(\delta t) & s_2(\delta t) & s_3(\delta t) & ... & s_n(\delta t) \\ s_1(2\delta t) & s_2(2\delta t) & s_3(2\delta t) & ... & s_n(2\delta t) \\ \vdots & \vdots & \vdots & \vdots & \vdots \\ s_1(N\delta t) & s_2(N\delta t) & s_3(N\delta t) & ... & s_n(N\delta t) \end{bmatrix}, \tag{1.10}$$

where N is the total number of samples over which identifiability analysis is performed.

If the measurement noise process is zero-mean, Gaussian, and iid, then the Fisher information matrix can be related to the above definition of the sensitivity matrix as follows:

$$\mathbf{F} = \frac{1}{\sigma^2}\mathbf{S}^T\mathbf{S} \tag{1.11}$$

The above result is important because it highlights the degree to which maximizing the identifiability of a dynamic system's parameters essentially amounts to maximizing the sensitivity of its output to perturbations in these parameters. For linear estimation problems, such maximization leads to the perhaps trivial conclusion that more aggressive inputs lead to better parameter identifiability, assuming the underlying dynamic system model to be accurate. However, for estimation problems that are nonlinear in the param-

eters, optimizing a system's input trajectory for identifiability has the potential to lead to non-trivial insights. There may, for instance, be specific shapes of the input trajectory that improve identifiability by exciting the underlying dynamics in an optimal manner. Moreover, there may be specific input trajectories that lead to particularly poor identifiability by obscuring key underlying system dynamics. This dissertation examines these insights for a variety of multi-compartment dynamic system models, covering both healthcare systems and electrochemical batteries.

1.4 Dissertation Contributions and Outline

The remainder of this dissertation explores four practical problems related to multi-compartment dynamic system identifiability, as explained earlier in this chapter. This exploration highlights the breadth of parameter identifiability analysis for dynamic systems. Furthermore, the progression of problems is chosen to reflect a progression of fundamental research topics related to dynamic system parameter identifiability. Specifically, the dissertation progresses from *motivating* the importance of identifiability analysis using animal experiments (Chapter 2), to *analyzing* identifiability in drug-resistance tumors (Chapter 3), to *optimizing* identifiability for lithium-sulfur batteries (Chapter 4), to finally *unveiling* the structure of an identifiability-optimizing lithium-ion battery test cycle using the Pontryagin minimum principle (Chapter 5).

Chapter 2: Parameterizing a Model of CO_2 Transport in a Test Animal During a Novel Extra-Corporeal Ventilation Experiment

2.1 Introduction

This chapter focuses on two interconnected research problems. First, from a practical perspective, the chapter examines the dynamics of CO_2 removal from a hypercarbic laboratory test animal via the perfusion of an oxygenated perfluorocarbon (specifically, perfluorodecalin) through the animal's peritoneal (or abdominal) cavity. This practical research problem builds on the hypothesis that perfusing perfluorodecalin through a hypoxic and/or hypercarbic patient's or animal's abdominal cavity can provide significant respiratory support. Second, from a fundamental perspective, the chapter highlights the importance of dynamic system parameter identifiability in research problems including the modeling of gas transport in human patients and test animals. This motivates subsequent work in this dissertation on the analysis and optimization of identifiability[1].

The research in this chapter is motivated by the need for providing life support to patients suffering from respiratory failure. Potential causes for respiratory failure in-

[1]Broadly speaking, the research presented in this chapter includes the development of a mechatronic setup for perfluorodecalin perfusion experiments, as well as the analysis of gas transport dynamics in animal experiments exploiting this setup. The former body of work has been submitted for potential archival in the IEEE/ASME Transactions on Mechatronics, and the latter body of work is currently in preparation for potential publication.

clude acute respiratory distress syndrome (ARDS), pulmonary embolism, pneumonia, toxic inhalation, as well as ailments such as COVID-19. The fact that the U.S. alone has historically seen more than 100,000 ARDS-related hospitalizations annually, even during pre-pandemic years, highlights the public health magnitude of respiratory failure [37].

The two main functions of the respiratory system are to bring oxygen into the body and expel CO_2 out of the body. If either of these two functions, oxygenation or CO_2 removal, falls below critical levels, then the patient will not survive without additional support. If the condition is severe, then the patient will require mechanical ventilation. This is a technique where the airway is intubated in an airtight manner, allowing positive pressure assistance of the lungs, often using an oxygen-enriched gas mixture. Potential complications of mechanical ventilation, therefore, include oxygen toxicity and barotrauma to the lungs, both of which can result in ventilator induced lung injury (VILI). VILI can compound the underlying lung dysfunction and exacerbate pulmonary failure – potentially to a fatal degree [3, 38, 39, 40, 41]. In such situations, unless gas exchange is augmented by extra-pulmonary means, the patient will not survive.

Extra-corporeal membrane oxygenation (ECMO) is currently the only pulmonary-independent modality available to supplement gas exchange. It involves drawing blood out of the patient through a vascular cannula, oxygenating it, then pumping it back into the patient through another cannula [4]. Unfortunately, ECMO is an expensive resource, with one study indicating a mean total hospital cost above $200,000 per patient[42]. The availability of ECMO is limited by cost and personnel requirements: its initiation is typically performed by specially trained cardiac surgeons, and its maintenance requires constant monitoring by highly trained personnel. Even when available, ECMO is accompanied by

contraindications or exclusion criteria that may make it a nonviable option for patients with potentially reversible lung failure. Therefore, there is a need for additional ways to support respiration that do not require the lungs or ECMO.

The main idea motivating the research in this chapter is to supplement gas exchange by perfusing (i.e., circulating) an oxygenated perfluorocarbon (PFC) through a patient's peritoneal (i.e., abdominal) cavity. Perfluorocarbons (PFCs) are organic compounds consisting either predominantly or entirely of carbon and fluorine. They are inert and recognized for their very high oxygen and carbon dioxide solubilities [43, 44]. Thanks to these properties, PFCs are well-suited for medical applications [45, 46, 47, 48]. For example, they have been investigated as blood substitutes [7, 49] and are also used for ophthalmologic surgeries [8]. One particularly relevant application is the use of PFCs for *liquid ventilation*, or "liquid breathing". This refers to filling the lungs partially or completely with an oxygenated PFC in an effort to augment gas exchange [50, 51, 52, 53]. Both laboratory studies and clinical trials have been performed on liquid ventilation. These studies show that while liquid ventilation does indeed supplement gas exchange [54, 55, 56, 57], its benefits do not justify its adoption as an alternative to mechanical ventilation [58].

The research in this chapter is similar to liquid ventilation in its use of PFC to augment gas exchange, but fundamentally distinct in its use of the abdominal cavity, as opposed to the lungs, for gas exchange. Figure (2.1) summarizes this respiratory support approach. A perfusion circuit is used for oxygenating PFC, removing CO_2 from it, and warming it to body temperature. The oxygenated PFC is then perfused through the abdomen, where processes such as diffusion allow it to exchange oxygen and CO_2 with the bloodstream. Finally, the PFC is drained out of the abdomen, potentially using negative

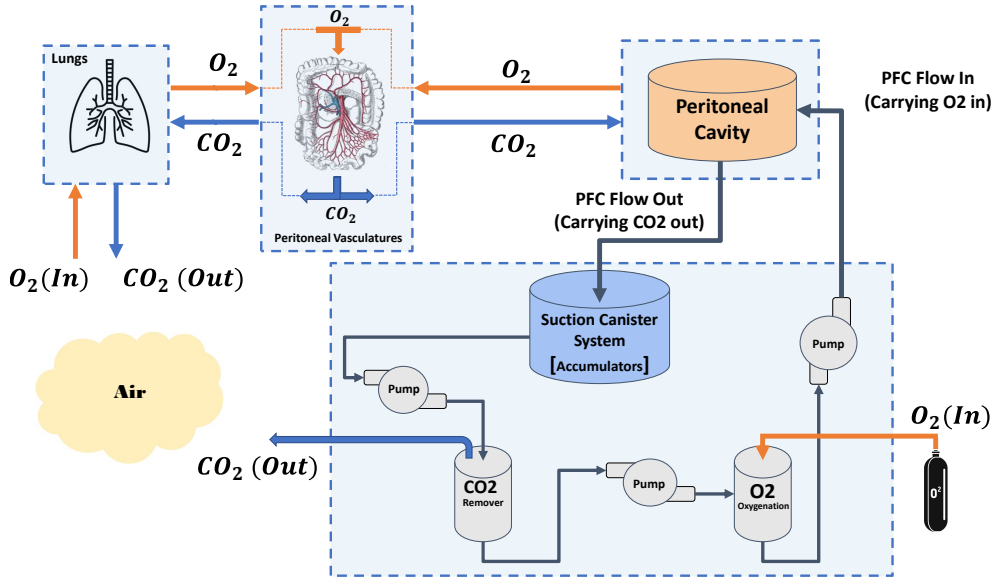

Figure 2.1: Schematic of the third lung concept

pressure from a suction/vacuum pump. The end result is a system that allows the peritoneal cavity to be used "like a lung," analogous to the way it is used "like a kidney" for peritoneal dialysis [6]. One potential benefit of this "third lung" concept is the fact that it offers a pulmonary-independent means of gas exchange that can supplement mechanical ventilation, thereby resting the lungs and helping them heal. Another potential benefit is the fact that the third lung innovation does not require a direct blood-device interface, thereby avoiding many of the risks and contra-indications of ECMO.

Previous medical research by one of this dissertation's committee members (Friedberg) shows that the third lung concept is indeed effective at providing oxygenation to large hypoxic animal models (namely, laboratory swine) [59]. While this prior research is encouraging, it leaves at least four important open questions and research challenges. First, it is not clear what operating conditions (e.g., perfusion flowrates, pressures, temperatures, PFC oxygenation levels, etc.) are ideal for the third lung concept. Second, the

impact of the third lung intervention on hemodynamic variables such as heart rate has yet to be fully characterized. Third, the impact of the intervention on CO_2 clearance in large laboratory animals has not yet been fully examined in the literature. Fourth, there is a need to implement the third lung concept using a mechatronic setup with extensive data acquisition and control capabilities supporting both ongoing animal experiments and potential future human interventions. To address these challenges, a research team including the author has collaboratively developed a novel mechatronic setup capable of (i) performing controlled peritoneal PFC perfusion experiments and (ii) gathering extensive datasets characterizing these experiments, from both setup-side and physiological sensors. The specific contributions of this dissertation's author include: (i) the development of this setup's data acquisition and control capabilities as well as (ii) the identification of a dynamic model of CO_2 gas transport from animal test data gathered by this setup.

From a fundamental perspective, the research in this chapter investigates the problem of parameterizing a model of the CO_2 transport dynamics associated with the "third lung" intervention. The literature already presents multi-compartment dynamic models of both human and animal gas transport [60, 61, 62, 63]. Moreover, the literature parameterizes these models from experiments not involving the abdominal circulation of oxygenated PFCs [60, 62, 64, 65, 66, 67, 68, 69, 70, 71]. From a fundamental perspective, one important contribution of this chapter is the degree to which it extends the above parameter identification and identifiability analyses to the "third lung" concept, building on elementary physical principles such as Fick's law of diffusion [72].

The remainder of this chapter is organized as follows. Section (2.2) summarizes mechanical design of the third lung setup. Section (2.3) describes the setup's monitor-

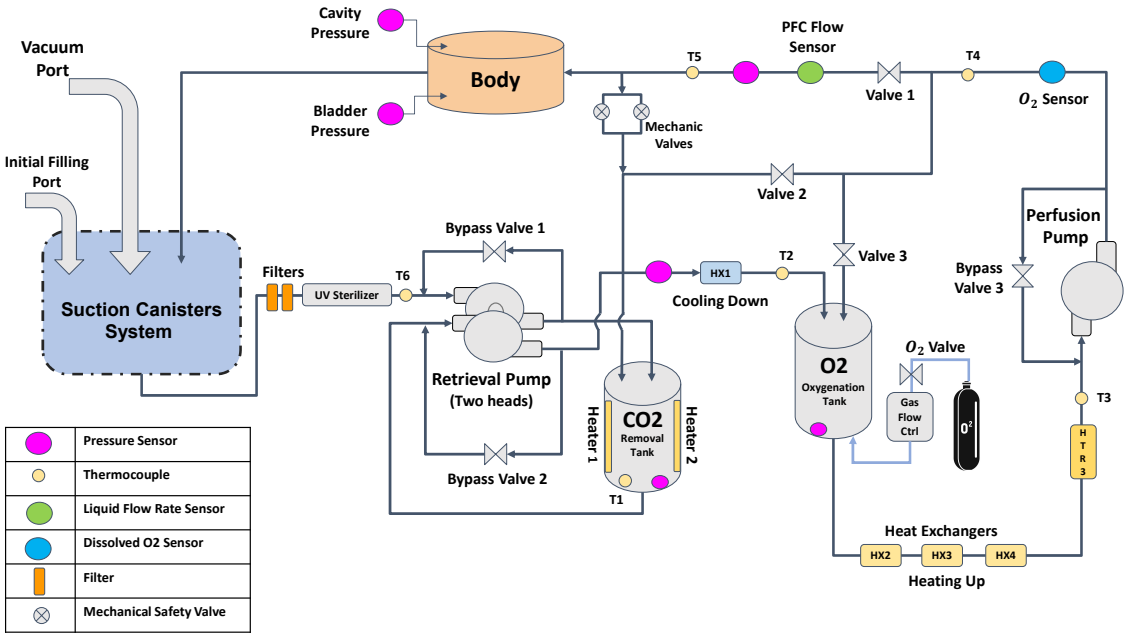

Figure 2.2: The third lung ventilator setup diagram

ing and data acquisition system. Section (2.4) summarizes the setup's key closed-loop control functionalities. Section (2.5) presents preliminary data from laboratory animal experiments highlighting some of the setup's successes in controlling perfusion parameters such as perfusate flowrate, temperature, pressure, and oxygenation level. Section (2.6) examines the problem of modeling and parameterization the CO_2 transport dynamics in a hypercarbic test animal. Section (2.7) performs identifiability analysis for the estimated parameters from section (2.7). Finally, Section (2.8) summarizes the chapter's conclusions.

2.2 Design of the third lung ventilator

Experiments on the third lung intervention have, to date, focused on large laboratory animals (swine) because they are close in size, core body temperature, and ventilation

needs to human patients. The perfusion setup described in this chapter is designed to facilitate these experiments, with the ultimate goal of enabling emergency interventions in human patients. The setup is designed to meet five key requirements, namely:

1. Oxygenating the PFC and removing CO_2 from it prior to perfusion.

2. Providing a PFC perfusion flowrate sufficient for supplementing gas exchange. For large animal experiments, prior research suggests that flowrates of up to 6 liters per minute may potentially be required.

3. Delivering up to 11 liters of PFC to the abdomen at any given time. This is important, considering the degree to which the abdominal cavity distends during perfusion. Filling the distended abdomen of a 40-50kg adult pig, for example, typically requires 6-7 liters of PFC.

4. Achieving perfusion temperatures that are consistent with core body temperature - namely, $37°C$ for human patients and $39°C$ for laboratory pigs.

5. Ensuring safety by avoiding intra-cavity pressures conducive to compartment syndrome.

Figure (2.2) presents the design of the third lung setup, tailored to meet the above requirements. When filled, the setup can accommodate 26 liters of PFC, of which 11 liters can be supplied to the animal's or patient's body at any time. The remaining PFC must stay in the setup to ensure that the setup is properly primed and able to sufficiently oxygenate the PFC. PFC enters and leaves the abdomen through tubes typically used as central venuous catheters. Different catheter sizes can be accommodated, a typical size

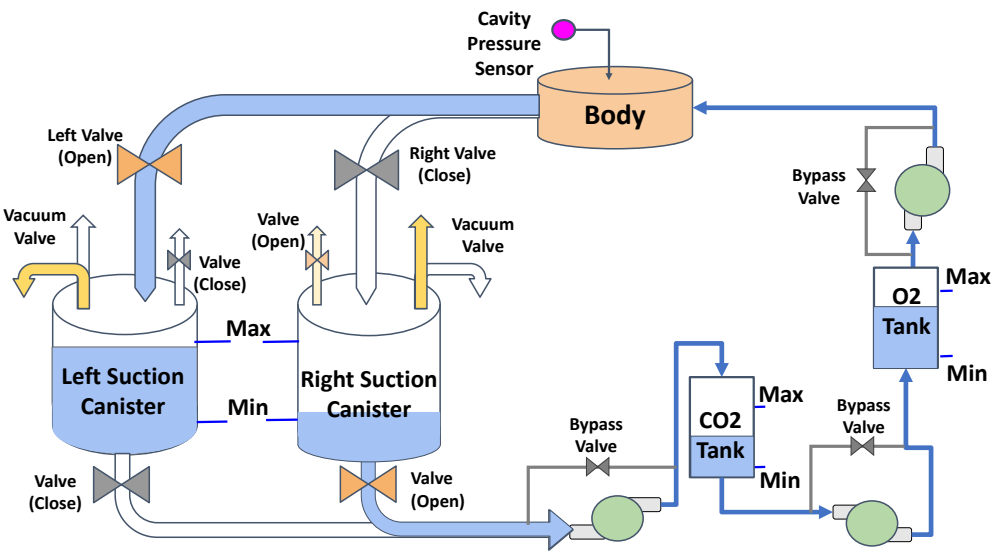

Figure 2.3: The two-canister accumulator system

being 36 on the French scale (i.e., 12mm diameter). An oxygenated PFC (specifically, a mix of cis- and trans-Perfluorodecalin) is perfused through the abdomen of the patient or animal. The PFC then drains into an accumulator using a combination of gravitational drainage and active suction via a vacuum pump. Two different versions of this accumulator have been built and can be rapidly interchanged, namely: a single-canister system and the dual-canister system in Fig. (2.3). The former system uses one canister to receive fluid drained from the test animal and supply it to the rest of the setup. In contrast, the dual-canister system switches periodically between a canister that recovers fluid from the animal versus a canister from which fluid is pumped into the rest of the setup.

Once the fluid is recovered by the accumulator system, it is filtered then exposed to an ultraviolet flood light. The fluid then passes through a chamber where CO_2 is purged. The specific setup sketched in Fig. (2.2) uses PFC heating plus exposure to an oxygen stream as means of CO_2 removal, the idea being to rapidly achieve equilibrium between dissolved and incoming gas concentrations. Alternative CO_2 removal mechanisms in-

clude the use of vacuum to bubble CO_2 out of the PFC as well as the use of chemical removal means (e.g., soda lime canisters). If the temperatures used for CO_2 removal exceed the ideal perfusion temperature, the setup provides the option to pass the warm PFC through a heat exchanger connected to cold water flow from a cardioplegic heater/chiller. The PFC is then oxygenated using a gas bubble chamber connected to an oxygen tank through an actively-controlled valve, with the possibility that future designs may employ membrane gas exchangers instead. Next, the temperature of the PFC is regulated to meet the desired perfusion target using a mix of electric heating and heat exchange with hot water from the cardioplegic heater/chiller unit. Finally, the oxygenated PFC is pumped into the abdomen.

As shown in Fig. (2.2), the setup needs to transfer PFC from the suction canisters to the CO_2 removal chamber, then to the oxygenation chamber, then finally to the abdomen. Two peristaltic pumps are used for achieving these three functionalities. A dual-head "retrieval pump" transfers fluid from the suction canister(s) to the CO_2 removal chamber, then to the oxygenation chamber. Next, a "perfusion pump" supplies PFC to the animal. Balancing the PFC fluid levels in the various chambers can be achieved through bypass valves, as shown in Fig. (2.2), with the recognition that modifying the setup to incorporate three independent pumps may potentially provide greater control authority. The setup incorporates a mix of spring-loaded passive and actively-controlled mechanical bypass valves on the final perfusion line. These valves provide the ability to bypass the abdomen if intra-cavity pressure increases beyond critical limits dictated by setup design (in case of the passive valves) or operator input, if the operator dictates a software-based pressure limit (in case of the active valves). This is important for avoiding cavity pressures

conducive to compartment syndrome.

Temperature control is potentially critical for the success of the third lung intervention, and requires significant fluid heating capabilities. Heating the PFC entering the final perfusion line is needed for ensuring compatibility between perfusion temperature and core body temperature. Moreover, pre-heating the PFC beyond core body temperature followed by cooling it back down may potentially important for CO_2 removal. For illustrative purposes, consider the problem of heating the PFC from a room temperature of $22°C$, to a desired CO_2 removal temperature of $42°C$, assuming a PFC flowrate of 5 liters per minute. Knowing that the density, ρ, of Perfluorodecalin is 1.93 $[kg/L]$ and its specific heat capacity, C_p, is 1000 $[J\ kg^{-1}\ K^{-1}]$, Eq. (2.1) solves for the heat, Q_{th}, required for this functionality:

$$\begin{aligned} Q_{th} &= \dot{m} c_p \Delta T \\ &= (5\ [\frac{L}{min}]) * (1.93\ [\frac{kg}{L}]) * (1000\ [\frac{J}{KgK}]) * (20\ [K]) \\ &= 193000\ [\frac{J}{min}] = \frac{193000}{60\ [sec]} \cong 3216\ [W], \end{aligned} \tag{2.1}$$

where ΔT is the desired rise in PFC temperature and $\dot{m}$ is the mass flowrate of PFC.

The setup is equipped with two $250[W]$ electric heaters in its CO_2 removal chamber plus a $100[W]$ electric heater attached to the final perfusion line. Moreover, the setup is connected through heat exchangers to the hot and (optionally) cold water outputs of a cardioplegic chiller/heater unit. The chiller/heater unit can provide up to $3000[W]$ of heat to its output hot water, which can be raised to temperatures as high as $41°C$. Given the

proximity of this hot water temperature to the final perfusion temperature, three of the setup's four heat exchangers are used for heating the PFC, compared to a single optional heat exchanger for cooling. These details highlight the importance of the coordinated control of the setup's heating (and potential cooling) assets in order to ensure effective perfusion temperature control. Other critical variables that the setup must monitor and control include perfusion flowrate, total perfused volume, perfusate gas concentrations, and intra-cavity pressure. The next section of this chapter presents a detailed description of the monitoring, data acquisition, and control functionalities implemented to meet these goals.

2.3 Setup monitoring and data acquisition

Figure (2.4) provides a high-level overview of the components of the setup's monitoring and data acquisition system. This system: (i) monitors the setup's performance, (ii) monitors the effect of perfusion on the test animal, and (iii) enables important closed-loop control functionalities. Up to 43 signals are collected by this system, from 28 different sensors and patient monitors, in order to collectively satisfy the data acquisition requirements below. Note that the physical locations of these sensors, where possible, are indicated in Fig.s (2-3).

- **Fluid height/volume monitoring** (6 sensors, 6 signals): The setup has the ability to monitor the height of the PFC in all of its canisters - namely, the oxygenation canister, the CO_2 removal canister, and its 1-2 canister accumulator. This is important for controlling the setup, as well as estimating the total volume of fluid delivered to

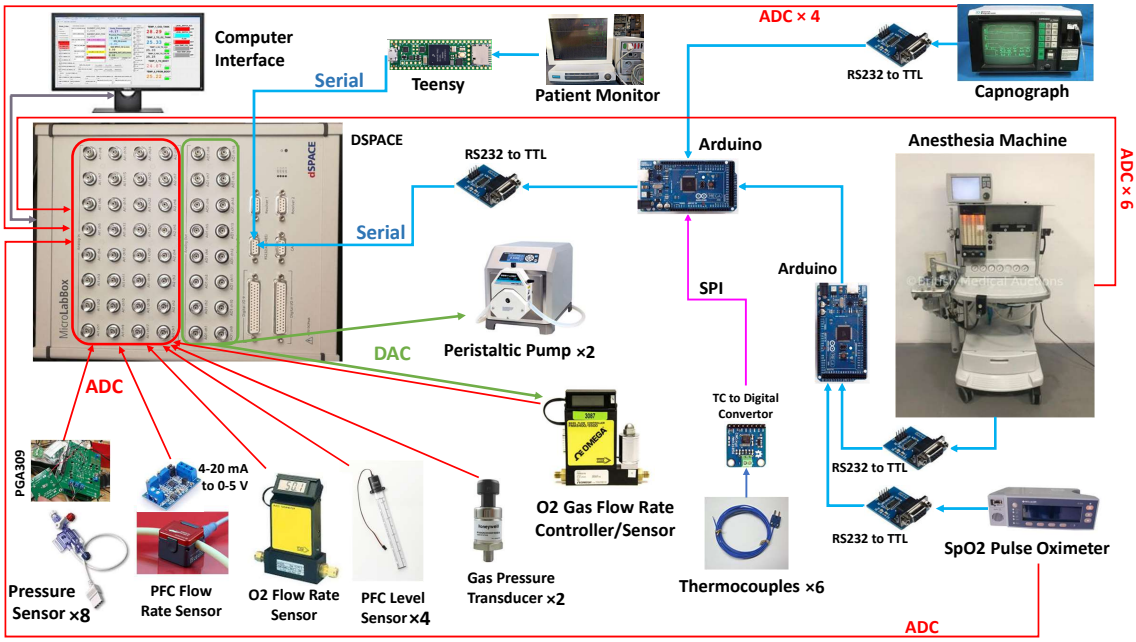

Figure 2.4: Setup monitoring and data acquisition system

the animal. To achieve this functionality, pressure sensors are mounted at the bottoms of all four canisters. Moreover, two pressure sensors are mounted at the tops of the two suction canisters in the dual-canister accumulator in order to measure air pressure during suction. The difference between air pressure in each canister and the pressure at the bottom of the canister enables the estimation of fluid height in the canister.

- **Secondary fluid height/volume monitoring** (4 sensors, 4 signals): The setup is equipped with an optional redundant method for estimating the height of the fluid in its canisters using 4 fluid level sensors.

- **PFC flowrate monitoring** (1 sensor, 1 signal): The setup monitors perfusion using a PFC flowrate sensor.

- **Oxygen flowrate monitoring** (2 sensors, 2 signals): The setup monitors the rate at

which oxygen flows into the CO_2 removal tank using a gas mass flowrate sensor. This rate is adjusted using a manual valve. The setup also controls oxygen flowrate into its oxygenation chamber using an active gas flowrate controller. This controller provides a measurement of the achieved oxygen flowrate back to the setup's data acquisition system.

- **Oxygen concentration monitoring** (1 sensor, 1 signal): An optical sensor is mounted on the final perfusion line in order to monitor the concentration of dissolved oxygen in the PFC.

- **Fluid temperature monitoring** (6 sensors, 6 signals): Thermocouples are used for monitoring PFC temperatures at multiple critical points in the setup. Specifically, six thermocouples are used for monitoring PFC temperature at: (i) the CO_2 removal tank; (ii) the inlet of the oxygenation tank; (iii) the inlet of the perfusion pump; (iv) the outlet of the perfusion pump; (v) the last point in the setup prior to perfusion; and (vi) either the return flow line or the surface of the final polishing heater, depending on usage of the setup.

- **Perfusion pressure monitoring** (4 sensors, 4 signals): The setup has the ability to measure the test animal's abdominal intra-cavity pressure and bladder pressure through two catheter-mounted pressure sensors. This is important for ensuring safe perfusion. Moreover, the setup uses two additional pressure sensors for monitoring internal fluid pressures prior to perfusion in order to avoid excessive pumping rates.

- **Physiological signal monitoring** (4 monitors, 19 signals): The setup has the abil-

ity to interface with four different medical monitoring systems in order to collect data regarding the test animal's physiological state (e.g., hemodynamics) and response to perfusion. Specifically, the setup can interface with: (i) a Nellcor **pulse oximeter**; (ii) a Capnomac **capnograph**; (iii) a Penlon **anesthesia machine**; and (iv) a TRAM-RAC **patient monitor**. Collectively, these devices provide 19 different measurements of physiological and/or anesthesia-related variables, with some of these measurements providing an important degree of redundnacy. For example, pulse oximetry is monitored using both the Nellcor oximeter and the TRAM-RAC patient monitor. Tables (2.1) and (2.2) list the signals provided by these monitoring devices using their serial and analog communication protocols.

The setup's monitoring and control system is built around a central data acquisition board - in this case, a dSpace MicroLabBox II board. Similar data acquisition boards are often used for instrumentation and control research [73, 74]. All analog sensor/monitor signals are read directly by the dSpace board's analog-to-digital converter. For sensor signals that use a current-based (i.e., $4 - 20mA$) analog communication protocol, standard integrated circuits are used for converting the signals to a voltage-based protocol first, prior to dSpace-based data acquisition. The remaining signals are communicated using either the RS-232 serial protocol or the serial peripheral interface (SPI) protocol. Figure (2.5) shows two Arduino Mega 2560 boards, together with a Teensy board (an Arduino clone) that they are used for reading these non-analog signals. As shown in Fig. (2.4), one of the Arduino boards is used for aggregating data from the pulse oximeter and anesthesia machine. The second Arduino board adds capnograph and SPI-based temperature

Table 2.1: The serial data from medical equipment

Pulse Oximeter (Nellcor)	**Capnograph** (Capnomac)	**Anesthesia Machine** (AVS)
SpO_2 $[0-100\%]$	$EtCO_2$ $[0-76\ mmHg]$	Measured Tidal Volume $[0-200cL]$ (TV*0.01 for L)
BPM $[0-250]$	$FiCO_2$ $[0-76mmHg]$	Measured O_2 $[0-100\%]$
	EtO_2 $[0-100\%]$	BPM $[0-120]$
	FiO_2 $[0-100\%]$	Measured Peak Pressure $[-22\ to\ 99\ cmH_2O]$
	EtN2O $[0-100\%]$	
	FiN2O $[0-100\%]$	
	Respiratory Rate $[4-60\ breaths/min]$	
Signal processing time $2000[ms]$	Signal processing time $10,000[ms]$	Signal processing time $2000[ms]$
General Sampling time ($150[ms]$)		

Table 2.2: The analog data from the anesthesia machine (AVS)

Parameter	**Range**	**Unit**
Real-time breathing circuit pressure (AWP)	[-10 to 100 cmH_2O] (0 to 4950 mV)	cmH_2O
Average breathing circuit pressure for previous respiratory cycle (MnAWP)	[-10 to 100 cmH_2O] (0 to 4950 mV)	cmH_2O
Real-time measured tidal volume (TidV)	[0 to 2.0 L] (0 to 5000 mV)	Liters
Real-time breathing circuit flow (AWF)	$[0\ to \pm 100\ L/min]$ $(0\ mV = 100\ L/min)$ inspiratory flow $2480\ mV = 0\ L/min$ inspiratory flow $5000\ mV = 100\ L/min$ expiratory flow)	L/min
Measured minute volume for previous respiratory cycle (MinV)	[0 to 75 L] (0 to 4950 mV)	Liters
Real-time measured oxygen percentage $(O_2\%)$	[0 to 100 %] (0 to 5000 mV)	Percent

data to this aggregate datastream, and forwards it to the dSpace board. Finally, the Teensy board selects specific signals from the fairly large dataset communicated serially by the TRAM-RAC patient monitor, repackages these signals, and communicates them directly to the dSpace board. Minimizing the amount of physical wiring necessary for communi-

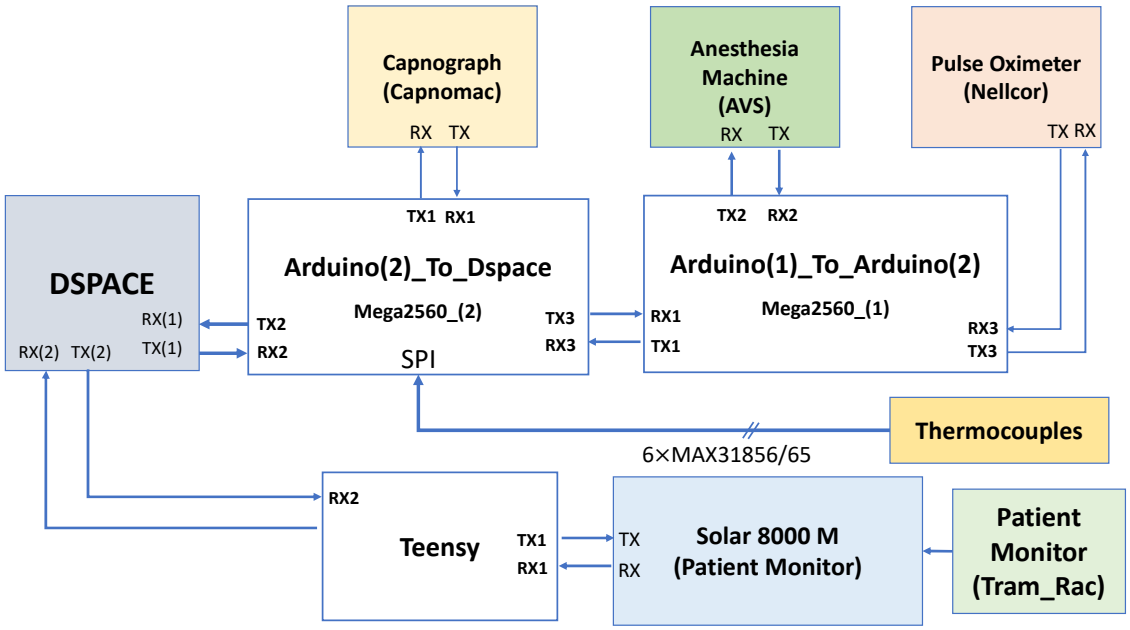

Figure 2.5: Setup communication layout

cating between these various devices is important, given the space limitation of a typical operating room. To address this issue, the setup collects the signals from all the medical devices using a custom printed circuit board (PCB), as shown on the left hand side of Fig. (2.6). A second custom PCB board, shown on the right hand side of Fig. (2.6) is then used to input these signals into the Arduino and dSpace boards.

Different components of the above data acquisition system monitor different underlying dynamics, with significantly different associated time constants. For example, if any of the setup's tubes are accidentally pinched during an experiment, the dynamics of the associated rise in fluid pressure are likely to be much faster than the dynamics of animal blood gas concentrations. With this in mind, the setup's dSpace board has a relatively fast master sampling time of $10ms$, corresponding to a sampling rate of 100 samples/second. Other components of the setup have progressively slower sampling rates and/or data processing times. For example: (i) The SPI protocol is used for reading temperatures every

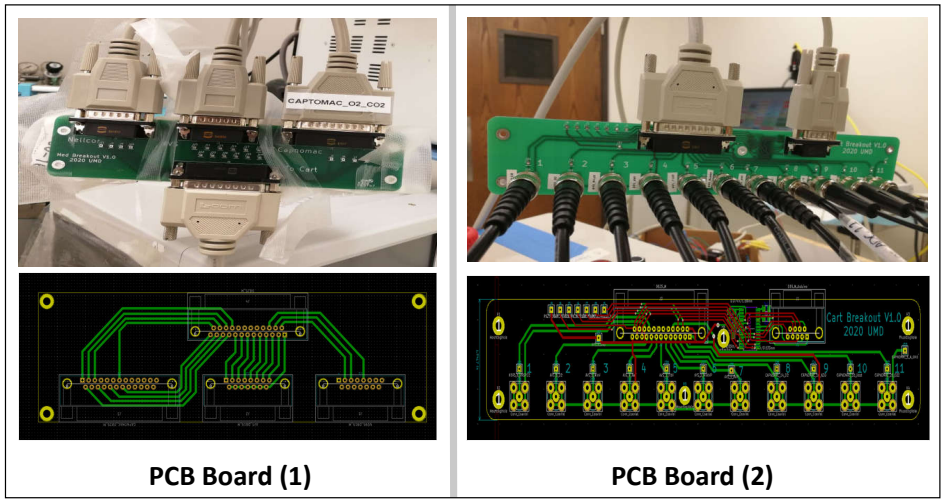

Figure 2.6: Medical equipment communication boards

$100ms$. (ii) The Arduino boards communicate data to the dSpace board every $150ms$. (iii) The Teensy board communicates data to the dSpace board every $500ms$. (iv) The pulse oximeter, anesthesia machine, and patient monitor communicate data to the Arduino and Teensy boards every $2000ms$. (v) The capgnograph communicates data to the corresponding Arduino board every $10,000ms$. (vi) Finally, the oxygen sensor updates its readings every 60 seconds, with the caveat that this is the only sensor that is read by a (proprietary) standalone program not communicating with the dSpace board.

Ensuring proper calibration of the above sensors and monitors is essential for the successful use of the setup. Four particular calibration efforts are needed on a regular basis, potentially as frequently as once per use of the setup for animal experiments. First, it is important to calibrate the PFC flowrate sensor, especially if it is used for closed-loop perfusion flowrate control. This is achieved by using the setup to pump a known volume of fluid into an external tank, then calibrating the sensor's data processing software to ensure that the time integral of the flowrate measured by the sensor matches the volume of

fluid delivered. Second, it is important to calibrate the canister pressure sensors to ensure correct fluid height estimates. This is done by filling the canisters to known fluid heights, then adjusting the reference voltage outputs of these sensors to furnish height estimates matching these known heights. Third, it is particularly critical to calibrate the cavity and bladder pressure sensors. This is done at the beginning of each animal experiment by exposing these sensors to atmospheric pressures, then adjusting the reference voltage outputs of these sensors to furnish a correct reading of atmospheric pressure. Finally, it is important to calibrate the optical dissolved oxygen concentration sensor. This sensor produces a raw output signal that does not equal dissolved oxygen concentration, but can be correlated to it. To calibrate this sensor, two samples of PFC were prepared with dissolved oxygen concentrations corresponding to partial oxygen pressures of 159mmHg and 760mmHg, respectively, at room temperature. These samples were then mixed in different proportions in order to prepare PFC samples with intermediate oxygen partial pressures. A small but noticeable increase in fluid turbidity occurred at dissolved oxygen partial pressures approaching 760mmHg. The sensor's reading was then correlated to dissolved oxygen fraction, defined as the partial pressure of dissolved oxygen divided by 760mmHg. Figure (2.7) shows the resulting sensor calibration plot.

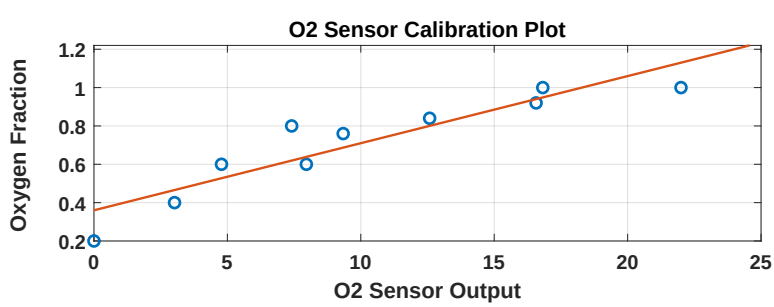

Figure 2.7: Calibration plot for optical oxygen sensor

2.4 Setup control

Four closed-loop control functionalities are implemented in the setup. Specifically, the setup contains discrete-event algorithms to control: (i) the filling of the two-canister system when in use; and (ii) the filling of the CO_2 removal chamber and oxygenation chambers. The setup also contains proportional-integral (PI) algorithms for controlling (iii) the temperatures of the PFC in the CO_2 removal chamber and final perfusion line; and (iv) the final perfusion flowrate/pressure. These controllers are discussed below.

2.4.1 Multi-Canister Switching Control

The intent of the dual-canister accumulator is twofold. First, it enables smooth, continuous PFC drainage from the test animal into the setup, potentially in the presence of active suction via a vacuum pump applied to the canisters. Second, it achieves this while minimizing the loading that this suction may apply on the retrieval pump. Discrete-event logic is needed for switching between two configurations. In one configuration, the "left" canister is receiving drained PFC and the "right" canister is supplying PFC to the rest of the setup. In the second configuration, these roles are reversed.

Figure (2.8) summarizes the discrete-event logic used for operating the dual-canister system when it is used. The figure generalizes this algorithm to an N-canister system. Most of the time, the setup is in a "k-filling" state, where canister k is being filled and all other canisters are being emptied. When canister k is full or any other canister is empty, an immediate switch takes place to a "transitioning" state. This state persists for a fixed

duration of time, during which the retrieval pump is shut down, suction is applied to the next canister in the sequence of canisters to fill, fluid is routed to that new canister, the outlet valves from the canisters to the rest of the setup are opened and closed appropriately, and the retrieval pump is restarted. Once this transition is complete, the discrete-event control algorithm automatically moves to a state where it is filling the next canister in the filling sequence, namely, canister number $(k+1) mod N$.

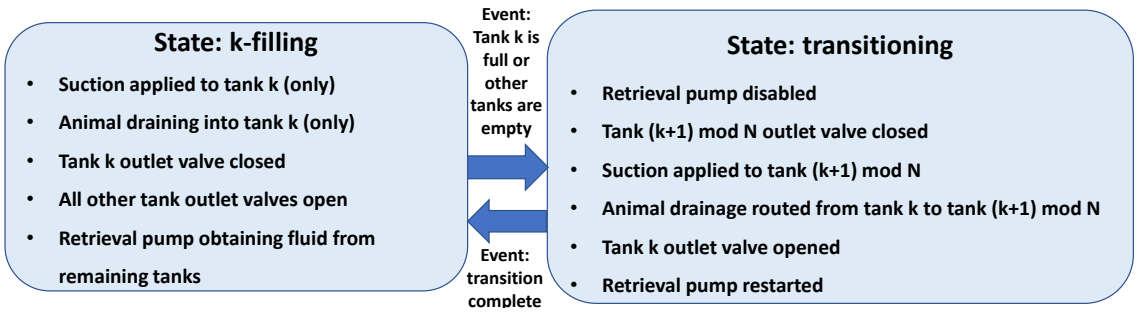

Figure 2.8: Multi-canister switching control algorithm

2.4.2 Control of Oxygenation and CO_2 Chamber Filling

Three different control algorithms/loops are used for controlling the retrieval pump and its associated bypass valves. Collectively, these loops ensure that the oxygenation and CO_2 removal chambers are replenished with fluid whenever possible, but prevented from overfilling.

- The first loop controls the retrieval pump flowrate. During normal operation, this flowrate is set to a constant value. However, when both the oxygenation and CO_2 removal tanks are full or when all the canisters in the accumulator are empty, the pump enters a temporary shutdown state, where flowrate is set to zero. The pump

dwells in this state for a fixed time duration, then returns to normal operation. This translates to a 2-state finite state machine governing the pump's operation, where it transitions automatically from normal operation to shutdown whenever needed. The setup's graphical user interface (GUI) allows the user to define the "empty" and "full" fluid levels for all canisters. The GUI also allows the user to dictate the constant flowrate used by the retrieval pump during normal operation. This flowrate should ideally be 0.5lpm-1.0lpm larger than the desired perfusion flowrate to ensure that the oxygenation and CO_2 removal tanks are always replenished.

- The second loop controls the bypass valve for the first retrieval pump head. This valve is closed during normal operation, allowing the retrieval pump to supply PFC from the accumulator to the CO_2 removal tank. However, when the $CO2$ removal tank is full, this valve automatically switches to a state where it is open, allowing flow to bypass the CO_2 removal tank. The valve dwells in this state for a fixed time duration, then automatically returns to the normal operation state. This makes it possible for the retrieval pump to replenish the oxygenation tank through its second pump head, without overfilling the CO_2 removal tank.

- The third loop controls the bypass valve for the second retrieval pump head. The logic governing this loop is identical to the logic governing the second control loop, the only difference being the the transition from closed- to open-valve operation is governed by fluid level in the oxygenation chamber. This loop allows the CO_2 chamber to be replenished, without overfilling the oxygenation chamber.

2.4.3 PFC Temperature Control

Two different loops are used for controlling PFC temperature (i) in the CO_2 removal chamber and (ii) at the final perfusion point. Both loops rely on proportional integral (PI) control with saturation and anti-windup logic. In both cases, the dynamics of PFC temperature are assumed to be governed by the following simple energy balance:

$$\begin{aligned} \rho V C_p \frac{dT}{dt} &= \rho Q C_p (T_{in} - T) \\ &\quad + hA(T_\infty - T) + uR_o I_o^2 \end{aligned} \tag{2.2}$$

In the above equation, T is the PFC temperature in the given control volume, assumed to be equal to the control volume's outlet temperature. Depending on the control loop, this control volume is either the CO_2 removal chamber or the pipe section/manifold being heated by the final perfusion heater. The volume of PFC being heated is denoted by V. Moreover, the density and specific heat capacity of the PFC are denoted by ρ and C_p, respectively. Thus, the term $\rho V C_p dT/dt$ equals the rate of change of thermal energy stored in the control volume, assuming that the amount of PFC in this control volume, V, is approximately constant. The first term contributing to this rate of change, $\rho Q C_p (T_{in} - T)$, equals the rate of energy transfer due to the flow of PFC, where Q is the volumetric flowrate of the PFC and T_{in} is the PFC temperature at the inlet of the control volume. The second term contributing to temperature change, $hA(T_\infty - T)$, represents the rate of convection heat transfer, where h is the heat transfer coefficient, A is the area

exposed to convection, and T_∞ is ambient temperature. Finally, the term $uR_oI_o^2$ represents electric heating of the PFC, where R_o is the heater's effective resistance, I_o is the nominal current flowing through the heater when it is turned on, and u is an adjustable pulse width modulation (PWM) duty ratio for the heater. This PWM duty ratio is constrained to have a value between 0 and 1. Note that the above model is used for controlling the setup's two sets of electric heaters, keeping in mind that additional heating/cooling functionalities are provided in an open-loop manner by the setup's heat exchangers.

Figure (2.9) shows the PI loop used for temperature control in the CO_2 removal chamber. The plant dynamics block in the figure represents Eq. (2.2). The difference, $E(s)$ between the desired reference temperature, $R(s)$, and actual temperature, $T(s)$, is passed through a PI controller, $k_p + k_I/s$, with a proportional gain k_p and integral gain k_I, in order to produce a PWM ratio $U'(s)$. This PWM ratio is then passed through a saturation function in order to ensure that the final commanded PWM ratio, $U(s)$, lies between 0 and 1. If the saturation function is active, meaning that there is a difference between the signals U' and U, then the integral feedback functionality is disabled in order to prevent integrator windup. When the saturation function is inactive, the resulting closed-loop expression for the PFC temperature, $T(s)$, ensures ideal steady-state target temperature tracking in the presence of constant ambient and inflow temperature disturbances, as expected:

$$T(s) = \frac{\rho Q C_p T_{in} + hAT_\infty + (k_p s + k_I)R_o I_o^2 R(s)}{s(\rho C_p(Vs + Q) + hA) + (k_p s + k_I)R_o I_o^2} \tag{2.3}$$

Temperature control for the CO_2 removal chamber was tuned by fitting the open-

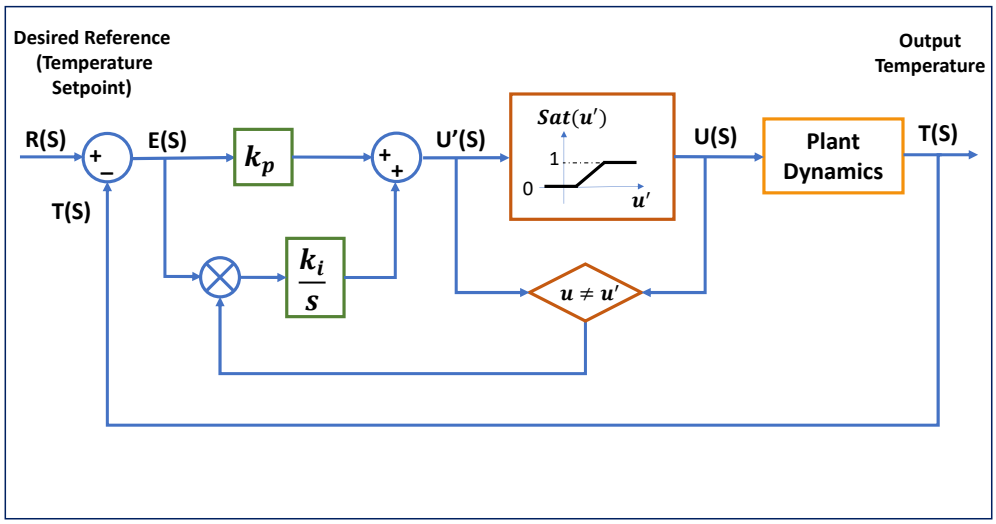

Figure 2.9: Closed-loop temperature control

loop dynamics of Eq. (2.2) to an experimental step response test, then using classical pole placement to set the gains k_p and k_I. A similar process was used for tuning the gains of the final perfusion temperature controller, with one important caveat compared to the CO_2 chamber temperature controller. Specifically, because the final perfusion heater is mounted directly on a metal pipe carrying PFC, as opposed to being immersed in a canister containing PFC, it is significantly more vulnerable to overheating. This vulnerability is particularly noticeable for small or zero PFC flowrates. To address this, the final perfusion heater's controller contains an additional term that brings the corresponding PWM ratio quickly to zero if the temperature of the final perfusion heater exceeds $55°C$. When this function is activated, integral control is disabled in order to prevent integrator windup.

2.4.4 Perfusion Flowrate and Pressure Control

The final perfusion controller dictates the flowrate command to the perfusion pump. The controller allows its user to select between two modes: a manual mode and an au-

tomatic mode. In both modes, the controller determines a raw flowrate command, $Q'(t)$. In the manual mode, this flowrate command is equal to $k_{ff}Q_{des}(t)$, where $Q_{des}(t)$ is the flowrate dictated by the setup's user through its GUI, and k_{ff} is a feedforward calibration constant determined through setup testing. In the automatic mode, the flowrate command is related to the user-defined desired flowrate as follows:

$$\begin{aligned} Q'(t) &= k_{ff}Q_{des}(t) \\ &\quad +I(t)k_q \int_0^t (Q_{des}(\tau) - Q_{meas}(\tau))d\tau \\ &\quad +(1 - I(t))k_c \int_0^t (P(\tau) - P_{set})d\tau \end{aligned} \tag{2.4}$$

In the above control law, $P(t)$ denotes peritoneal cavity pressure, and P_{set} is a user-defined pertioneal cavity setpoint pressure that should ideally not be exceeded for prolonged time durations. A dimensionless indicator function, $I(t)$, is defined as being equal to 1 when $P(t) > P_{set}$, and being equal to 0 otherwise. Therefore, when this indicator function equals 1, the implication is that the peritoneal cavity pressure setpoint has been exceeded. The volumetric flowrate, $Q'(t)$, is governed by three terms: a feedforward term identical to the one used for manual flow control, plus two integral feedback terms. The controls gains for these three terms are denoted by k_ff (dimensionless) for the feedforward gain, k_q (units: s^{-1}) for the integral flowrate correction gain, and k_c (units: $m^3Pa^{-1}s^{-2}$) for the integral pressure correction gain. Only one of the above integral feedback terms is active at any given time. When peritoneal cavity pressure exceeds the setpoint pressure, an integral controller with a gain k_c is used for bringing cavity pressure

down to the setpoint. In contrast, when peritoneal cavity pressure is below the setpoint, an integral controller with a gain k_q is used for matching the true perfusion flowrate measured by the flowrate sensor, $Q_{meas}(t)$, to the desired flowrate dictated by the user. The actual flowrate command communicated to the perfusion pump is equal to $Q'(t)$ from the above equation, with the exception of two extreme conditions:

- First, when the fluid level in the oxygenation tank drops below a certain minimum level, the perfusion pump controller enters a temporary discrete-event state where perfusate flowrate is curtailed by 50% while the oxygention tank is replenished. This prevents the excessive emptying of the oxygenation tank.

- Second, when cavity pressure exceeds a user-defined safety limit $P_{max} > P_{set}$, the perfusion pump controller enters a different temporary discrete-event state where perfusion is completely disabled.

The intent of the above perfusion flowrate control algorithms is to ensure steady-state tracking of a user-defined desired perfusion flowrate during normal operation. For safety reasons, this is interrupted when perfusion pressures increase beyond a user-defined setpoint and/or safety limit, or when the oxygenation chamber becomes excessively empty.

2.5 Laboratory animal experiment's results

Four animal experiments have been conducted to date, as illustrated in Fig. (2.10). These experiments employed different functionalities in the above setup. For example, the first animal experiment did not employ active suction for drainage of PFC from the

Figure 2.10: The first and second animal experiment

test animal, whereas the next 3 animal experiments did. Moreover, the first two animal experiments employed a single-canister accumulator, whereas the third and fourth experiments predominantly employed a dual-canister accumulator. The purpose of this section is to discuss the efficacy of the setup's data acquisition and control functionalities, from a mechatronics perspective. Future work will build on these results, with a deeper focus on the viability of the setup's use for supplementing test animal gas exchange. Seven lessons are visible from experiments performed with the setup to date:

First, the setup is capable of rapidly oxygenating its stored Perfluorodecalin. Figure (2.11) illustrates this by plotting the open-loop commanded flowrate of oxygen into the oxygenation chamber (blue) and the resulting measured percentage of dissolved oxygen in the PFC as a function of time (red), during one of the animal experiments. A rapid increase in dissolved oxygen percentage is achieved while the PFC is recirculated through

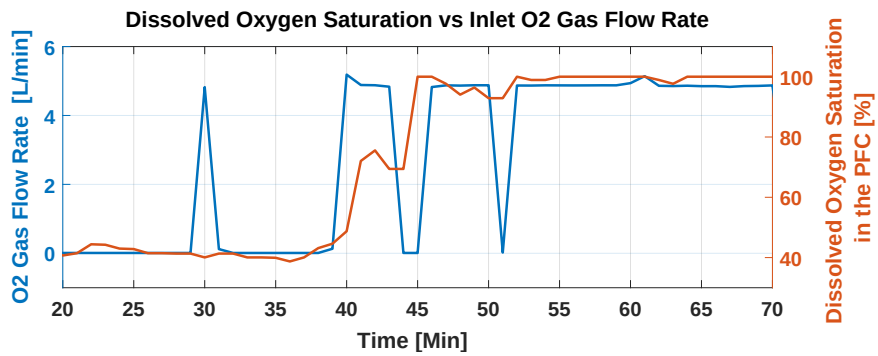

Figure 2.11: Illustration of setup oxygenation performance

the setup, in preparation for one of the perfusion events.

Second, the setup is capable of monitoring and controlling the temperature at which CO_2 stripping takes place. Figure (2.12) (a) illustrates this, by highlighting the setup's CO_2 tank reference temperature tracking performance during a portion of the second animal experiment. Good reference tracking is achieved, with a very small steady-state error corresponding to slight overheating of the PFC. As expected, once the PFC reaches this slightly overheated state, the PWM command to the CO_2 tank heaters drops mostly to zero.

Third, the setup is capable of monitoring and controlling the temperature of the PFC at the final perfusion line. Figure (2.12) (b) illustrates this by plotting perfusion temperature versus time for a portion of the second animal experiment.

Fourth, the setup is capable of both monitoring and controlling the final perfusion flowrate, in compliance with user input. Figure (2.13) illustrates this by comparing the commanded (blue) versus measured (red) PFC flowrate profiles during a portion of the third animal experiment. The setup was operated in manual flowrate control mode during this particular experiment, as opposed to automated control mode. Therefore, Fig. (2.13)

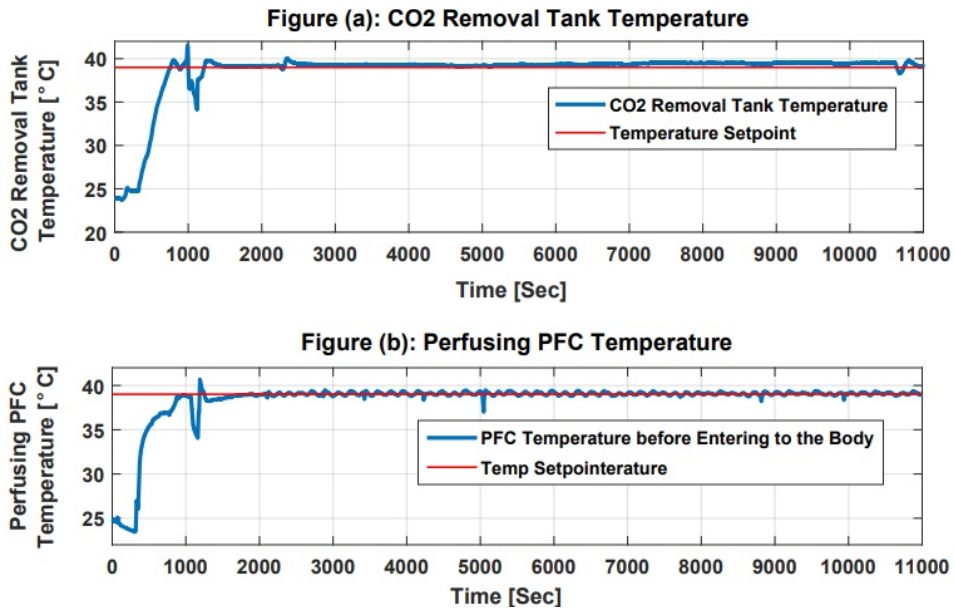

Figure 2.12: CO2 removal tank and perfusing PFC temperatures (second animal experiment)

illustrates successful feedforward control tuning, as opposed to successful steady-state flowrate command tracking through integral action.

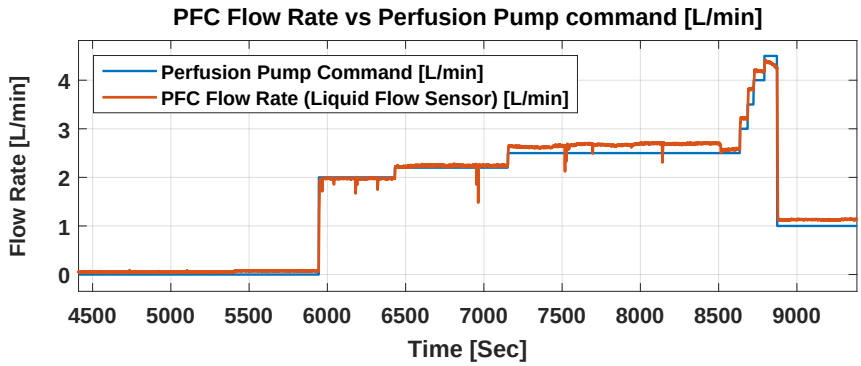

Figure 2.13: Measured vs. commanded PFC flowrate (third animal experiment)

Fifth, the setup is capable of detecting and avoiding excessive peritoneal intracavity pressures. Figure (2.14) illustrates this by plotting the setpoint cavity pressure (red) versus measured cavity pressure (blue) for a portion of the third animal experiment. Excursions beyond the setpoint pressure are brief. Moreover, they are followed by rapid curtailment

of fluid flowrate (not shown), leading to rapid curtailment of cavity pressure. Negative cavity pressures at the end of the plot are indicative of the use of active suction for fluid retrieval.

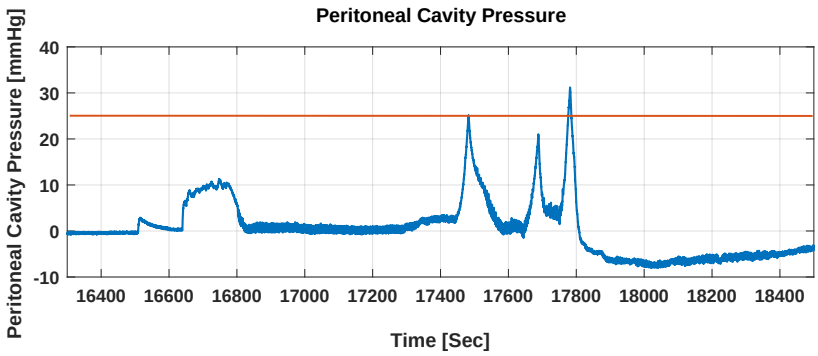

Figure 2.14: The peritoneal cavity pressure measurement vs the pressure setpoint (Data from the third animal experiment)

Sixth, the setup provides sufficient data for assessing the viability of perfusion for oxygenating the test animal. Figure (2.15) illustrates this by showing data from one of the animal oxygenation events. Specifically, the figure plots the animal pulse oximetry (blue) and PFC flowrate (red) versus time. The initial decline in pulse oximetry corresponds to a change in ventilator settings inducing hypoxia. Subsequent improvements in pulse oximetry may be due to a combination of physiological recovery by the animal and/or PFC perfusion. Analyzing the viability of perfusion for improving pulse oximetry is an open topic for ongoing research, exploiting this chapter's setup. However, the figure clearly shows that the setup is capable of measuring key variables that can be used for this type of analysis.

Finally, the setup provides sufficient data for assessing the viability of CO_2 removal from test animals. Figure (2.16) illustrates this by plotting perfusion flowrate, inspired CO_2 concentration, and end-tidal CO_2 concentration for a portion of the second

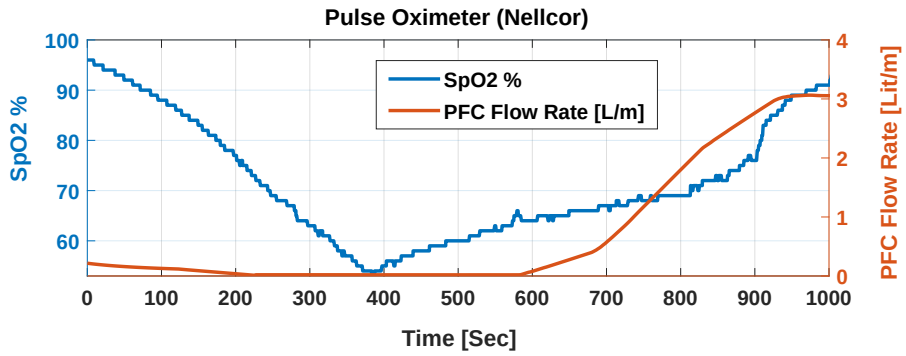

Figure 2.15: Perfusate flowrate and pulse oximetry (second animal experiment)

animal experiment. Hypercarbia is induced, in this case, through a reduction in minute ventilation. Improvements in end-tidal CO_2 concentration (ETCO2) may be caused by physiological recovery mechanisms or perfusion, or a combination of both effects. Analyzing these different recovery mechanisms is left open for ongoing research, building on the setup described in this chapter. Please note that the setup's capnograph measures gas concentrations in an endo-tracheal tube, and infers both inspired and end-tidal CO_2 concentrations from tracheal measurements. Therefore, changes in inspired gas concentration (FICO2) measurements are likely to reflect gas mixing and re-breathing in the endo-tracheal tube.

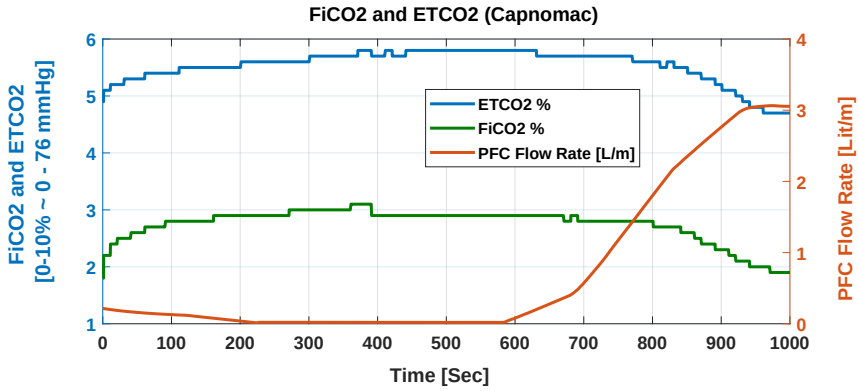

Figure 2.16: Inspired and end-tidal CO_2 concentrations and perfusate flowrate (second animal experiment)

2.6 Modeling "third lung" CO_2 transport dynamics

Animal experiments conducted using the above setup make it possible to build simple, control-oriented models of "third lung" gas transport dynamics. This section develops and parameterizes one such model - namely, a model of "third lung" CO_2 mass transport. The intent of the model is to examine the feasibility of using Perfluorodecalin to remove CO_2 from a hypercarbic test animal.

One of the difficulties in developing mathematical models is to decide what structural features need to be included in a mathematical model to capture certain phenomena. This is particularly challenging in biological systems where processes occurring on multiple scales need to be considered simultaneously. For example, gas exchange takes place between compartments such as the alveoli, vasculature, and tissue, with potentially different time constants associated with different transport phenomena/steps/compartments. This section present a three-compartment CO_2 transport model, including the lung, the vasculature, and the PFC in the peritoneal cavity during perfusion. The intent of the model is to capture the rate of change of CO_2 partial pressure in each compartment under some simplifying assumptions. The model has two input variables, namely, the lung minute ventilation rate (i.e., the inhalation rate in liters per minute) and the perfusate PFC flow rate (also in liters per minute). The model's output is the predicted end-tidal carbon dioxide partial pressure, $ETCO_2$ (in $mmHg$). Figure (2.17) shows the compartments and their connections. The symbols V_l, V_v, and V_p denote the effective volumes of the lung, vasculature, and peritoneal compartments, respectively. Moreover, the symbols P_l, P_v, and P_p denote the partial pressures of CO_2 in these three compartments, respectively.

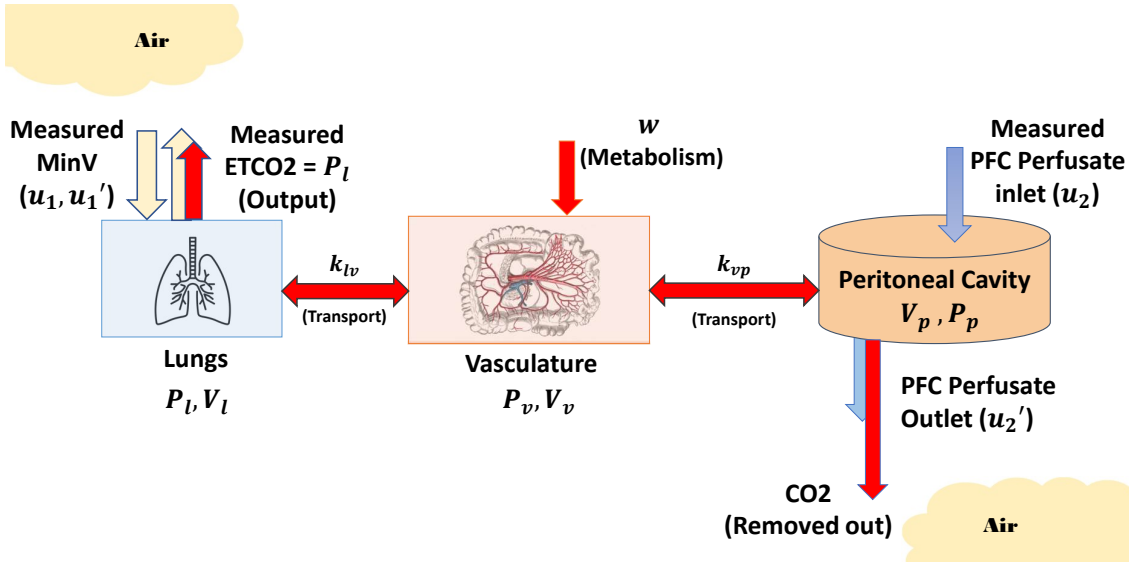

Figure 2.17: A three-compartment model for representing the CO_2 removal dynamics.

The filled volumes of the lung and peritoneal cavity compartments change as a result of inhalation, exhalation, and perfusion. To account for this, Fig.2.17 uses different symbols to refer to inhalation rate (u_1), exhalation rate (u_1'), perfusate inflow into the animal (u_2), and perfusate outflow from the animal (u_2'). Neglecting fluid compressibility, one can therefore write the following differential equations for the real-time filled volumes of the lung and peritoneal cavity:

$$\frac{dV_l}{dt} = u_1 - u_1' \tag{2.5}$$

$$\frac{dV_p}{dt} = u_2 - u_2' \tag{2.6}$$

For simplicity, the remainder of this chapter assumes the dynamics of CO_2 transport to be sufficiently slow compared to the dynamics of the filling and emptying of the lung and peritoneal cavity. This assumption makes it possible to simplify the above equa-

tions by approximating the cavity filling dynamics as being infinitely fast, and therefore always at steady state. Doing so is referred to as *model residualization* (a specific type of *model reduction*) in the dynamic systems literature. Such residualization implies that the filled volumes of the lung and peritoneal cavity, V_l and V_p are approximately constant, respectively. Moreover, this residualization leads to the conclusions that $u_1 \approx u_1'$ and $u_2 \approx u_2'$.

One common assumption in multi-compartment dynamic system modeling is that the concentration (or partial pressure) of the species of interest is spatially uniform within each compartment. Another common assumption is that advective mass transport from any compartment to another occurs at the concentration of the source compartment. For example, the air that enters the lungs has a CO_2 concentration identical to ambient air, whereas the exhaled air has a CO_2 concentration identical to the concentration in the lung compartment. We assume, for simplicity, that carbon dioxide is removed perfectly from PFC prior to perfusion, and that CO_2 concentration in inhaled air and incoming PFC is therefore equal to zero. Given these assumptions, one can apply the law of conservation of mass to each of the three compartments to obtain the following state equations:

$$\begin{aligned}
\frac{d}{dt}\left(\frac{P_l}{R'T}V_l\right) &= u_1(0) - u_1'\frac{P_l}{R'T} + k_{lv}(P_v - P_l) \\
&= -u_1\frac{P_l}{R'T} + k_{lv}(P_v - P_l) \\
\frac{d}{dt}\left(P_v H_v V_v\right) &= k_{lv}(P_l - P_v) + k_{vp}(P_p - P_v) + w \\
\frac{d}{dt}\left(P_p H_p V_p\right) &= k_{vp}(P_v - P_p) - u_2 P_p H_p
\end{aligned} \tag{2.7}$$

In the above state-space model, R' is the ideal gas constant for CO_2, and T is CO_2 gas temperature (assumed constant). Therefore, by the ideal gas law, $P_l/R'T$ is the density of exhaled CO_2. The product of this density withe the lung volume quantifies the mass of CO_2 in the lung compartment. Moreover, the rate of change of this mass is governed by advection to exhaled breaths and by transport between the lungs and vasculature. This transport is assumed to be a linear function of the difference in partial pressure between these two compartments, with some proportionality constant k_{lv}. Similarly, a proportionality constant k_{vp} governs the rate of diffusive mass transport between the vasculature and the peritoneal cavity. The coefficients H_v and H_p are Henry's law constants for the vasculature and peritoneal cavity compartments, respectively, and w is a metabolic CO_2 mass generation rate, assumed to be constant for simplicity.

To fit the above model to animal test data, one must estimate both the constant parameters in the model as well as the model's initial conditions. Since this is a three-compartment model, three initial conditions are required for its three state variables. One can simplify this estimation exercise by exploiting time scale separation to residualize the model further. The time constants associated with two of this model's three compartments - namely, the lung compartment and peritoneal cavity compartment - are governed at least partially by the rates at which these compartments are replenished with external fluid, respectively. For instance, the larger the inhalation/exhalation rate, u_1, compared to the lung volume, V_l, the faster the lung gas dynamics will generally be. With this in mind, this chapter residualizes the lung and peritoneal cavity gas dynamics, leading to a first-order gas exchange model. To illustrate this residualization process, consider the dynamics of

the lung compartment:

$$\frac{d}{dt}\left(\frac{P_l}{R'T}V_l\right) = -u_1\frac{P_l}{R'T} + k_{lv}(P_v - P_l) \tag{2.8}$$

Approximating these dynamics as being infinitely fast compared to the dynamics of the vasculature compartment is equivalent to setting the left hand side of hte above equation to zero, thereby obtaining:

$$0 \approx -u_1\frac{P_l}{R'T} + k_{lv}(P_v - P_l) \tag{2.9}$$

Solving the above equation provides the following quasi-steady expression for the partial pressure of CO_2 in the lung compartment:

$$P_l = \frac{k_{lv}}{k_{lv} + u_1/R'T}P_v \tag{2.10}$$

Finally, plugging the above expression into the state equation for the partial pressure of CO_2 in the vasculature compartment leads to the following state equation:

$$\dot{P}_v H_v V_v = -k_{lv}\frac{u_1/R'T}{k_{lv} + u_1/R'T}P_v + k_{vp}(P_p - P_v) + w \tag{2.11}$$

In the above state equation, the term $k_{lv}\frac{u_1/R'T}{k_{lv}+u_1/R'T}P_v$ represents diffusion-based CO_2 mass transport from the vasculature compartment to the lung compartment, assuming that the latter compartment's dynamics are infinitely fast. The mathematical structure of this term reveals a diminishing gas transport benefit associated with higher and higher breathing rates. For small values of the inhalation/exhalation rate, u_1, CO_2 mass trans-

port increases approximately linearly with u_1. However, for values of u_1 much larger than $k_{lv}R'T$, mass transport is governed predominantly by the constant k_{lv}. This observation makes intuitive sense: it suggests that faster breathing benefits CO_2 transport only up to the point where diffusion-based transport between the vasculature and the lungs becomes the rate-limiting transport phenomenon.

Applying a similar residualization to the peritoneal cavity's CO_2 dynamics simplifies the above state-space model further, to the point where it is governed by a single state equation:

$$\dot{P}_v H_v V_v = -k_{lv}\frac{u_1/R'T}{k_{lv} + u_1/R'T}P_v - k_{vp}\frac{u_2/R'T}{k_{vp} + u_2/R'T}P_v + w \tag{2.12}$$

The above state equation highlights the desirability of increasing the PFC flowrate, u_2, from the perspective of mass transport. Specifically, the equation predicts that higher PFC perfusion flowrates will improve mass transport, at least up to a point of diminishing returns where u_2 is much larger than $k_{pv}R'T$. This creates motivation for pushing PFC perfusion flowrates to high values. Unfortunately, doing so comes with the risk of elevated peritoneal cavity pressures, and possibly compartment syndrome. Taking this into account, this chapter makes the conservative assumption that the PFC perfusion flowrate, u_2, is sufficiently small to the point where is may potentially be much smaller than $k_{vp}R'T$. This makes it possible to simplify the above state equation as follows:

$$\dot{P}_v H_v V_v = -k_{lv}\frac{u_1/R'T}{k_{lv} + u_1/R'T}P_v - \frac{u_2}{R'T}P_v + w \tag{2.13}$$

This concludes the chapter's effort to model "third lung" CO_2 gas transport dynam-

ics. Specifically, the remainder of this chapter will use the above three-compartment gas transport model, residualized to a single compartment - namely, the vasculature compartment. Lumping this model's parameters allows it to be rewritten in terms of the following state and output equations:

$$\dot{P}_v = -a_1 \frac{u_1}{a_2 + u_1} P_v - a_3 u_2 P_v + a_4, \tag{2.14}$$

$$P_l = \frac{1}{1 + u_1/a_2} P_v \tag{2.15}$$

where the output equation provides a quasi-steady expression for ETCO2 in terms of the partial pressure of CO_2 in the vasculature compartment, and the constants in this final state-space model are given by: $a_1 = \frac{k_{lv}}{H_v V_v}$, $a_2 = k_{lv} R' T$, $a_3 = 1/R' T H_v V_v$, and $a_4 = \frac{w}{H_v V_v}$.

2.7 Parameterizing "third lung" CO_2 dynamics

Given the above residualized three-compartment model, the next goal of this chapter is to identify the parameters of the model from experimental data. Four animal experiments have been conducted to date. A shortage of PFC, combined with a lack of active suction, caused the first animal experiment to terminate without successful PFC drainage. Moreover, significant drops in real-time tidal volume during perfusion resulted in failure to realize the gas transport benefits of PFC perfusion during the third and fourth animal experiments. These drops in real-time tidal volume appear to have been caused by a leak-

age in the mechanical ventilator utilized for inducing hypoxia and hypercarbia, discovered after the fourth animal experiment. Given this mixed history of animal tests, the current model parameterization exercise focuses on the second animal experiment, where significant gas transport benefits were successfully realized through peritoneal PFC circulation. Two hypercabia episiodes were induced during the second animal experiment through the deliberate manipulation of real-time tidal volume. The first hypercarbia episode was induced without PFC perfusion, whereas the second hypercabia episode was induced with PFC perfusion. Together, data sets gathered during both hypercarbia episodes were used for identifying the parameters of the above state-space model. Specifically, optimization was used for estimating the values of the parameters $a_{1.2.3.4}$, plus the initial partial pressure of CO_2 in the vasculature compartment at the beginning of each hypercabia episode.

Figures (2.18) and (2.19) show the results of the above parameterization exercise. The top plot in each figure is the animal's real-time minute ventilation (i.e., inhalation/exhalation) rate. The middle plot in each figure is the volumetric flowrate at which PFC is supplied to the animal. Figure (2.18) corresponds to a hypercarbia attempt with no perfusion, whereas Fig. (2.19) corresponds to a perfusion attempt. The bottom plot in each figure compares the measured animal ETCO2 to the predictions of the proposed model. The model's parameters are obtained by solving a single optimization problem covering both hypercarbia episodes simultaneously. This probelm can be written as fol-

lows:

$$
\begin{aligned}
&\min_{a_{1,..,4},\hat{P}_v(T_1),\hat{P}_v(T_2)} \sum_k \left[y_m(t_k) - \hat{y}(t_k)\right]^2 \\
s.to : \dot{\hat{P}}_v &= -a_1 \frac{u_1}{a_2 + u_1} \hat{P}_v - a_3 u_2 \hat{P}_v + a_4 \\
\hat{y}(t) &= \frac{1}{1 + u_1(t)/a_2} \hat{P}_v(t)
\end{aligned}
\tag{2.16}
$$

In the above problem statement, the goal is to minimize the sum of the squared ETCO2 prediction errors over all moments in time, for both of the above hypercarbia episodes. The index k refers to different moments in time when ETCO2 is sampled experimentally, and the ranges of values of k are selected to correspond to the two hypercarbia episodes. Optimization proceeds with respect to the initial conditions for the partial pressure of CO_2 in the vasculature compartment, as well as the parameters $a_{1.2.3.4}$. The proposed gas exchange model is applied as a dynamic constraint on the optimization problem, Because of the diminishing impact of inhalation rate on gas exchange, as well as the bilinearity of the gas transport dynamics (i.e., the fact that gas transport depends on the products of volumetric flowrates and partial pressures), this is a nonlinear, non-convex optimal estimation problem. A particle swarm algorithm is used for solving this non-convex problem, leading to the curve fits in Figures (2.18,2.19).

The curve fits in Figures (2.18,2.19) correspond to the following parameter values: $a_1 = 5.6 \times 10^{-3}$, $a_2 = 7.89$, $a_3 = 1.55 \times 10^{-4}$, and $a_4 = 3.1 \times 10^{-2}$. Moreover, the optimal initial partial pressures of CO_2 in the vasculature compartment, corresponding to these curve fits, are 48.9 and 48.7 mmHg for the episodes without and with perfusion,

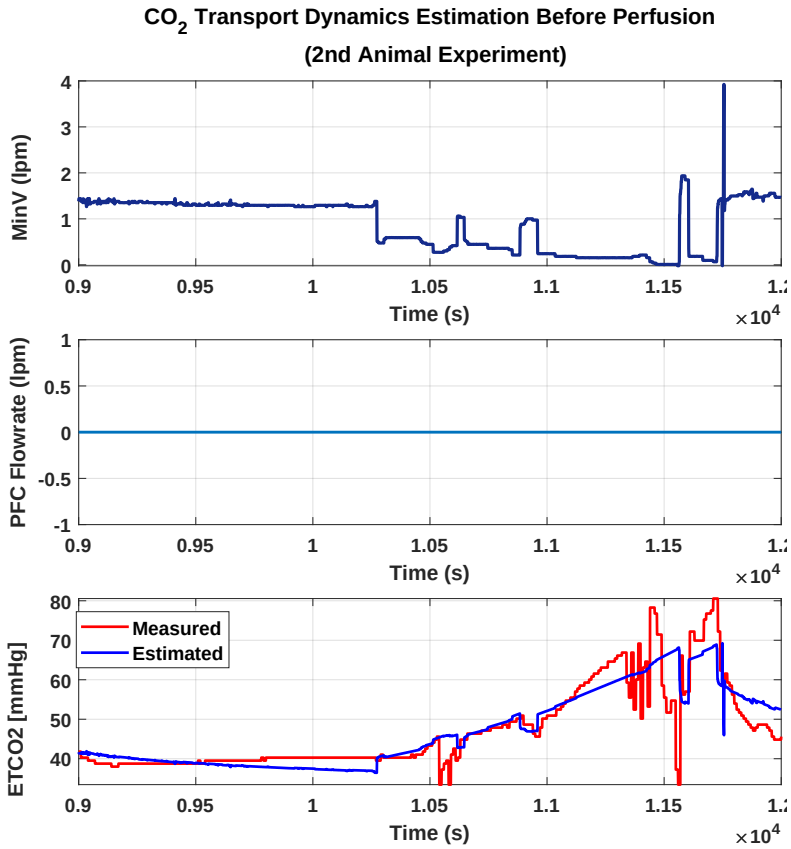

Figure 2.18: Estimated vs. measured $ETCO_2$ without perfusion.

respectively. Perhaps the most important of the above parameter/state estimates, for the purposes of this chapter, is the estimate of a_3. This estimate suggests that for each additional liter per minute of PFC perfuste flow, the test animal is able to reduce its vasculature compartment's partial pressure of CO_2 by 1.55×10^{-4} mmHg per second for each mmHg of this partial pressure. For example, if the partial pressure of CO_2 in the vasculature compartment is 45 mmHg, and if PFC is perfused through the animal at 3 liters per minute, then perfusion will reduce this partial pressure by $3 \times 45 \times 1.55 \times 10^{-4} \times 60 \approx 1.26$ mmHg per minute. Comparing this number to $60a_4 = 60 \times 3.1 \times 10^{-2} \approx 1.86$ mmHg

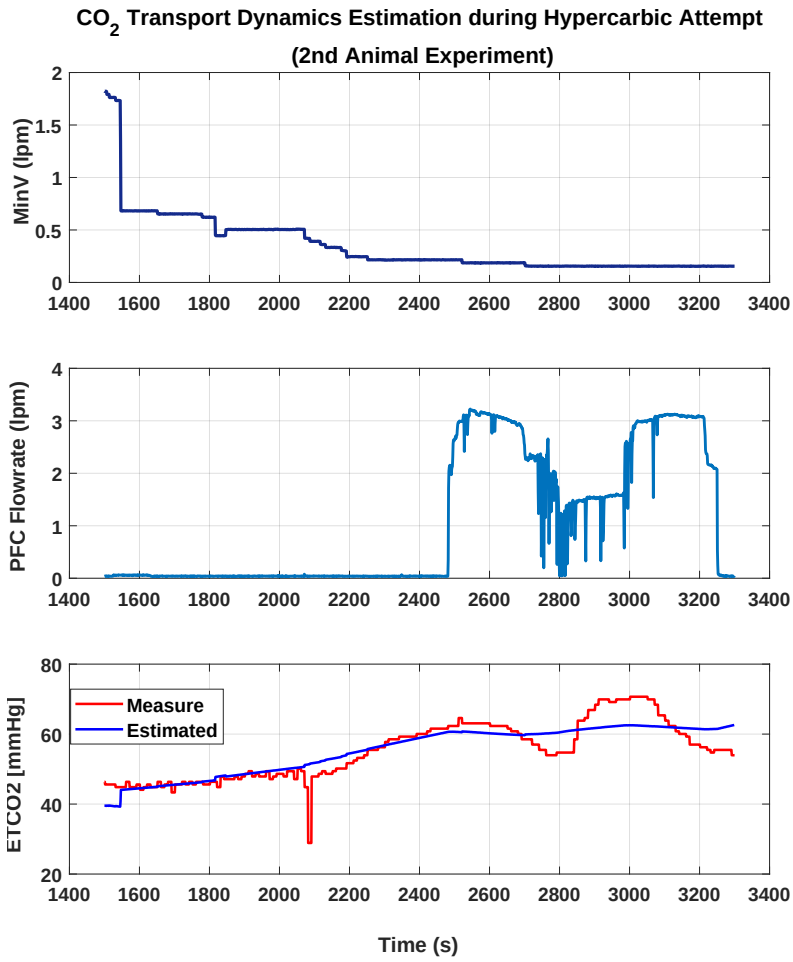

Figure 2.19: Estimated vs. measured $ETCO_2$ with perfusion

per minute suggests that PFC perfusion, alone, at a volumetric flow rate of 3 liters per minute, is capable of removing approximately 68% of all the CO_2 generated by the test animal during perfusion, assuming a CO_2 partial pressure of 45mmHg in the vasculature compartment.

The above result, while quite encouraging, must be taken with a grain of salt. Uncertainty quantification tools such as Fisher information analysis can help provide confidence bounds on this result, as discussed in the next section of this chapter.

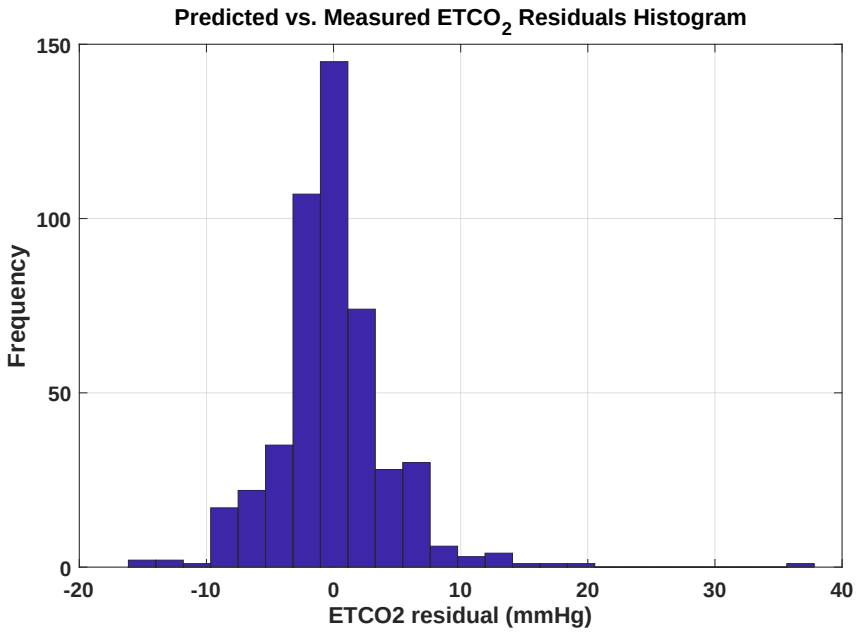

Figure 2.20: Histogram of ETCO2 residuals

2.8 Identifiability analysis for "third lung" CO_2 dynamics

Figure (2.20) shows a histogram of the ETCO2 prediction errors - or residuals - for the two hypercarbia episodes examined in this chapter. Moreover, Fig. (2.21) shows the autocorrelations of these residuals. Both figures are generated for a sampling time step of 10 seconds, corresponding to the communication time step of the capnograph used in third lung animal experiments. Together, these two figures suggest that the ETCO2 prediction residuals may not be independent, identically distributed, and Gaussian. One possible explanation for this observation may be that the ETCO2 measurement noise is, itself, not independent, identically distributed, and Gaussian. Another possible explanation may be that the simple model used in this chapter for predicting ETCO2 does not necessarily capture the full dynamics of test animal gas transport. In addition to these observations, it

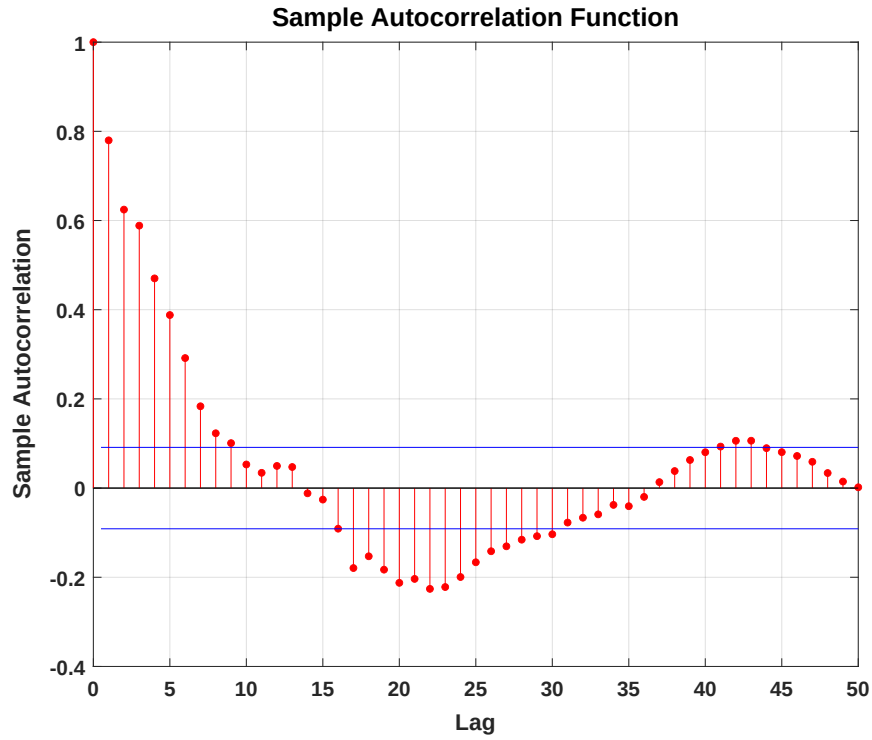

Figure 2.21: Auto-correlation of ETCO2

is important to note that the nonlinearity of the assumed ETCO2 gas transport dynamics in terms of the underlying estimation parameters implies that Fisher information analysis will furnish a local - as opposed to global - quantification of parameter identifiability. Altogether, these observations suggest that the use of Fisher information analysis for ETCO2 model parameter identifiability analysis in this chapter will furnish an imperfect estimate of model parameter identifiability.

With the above important caveats in mind, the proposed gas transport dynamics model was simulated for perturbed values of all six unknown model parameters and initial conditions. The magnitude of the perturbation was set to 0.1% of the nominal value of each parameter, leading to a numerical computation of Fisher information. Based on this numerical computation, the $\pm 3\sigma$ Cramér-Rao estimation bounds on the model's

parameters were found to be as follows: $a_1 = 5.6 \times 10^{-3} \pm 6.15 \times 10^{-4}$, $a_2 = 7.89 \pm 0.78$, $a_3 = 1.55 \times 10^{-4} \pm 1.28 \times 10^{-5}$, and $a_4 = 3.1 \times 10^{-2} \pm 1.3 \times 10^{-3}$.

The above estimation error bounds are encouraging, in the sense that they suggest that the peritoneal perfusion of oxygenated PFC is indeed potentially effective as a mechanism for CO_2 clearance. In particular, the fact that the $\pm 3\sigma$ bounds on the parameter a_3 are both positive suggests that such perfusion is successful in CO_2 clearance, even when modeling and measurement errors are accounted for through uncertainty quantification. This type of uncertainty quantification motivates subsequent work in this dissertation on the Fisher identifiability of multi-compartment dynamic system models. Of particular importance to this dissertation is the question of how the shaping of a given dynamic system's input trajectory affects its underlying parameter identifiability.

2.9 Conclusions

This chapter presents the development, design, and implementation of a peritoneal perfusion setup for studies on animal oxygenation using perfluorocarbon. The chapter also examines the modeling, parameterization, and identifiability analysis for the underlying CO_2 gas transport. The outcomes of this chapter are twofold. First, the research described in this chapter is successful in furnishing a mechatronic setup with the monitoring, data acquisition, and control capabilities needed for extra-pulmonary animal gas transport experiments. Second, analyzing the results of one of the experiments furnishes valuable insights into a primary function of the setup, namely, CO_2 removal. Four animal experiments have been conducted to date using this setup. These animal experiments highlight

the setup's functionalities from an engineering perspective. These functionalities include the ability to monitor and control perfusate flowrate, pressure, and temperature. More importantly, the setup is also capable of simultaneously tracking both physical perfusion variables and physiological animal responses. Based on the results of this study, CO_2 concentration is indeed diminishing as a result of peritoneal PFC perfusion in a hypercarbic test animal. Moreover, the uncertainty quantification of the estimated parameters in this chapter illustrates the accuracy with which the parameters are identified. It is important to mention that diminishing the partial pressure of CO_2 in the vasculature (PCO_2) during peritoneal cavity PFC perfusion for a hypercarbic animal is indeed the goal of the third lung setup, and the residualized model presented in this chapter is actually modeling this dynamic. However, we need to implement a novel sensor for gathering more data to fit the model for PCO_2. There is an ongoing research on designing such a sensor to implement for the next animal experiments within the third lung team to make it possible to actually model for the PCO_2. The question of what factors affect the efficacy of peritoneal PFC perfusion as a gas exchange mechanism remain open for ongoing/future research. Moreover, the related question of the minimum viable level of setup complexity and sophistication for gas exchange also remains open for ongoing/future research. The design of the setup in this study focuses predominantly on achieving a level of sophistication in data acquisition and control that is conducive to scientific exploration, with the recognition that practical clinical implementation may benefit from potential setup simplifications. Perhaps most importantly, the work in this chapter highlights the value of uncertainty quantification tools such as Fisher information analysis in assessing the outcomes of multi-compartment model parameterization experiments. Subsequent chapters

in this dissertation focus on the follow-on fundamental question of how input shaping affects multi-compartment model parameter identifiability.

Chapter 3: Combined State and Parameter Identifiability for a Model of Drug-Resistant Cancer Dynamics

3.1 Overview

This chapter analyzes the combined parameter and state identifiability for a model of a cancerous tumor's growth dynamics. The model describes the impact of drug administration on the growth of two populations of cancer cells: a drug-sensitive population and a drug-resistant population. The model's dynamic behavior depends on the underlying values of its state variables and parameters, including the initial sizes and growth rates of the drug-sensitive and drug-resistant populations, respectively. The chapter's primary goal is to use Fisher identifiability analysis to derive and analyze the Cramér-Rao theoretical bounds on the best-achievable accuracy with which this estimation can be performed locally. This analysis highlights two key scenarios where estimation accuracy is particularly poor. First, a critical drug administration rate exists where the model's state observability is lost, thereby making the independent estimation of the drug-sensitive and drug-resistant population sizes impossible. Second, a different critical drug administration rate exists that brings the overall growth rate of the drug-sensitive population to zero,

thereby worsening model parameter identifiability[1].

The cancerous tumor dynamics model presented in this chapter is largely based on earlier modeling efforts in the literature, and parameterized based on those efforts. This places some limitations on the work included in this chapter. For instance, this work is not fully validated against experimental tumor growth data sets, from either petri dish or animal experiments. As a result, legitimate questions remain open regarding the validity of the tumor model's parameters, particularly the parameters associated with cancerous tumor growth rates. The intent of the chapter is not to assert the correctness of the underlying tumor dynamics model for any particular type of cancer, or to develop directly translatable treatment protocols. Rather, the intent is to explore the fundamental question of how the combined state/parameter identifiability of a multi-compartment cell population dynamics model is potentially influenced by input shaping. From a broad, fundamental perspective, the chapter highlights the degree to which poor input shaping can result in poor identifiability, thereby motivating the use of optimal input shaping in subsequent chapters to improve identifiability.

3.2 Introduction

This chapter examines the Fisher identifiability of drug resistance dynamics in cancerous tumors. The chapter models a tumor as a dynamic system. From a control-theoretic perspective, the "input" to this system is the rate at which the tumor is treated

[1]The work presented in this chapter already appears in publication. Specifically, a preliminary version of this work appears in the peer-reviewed Proceedings of the European Control Conference, focusing solely on initial population observability. Moreover, a complete version of the work appears in the ASME Journal of Dynamic Systems, Measurement, and Control, focusing on combined state/parameter identifiability.

versus time. One example is the rate of drug administration versus time during chemotherapy. The "output" of the system is any measurement used for monitoring the cancer. One example is total tumor size measurement versus time. The chapter focuses on the case where part of the tumor's cell population is sensitive to chemotherapy, and part of the population is resistant to chemotherapy.

Identifiability is an established concept from the fields of system dynamics and information theory [1, 2]. It refers to the degree to which one can estimate a model's internal variables from input-output data. One can classify these variables into constant parameters (e.g., cell mutation rates) versus time-varying state variables (e.g., sizes of the drug-sensitive and drug-resistant cell populations). The terms "parameter identifiability" and "state observability" refer, respectively, to one's ability to estimate these two types of internal variables from input-output data. This chapter focuses on combined state/parameter identifiability. This is a broader concept that refers to one's ability to estimate a given model's state variables and parameters simultaneously. One possible approach for estimating a model's state variables and parameters simultaneously is to treat the parameters and initial states of the model, collectively, as a vector of unknown quantities to be estimated concurrently.

Analyzing combined state/parameter identifiability for a partially drug-resistant cancerous tumor model is, in essence, an exercise in uncertainty quantification. The importance of this exercise stems partly from its potential to serve as a starting point for uncertainty propagation. For example, knowing the uncertainties in one's estimates of a model's internal variables, one can ask: how do these errors propagate to induce further errors in the model's future predictions? Furthermore, how do these prediction errors

affect the accuracy with which one can optimize future treatment protocols? Of particular importance, here, is the choice between aggressive chemotherapy protocols that seek tumor remission versus more benign protocols that favor containment. Aggressive cancer treatment is a standard approach where the goal is to eliminate drug-sensitive cells as quickly as possible, partly in order to lessen the likelihood of the emergence of drug resistance. Such a treatment strategy inherently neglects the potential importance of natural competition between the drug-sensitive and drug-resistant cell populations (for nutrients, etc.) as a means for decelerating the growth of the latter population. Containment strategies, in contrast, typically use less aggressive drug administration rates in order to maintain a clinically acceptable target overall tumor size. By doing so, they encourage the competitive suppression of drug resistance, which can potentially be beneficial for the patient in the long run.

Previous work by Hansen *et al.* shows that the relative merit of aggressive cancer treatment versus containment strategies depends on the relative sizes of the drug-sensitive and drug-resistant cancer cell populations [75]. Specifically, they show that there exists a threshold level of drug resistance, above which containment is optimal. [75] Making an informed cancer treatment decision, therefore, ideally involves the measurement of these two population sizes. Unfortunately, it is difficult to measure the size of the population of drug-resistant cells in a cancer tumor, at least early on during treatment, when this population is very small. This raises the following two questions. First, can the resistant population size be estimated from measurements of overall population size? Second, how accurately can one estimate primary drug resistance (i.e., the initial population of drug-resistant cells, prior to the beginning of treatment) from total population measure-

ments during the cancer treatment phase? The theoretical accuracy with which these models, combined with measurements, can estimate the prevalence of drug resistance remains relatively unexplored. The fields of estimation theory and systems biology provide fundamental tools for assessing the accuracy of an estimator, one example being Fisher identifiability analysis. The goal of this chapter is to use these tools to answer the above questions.

There is a rich existing literature on the identifiability of biological system models, much of it tracing back to Bellman and Åström's seminal work in 1970 [24]. As shown by Jacquez *et al.*, identifiability analysis makes it possible to both estimate the uncertainty in a given model's parameters and optimally design subsequent parameter estimation experiments [76]. The focus in this chapter is on the identifiability of drug resistance dynamics in cancerous tumors. The research in this chapter is motivated by the fact that drug resistance is responsible for a significant portion of chemotherapeutic treatment failures. Drug resistance occurs because of various factors including changes in drug metabolism, mutations, genetic rewiring, and tumor heterogeneity [9, 77, 78]. Regardless of the specific cause of drug resistance, the main outcome is that a portion of the cancerous cell population continues to suffer from defective apoptosis (i.e., controlled cell death) even in the presence of a given drug. Therefore, understanding and predicting the behavior of drug resistant cells is essential for determining an optimal chemotherapeutic treatment schedule. Drug resistance dynamics have been studied from both the mathematical and experimental perspectives [79, 80, 81, 82]. Numerous mathematical models of cancer growth have also been formulated [83, 84, 85, 86, 87, 88, 89, 90, 91, 92]. Among these models, the Gompertz model has been widely used in optimizing treatment protocols [93, 94, 95, 96].

This model considers the slowdown in tumor growth as a function of increasing tumor size.

Identifiability is a challenge in cancer treatment because not all of the internal variables affecting a given tumor's dynamics can be measured directly [92]. For instance, the sizes, growth rates, and mutation rates of various cancer cell populations are often not measured directly. This raises the question of whether one can estimate such quantities from other measurements, such as measurements of total tumor size versus time. Multiple studies in the literature are relevant in addressing this question. For instance, Lebedeva *et al.* use a global sensitivity method to analyze uncertainties in the parameters of biochemical networks involved in cancerous tumors [97]. Raue *et al.* discuss methods for improving identifiability in biological applications. They show that parameter estimation accuracy is related to both the model structure and the information provided by experimental data [98]. Eisenberg *et al.* examine the identifiability and estimability of compartmental cancer models [99]. Wu *et al.* investigate the algebraic identifiability of a third-order HIV/AIDS dynamics model with six unknown parameters. They also study the effect of initial values of state variables on the identifiability of this model's unknown parameters [100]. Xia *et al.* study the identifiability of nonlinear HIV system models [101]. Finally, work by the author examines the observability of drug resistance dynamics in cancerous tumors [102]. To the best of the author's knowledge, this chapter is the first work examining combined state/parameter identifiability for drug resistance dynamics in cancers. The chapter highlights two specific scenarios with particularly poor identifiability. In the first scenario, the rate of drug administration causes the net population growth rates of the drug-sensitive and drug-resistant cell populations to be almost

equal. In this scenario, state observability – and therefore, combined state/parameter identifiability – is lost. In the second scenario, drug administration causes the net growth rate of the drug-sensitive cell population to diminish to zero. This treatment protocol causes parameter identifiability - and, therefore, combined state/parameter identifiability - to be particularly poor. An important insight from the chapter is that a treatment protocol that attempts to maintain a constant drug-sensitive cell population size can worsen identifiability substantially. The remainder of this chapter is organized as follows. Section 3.2 presents the nonlinear cancer dynamics model used in this work. The chapter then proceeds to three different identifiability analysis studies:

- First, Section 3.3 analyzes combined state/parameter identifiability for the nonlinear tumor model. This analysis shows that combined state/parameter identifiability is particularly poor when the rate of mutation of drug-sensitive cells is unknown. Even when this mutation rate is assumed to be known *a priori*, two situations arise where identifiability is poor, corresponding to two different drug administration rates.

- Second, Sections 3.4 and 3.5 provide an explanation for one of the two poor identifiability scenarios. In particular, Section 3.4 shows that the drug administration rate in this scenario corresponds to the loss of state observability for a linearized model of the tumor dynamics. Moreover, Section 3.5 shows that this loss of observability persists in the nonlinear tumor dynamics model.

- Third, Section 3.6 uses both the linearized and nonlinear models of tumor dynamics to show that the second poor identifiability scenario corresponds to a drug admin-

istration rate that maintains a constant sensitive cell population size.

The intent of Sections 3.4-3.6 is to obtain insights into the factors contributing to poor combined state/parameter identifiability for the full nonlinear model of tumor dynamics. Simplifying (i.e., linearizing) the model aids in obtaining these insights, with the goal of shedding light on the more complex, nonlinear model. The main outcomes of the work are: (i) the fact that it pinpoints two scenarios where combined state/parameter identifiability is poor, and (ii) the fact that it provides intuitive insights, supported by simpler models/studies, for this poor identifiability. Section 3.7 concludes the chapter by summarizing these insights.

3.3 Nonlinear model of tumor dynamics

Consider a two-compartment representation of tumor dynamics, where cancer cells are either drug-sensitive or drug-resistant. Let the sizes of these two populations be $S(t)$ and $R(t)$, respectively. Suppose that the sum of these two population sizes, $P(t)$, is a measurable output variable. Moreover, let the dynamics of these populations be governed by the following differential equations [102]:

$$\begin{aligned}
\dot{S} &= [(1-\epsilon)r_s - \mu_s]\,(1-\frac{P}{P_c})S - \alpha D S \\
\dot{R} &= (r_r - \mu_r)(1-\frac{P}{P_c})R + \epsilon r_s(1-\frac{P}{P_c})S \\
P &= S + R
\end{aligned} \tag{3.1}$$

The above model expresses the net rates of change of the two cancer cell population sizes in terms of the current population sizes. The external input to the model, $D(t)$, is a drug administration rate. This drug administration rate has a direct impact only on the sensitive cell population. The constant multiplier α scales this drug administration rate to furnish an effective drug-induced sensitive cell death rate. In the absence of drug administration, the sensitive and resistant cell populations birth rates are r_s and r_r, respectively. Moreover, these populations' death rates are μ_s and μ_r, respectively. The rate at which sensitive cells mutate to become drug-resistant equals ϵr_s, where ϵ is a small mutation fraction. Finally, all of these rates are multiplied by a logistic term, $1 - P/P_c$, where P_c is the carrying capacity of the cancerous tumor. Mathematically, this logistic term makes the cancer dynamics nonlinear. Intuitively, the logistic effect represents a slowdown in tumor growth as the tumor becomes larger, perhaps caused by competition for resources among the sensitive and resistant cells. The presence of the logistic term couples the dynamics of the drug-sensitive and drug-resistant cells in a manner that motivates research on containment protocols. Specifically, the idea behind containment strategies is to maintain a nonzero target total tumor size that slows down the growth of the drug-resistant cell population through competition for resources, represented in this model via the logistic effect. The initial drug-sensitive cell population is taken to be $S(0) = 10^8$ cells, which is 10 times smaller than the clinically detectable population size [103]. The initial drug-resistant cell population is assumed to be a very small fraction of the whole tumor size. We consider it to be only 220 cells initially. Once a tumor is clinically detected, we assume that its size can be measured with a measurement error standard deviation of $\sigma = 10^6$ cells, which corresponds roughly to one milligram of tumor mass. We set the

sampling time for the measurements to $\delta t = 1$ week. Similar to the authors' previous work [102], parameter values for the above model are listed in Table (3.1).

Table 3.1: List of parameters

Parameter	Value [$Week^{-1}$]	Parameter	Value	[Unit]
r_s	0.0256	ϵ	10^{-7}	-
μ_s	0.0026	σ	10^6	[Cell]
r_r	0.0026	α	1	[Cell/D]
μ_r	0.00026	$\delta(t)$	1	[Week]

Table 3.2: List of cell Populations for 10 weeks with minimum ($D = 0$) and maximum ($D = 1$) drug administration rates.

D	Cell Populations	$P_c = 10^{10}$	$P_c = 10^{12}$
D = 0	$S(0)$	10^8	10^8
	$R(0)$	220	220
	$S(10\ Weeks)$	1.225×10^8	1.259×10^8
	$R(10\ Weeks)$	228	228
D = 1	$S(0)$	10^8	10^8
	$R(0)$	220	220
	$S(10\ Weeks)$	5713	5714
	$R(10\ Weeks)$	225	225

Fig. (3.1) shows the evolution of the drug-sensitive and drug-resistant cell populations over a 10-week period, for both a no-treatment scenario ($D = 0$) and an aggressive treatment scenario ($D = 1$). The choice of a 10-week simulation duration, when compared to the rate at which the tumor cell population evolves, reflects a desire to analyze the degree to which the tumor dynamics can be identified early in the evolution of the tumor, thereby guiding subsequent treatment decisions. The plots in Fig. (3.1) are generated for two different carrying capacities, namely, $P_c = 10^{10}$ cells and $P_c = 10^{12}$ cells. In

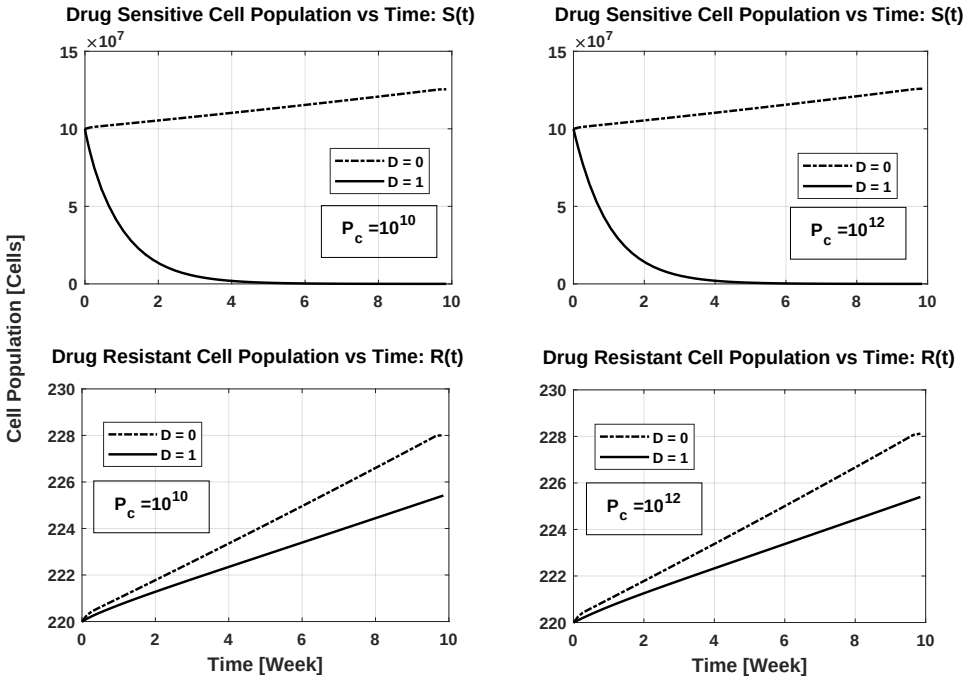

Figure 3.1: Drug-sensitive and drug-resistant cell populations for two different carrying capacities and drug administrations rates.

both scenarios, total tumor size remains well below the corresponding carrying capacity over the examined 10-week duration: a fact that has two main consequences. First, as evident from the figure, drug-resistant population growth is governed predominantly by mutation as opposed to competition during this 10-week period. In other words, the larger the drug-sensitive cell population, the more the drug-resistant cell population grows during this period. Second, one can see from the figure that there is very little difference between the two carrying capacities in terms of the resulting evolution of the two cell populations. We compare these two carrying capacities not because of fundamental differences in overall population growth during this 10-week duration, but rather because of non-trivial differences in identifiability outcomes, as will be seen later in this chapter. The impact of drug administration on sensitive cell population is visible from these plots,

as well as from the corresponding final population size list in Table (3.2). In this work, only the sum of these two populations is assumed to be directly measurable, as opposed to the individual population sizes.

The overarching goal of this chapter is to analyze the identifiability of the time-varying state variables and constant parameters in the above model. Identifiability analysis is, in essence, a two-step process. The first step is to analyze *structural identifiability* by determining whether the state/parameter estimation problem is solvable. The second step is to analyze *numerical identifiability* (often referred to as "practical identifiability" in the literature) by determining the accuracy with which this estimation problem can be solved. Structural identifiability is lost when the impacts of two different internal variables on a dynamic model are indistinguishable from one another. In the above model, for example, equal changes in the growth and death rates of the drug-resistant cells, r_r and μ_r, will not affect overall tumor dynamics. Therefore, treating these two parameters as independent jeopardizes structural identifiability. To avoid this issue, we create three aggregate model parameters, namely, λ_1, λ_2, and ϵr_s, with the first two aggregate parameters defined as shown below,

$$\begin{aligned} \lambda_1 &= (1-\varepsilon)r_s - \mu_s - \alpha D, \\ \lambda_2 &= r_r - \mu_r, \end{aligned} \tag{3.2}$$

where λ_1 and λ_2 are the net growth rate of drug-sensitive and drug-resistant cell population, respectively, and ϵr_s represents the mutation effect. In performing this parameter

aggregation, we focus on the special case where the drug administration rate, $D(t)$, is equal to some fixed constant D, as opposed to the more general case where it varies with time. Rewriting this model in terms of λ_1 and λ_2 furnishes the following equations:

$$\begin{aligned}
\dot{S} &= \lambda_1 S - (\frac{1}{P_c})(\lambda_1 + \alpha D)S^2 - (\frac{1}{P_c})(\lambda_1 + \alpha D)RS \\
\dot{R} &= \lambda_2 R + (\epsilon r_s)S - (\frac{1}{P_c})(\lambda_2 + \epsilon r_s)RS \\
&\quad -(\frac{\lambda_2}{P_c})R^2 - (\frac{\epsilon r_s}{P_c})S^2 \\
P &= S + R
\end{aligned} \tag{3.3}$$

Redefining the model's parameters as shown above eliminates redundancies among these parameters, thereby addressing the structural identifiability issue. This paves the way towards numerical identifiability assessment, which we perform using Fisher information analysis. Fisher information analysis is model-agnostic. However, its outcomes are model-dependent. Therefore, the conclusions of this chapter are closely tied to the above tumor dynamics model.

3.4 Combined State and parameter identifiability for the Nonlinear Model

This section presents a numerical study of combined state and parameter identifiability for the nonlinear tumor model. The study assumes that the effective rate of drug-induced sensitive cell death, αD, is a known constant. Moreover, the study assumes that the remaining three parameters (namely, λ_1, λ_2 and ϵr_s) and initial conditions (namely,

$S(0)$ and $R(0)$) of the tumor dynamics model are unknown. Fisher information analysis provides a convenient method for analyzing the combined identifiability of these parameters and state variables. To perform Fisher information analysis, we begin by defining an output variable, $Y(t, \theta)$, equal to the true total tumor size, i.e., P, at time t, for a given set of values of a combined unknown initial state and parameter vector, θ. Measurements of this output variable are noisy, but the symbol $Y(t, \theta)$ refers to the true output, uncorrupted by noise. The vector θ is, in turn, defined as follows:

$$\theta = \begin{bmatrix} S(0) \\ R(0) \\ \lambda_1 \\ \lambda_2 \\ \epsilon r_s \end{bmatrix} \tag{3.4}$$

Suppose that the above output $Y(t, \theta)$, is measured at moments in time separated by a sampling time $\delta t = 1$ week. Moreover, suppose that the measured output at every sampling instant is equal to the true output plus an independent, identically distributed measurement noise signal with a zero mean and some variance σ^2. In the following analysis, we assume this noise signal to be Gaussian, but Fisher information analysis can be generalized to other noise distributions. Given these assumptions and definitions, let $\mathbf{e}_i$ represent the ith Euclidean vector in the 5-dimensional combined space of unknown parameters and initial values. For instance, let $\mathbf{e}_1 = [1, 0, 0, 0, 0]^T$, $\mathbf{e}_2 = [0, 1, 0, 0, 0]^T$, and so on. Moreover, let $Y(k\delta t, \theta)$ represent the true value of the output, Y, at time $t = k\delta t$, for a given set of unknowns, θ. Then the sensitivity function $s_i(k\delta t)$, can be

defined as follows:

$$s_i(k\delta t) = \lim_{\delta\theta_i \to 0} \frac{Y(k\delta t, \theta + \mathbf{e_i}\delta\theta_i) - Y(k\delta t, \theta)}{\delta\theta_i}, \tag{3.5}$$

where $\delta\theta_i$ represents an infinitesimal change in the ith unknown parameter. Given the above sensitivity function, one can construct the following sensitivity matrix:

$$\mathbf{S} = \begin{bmatrix} s_1(\delta t) & s_2(\delta t) & s_3(\delta t) & s_4(\delta t) & s_5(\delta t) \\ s_1(2\delta t) & s_2(2\delta t) & s_3(2\delta t) & s_4(2\delta t) & s_5(2\delta t) \\ \vdots & \vdots & \vdots & \vdots & \vdots \\ s_1(N\delta t) & s_2(N\delta t) & s_3(N\delta t) & s_4(N\delta t) & s_5(N\delta t) \end{bmatrix} \tag{3.6}$$

where N is the total number of samples over which identifiability analysis is performed. In this study, we choose $N = 10$, the goal being to assess the accuracy with which one can estimate the vector θ after 10 weeks of treatment, recognizing that the total duration of cancer treatment may potentially be longer, especially for containment protocols.

The Fisher information matrix can be constructed from the above sensitivity matrix as follows:

$$\mathbf{F} = \frac{1}{\sigma^2}\mathbf{S}^T\mathbf{S} \tag{3.7}$$

The above computation furnishes a 5x5 matrix. The inverse of this matrix, if it exists, furnishes a local estimate of the Cramér-Rao Lower Bound ($CRLB$) on the best estimation covariance achievable by any unbiased estimator of the vector θ. The condition number of the Fisher information matrix therefore serves as a combined state/parameter identifiabil-

ity metric, with poor (i.e., low) condition numbers indicating poor identifiability, and *vice versa*. Moreover, the diagonal elements of the inverse of the Fisher information matrix provide the best-achievable estimation variance for each element of the vector θ. Dividing each parameter's variance by the nominal value of the parameter squared provides a normalized estimation variance, useful for comparing the accuracy levels with which different parameters can be estimated.

Table (3.3) shows the condition numbers for the above 5x5 Fisher information matrix, for different values of the drug administration rate, D, assuming $\alpha = 1$ and $P_c = 10^{12}$ cells. These condition numbers are computed through numerical simulation, given the nonlinearity of the underlying dynamics. One important conclusion from this table is that combined state/parameter identifiability is very poor across the board, for a broad range of drug administration rates, at least for the tumor carrying capacity under consideration. A poorly conditioned Fisher information matrix indicates that parameter estimation errors are expected to be excessively large, and in fact difficult to evaluate (given the difficult of numerically inverting poorly conditioned matrices). One rule of thumb in identifiability analysis is that attempting to estimate more unknowns leads to poorer identifiability, and *vice versa*. When the parameter ϵr_s is excluded from the above Fisher analysis, for instance, the condition number of the (now 4x4) Fisher information matrix improves considerably. This occurs across the board, for a broad range of drug administration rates. This leads to the insight that the parameter ϵr_s is particularly difficult to estimate accurately from 10 weeks of tumor size measurements, regardless of the drug administration rate. Intuitively, the impact of the mutation process on overall tumor size is quite small over a 10-week duration, resulting in the above difficulty in estimating ϵr_s. Given this

insight, the remainder of this chapter eliminates ϵr_s from Fisher analysis, focusing on the remaining 4 parameters and initial conditions. The underlying question is to what extent can the remaining parameters be estimated if ϵr_s is assumed to be known *a priori*.

Table 3.3: Comparing the reciprocal condition number for different drug administration rates.

D	0.085	0.1	0.5	1
$5 \times 5\ FIM$ (ϵr_s included)	2.01×10^{-32}	1.08×10^{-31}	6.4×10^{-26}	6.3×10^{-24}
$4 \times 4\ FIM$ (ϵr_s excluded)	1.7×10^{-21}	1.03×10^{-21}	2.4×10^{-17}	4.3×10^{-17}

Even when ϵr_s is eliminated from the combined state/parameter estimation problem, identifiability remains a challenge for the tumor model examined in this research, at least for the two tumor carrying capacities of 10^{12} cells and 10^{10} cells. Fig. (3.2) and Fig. (3.3) illustrate this by presenting the normalized estimation variances for the remaining four elements of θ versus different drug administration rates, for two different carrying capacities. From these two figures it is evident that carrying capacity does not affect the specific drug administration rates corresponding to the worst-case identifiability scenarios. The determinant of the corresponding 4x4 Fisher information matrix is plotted versus the drug administration rate in Fig. (3.4). Two particular drug administration rates appear to result in poor combined state/parameter identifiabiliy, namely, $D = 0.02$ and $D = 0.023$. These administration rates correspond to $\alpha = 1$, and can therefore be construed as drug-induced sensitive cell death rates. For example, the scenario where $D = 0.02$ corresponds to a drug-induced sensitive cell death rate of 2% cell deaths per week. In both scenarios, identifiability is sufficiently poor to the point that

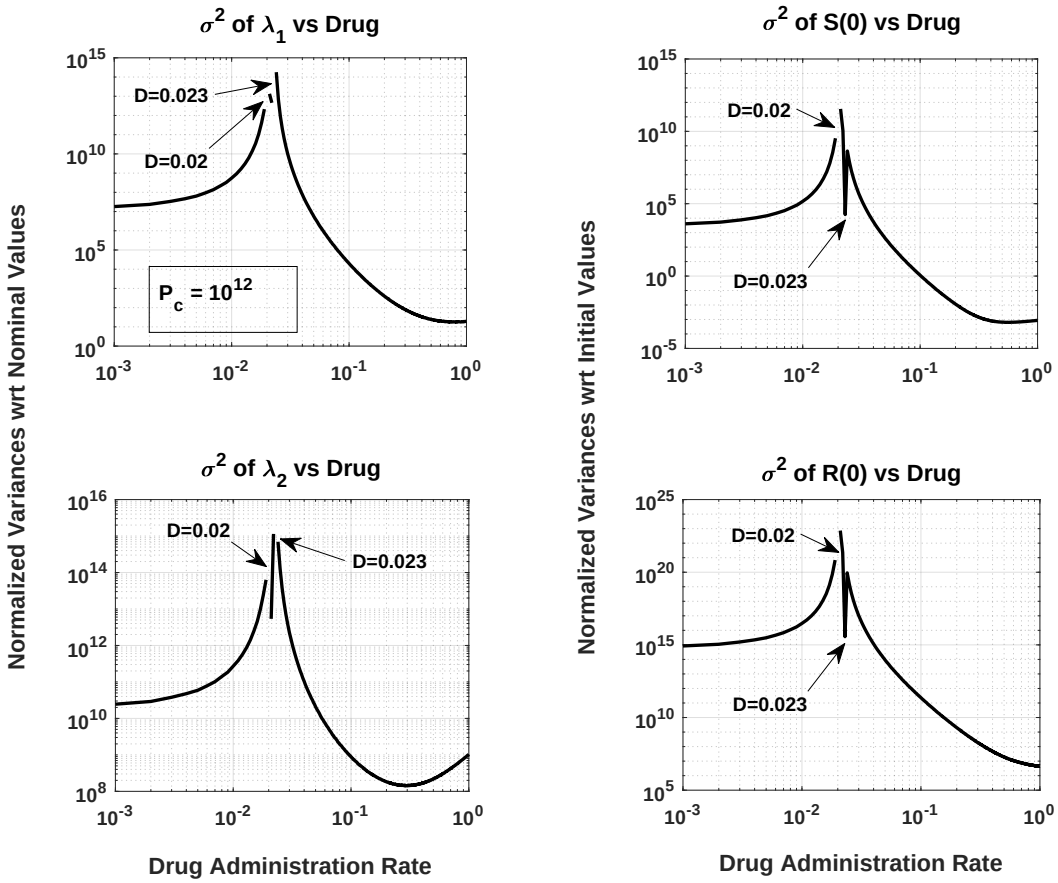

Figure 3.2: Combined states and parameters identifiability for two parameters and two initial states together when $P_c = 10^{12}$.

the Fisher information matrix cannot be inverted numerically, hence the corresponding "gaps" in Fig. (3.2), Fig. (3.3) and Fig. (3.4). The goal of the remainder of this chapter is to obtain insights into the above two poor identifiability scenarios. These insights are obtained by analyzing state observability alone (assuming the tumor model's parameters are known) then analyzing parameter identifiability alone (assuming the tumor model's state variables are directly measurable). We perform these two analyses first using a linearized tumor dynamics model that neglects the logistic effect, then using the nonlinear tumor dynamics model. The intent is to gain insights through the linearized model, then

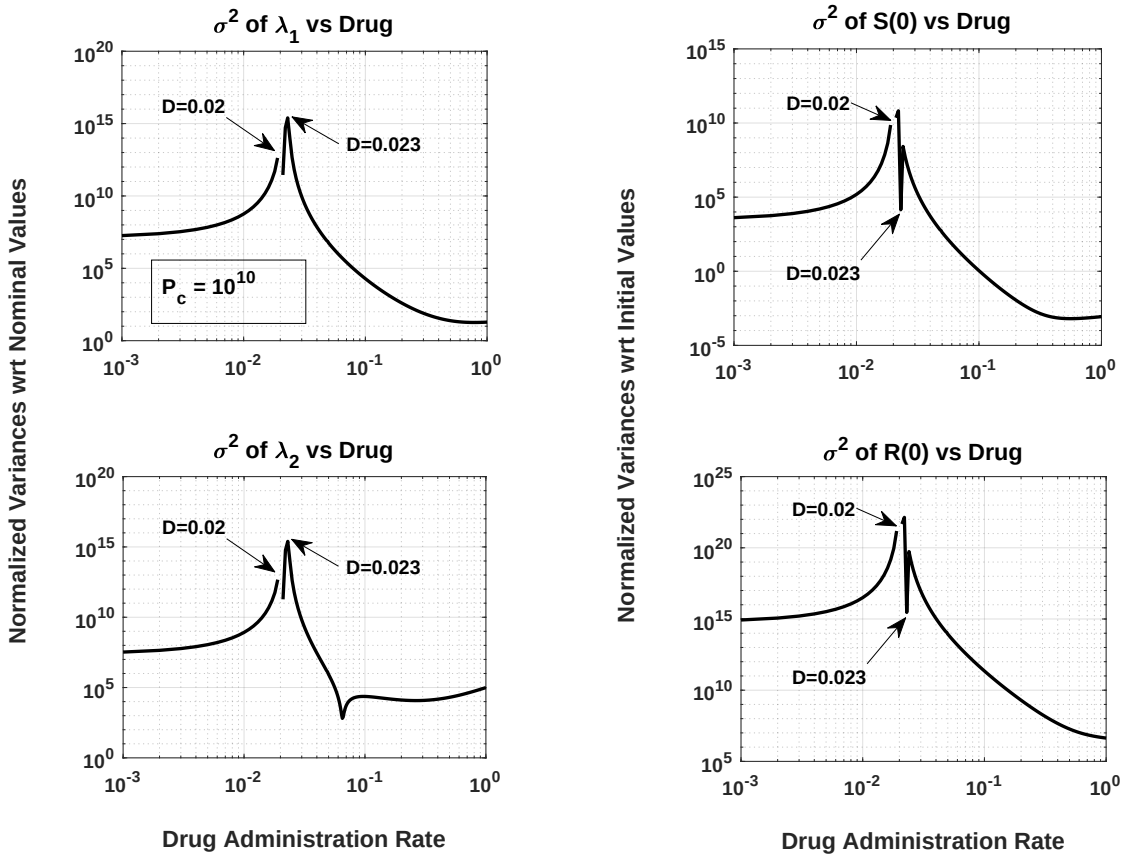

Figure 3.3: Combined states and parameters identifiability for two parameters and two initial states together when $P_c = 10^{10}$.

examine the degree to which these insights continue to hold in the nonlinear case.

3.5 State observability for linear tumor dynamics

A dynamic system model is observable if one can estimate its time-varying internal state variables, assuming that the model (including its parameters) is known and that both its inputs and outputs are measured versus time. In this case, the model's state variables are $S(t)$ and $R(t)$, its input is the drug administration rate $D(t)$, and its output is total population size $P(t)$. The tumor dynamics model is observable if and only if the initial

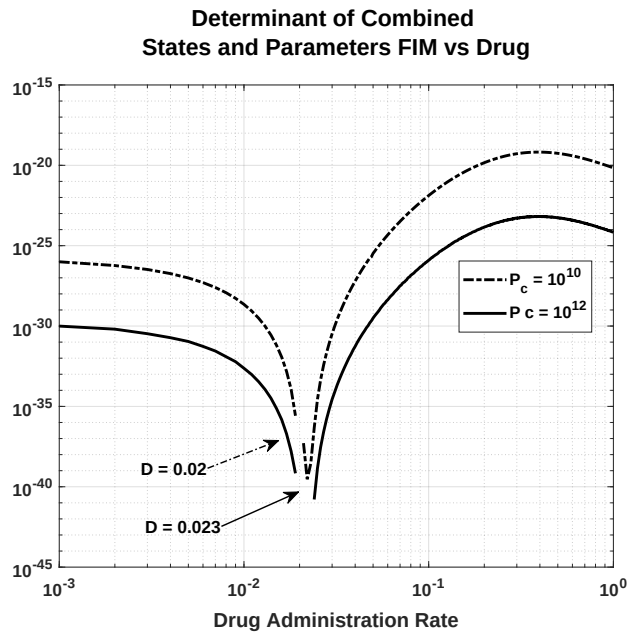

Figure 3.4: Combined states and parameters Fisher Information Matrix Determinant for two parameters and two initial states together.

sizes of sensitive and resistant cells, $S(0)$ and $R(0)$, can be estimated. Knowledge of these initial conditions plus the drug administration history, $D(t)$ makes it possible to estimate $S(t)$ and $R(t)$ at other instants in time. This section analyzes the observability of a linearized version of the tumor dynamics model. In doing so, the section summarizes earlier findings by the authors [102] and provides simple, closed-form analytic expressions that shed light on the chapter's broader combined state/parameter identifiability analysis.

Consider the two-compartment model in Eq. (3.3). This is a nonlinear dynamic model that can be simplified if one assumes the carrying capacity P_c to be much larger than the total cancer cell population size P. In this case, the logistic effect becomes negligible. Furthermore, the model becomes bilinear, in the sense that all the terms in its underlying differential equations become linear except for the product term $S(t)D(t)$. Under the additional simplifying assumption of a constant drug administration rate, D,

the model becomes linear and can be rewritten as follows:

$$\begin{aligned}
\dot{x}_1 &= ((1-\epsilon)r_s - \mu_s - \alpha D)x_1, \\
\dot{x}_2 &= \epsilon r_s x_1 + (r_r - \mu_r)x_2, \\
y(t) &= x_1(t) + x_2(t)
\end{aligned} \tag{3.8}$$

where the state variables $x_1(t)$ and $x_2(t)$ denote the drug-sensitive and drug-resistant population sizes, respectively, and the output $y(t)$ denotes the total population size.

The dynamics of the above model can be expressed in terms of the redefined model parameters as follows:

$$\begin{aligned}
\dot{x}_1 &= \lambda_1 x_1 \\
\dot{x}_2 &= \epsilon r_s x_1 + \lambda_2 x_2 \\
y &= x_1 + x_2
\end{aligned} \tag{3.9}$$

The model's system matrix, or $\mathbf{A}$ matrix, is then given by:

$$\mathbf{A} = \begin{bmatrix} \lambda_1 & 0 \\ \epsilon r_s & \lambda_2 \end{bmatrix} \tag{3.10}$$

The above model is a lower-triangular representation of the dynamics of an au-

tonomous system. The term "autonomous", here, refers to the absence of a time-varying input signal. Because the drug administration rate, D, is treated as constant, its impact on the overall system dynamics is absorbed into the above $\mathbf{A}$ matrix. The roles of the system's three redefined parameters are now clear: λ_1 and λ_2 serve as eigenvalues affecting the system's dynamics, and ϵr_s governs the mutation of drug-sensitive cells into drug-resistant cells.

To analyze the above model's observability, we determine the output matrix $\mathbf{C}$ and observability test matrix $\mathbf{Q}$ as follows:

$$\mathbf{C} = \begin{bmatrix} 1 & 1 \end{bmatrix} \tag{3.11}$$

$$\mathbf{Q} = \begin{bmatrix} \mathbf{C} \\ \mathbf{CA} \end{bmatrix} = \begin{bmatrix} 1 & 1 \\ \lambda_1 + \epsilon r_s & \lambda_2 \end{bmatrix} \tag{3.12}$$

In order for the above model to be observable, the rank of the matrix $\mathbf{Q}$, must equal 2, the number of state variables. This leads to the following condition for loss of observability:

$$\begin{aligned} \lambda_1 + \epsilon r_s &= \lambda_2 \Rightarrow Loss\, of\, Observability \\ \Rightarrow \alpha D &= r_s - \mu_s - r_r + \mu_r \end{aligned} \tag{3.13}$$

When the above condition is met, it is impossible to estimate the drug-sensitive and drug-resistant cell population sizes simultaneously. This occurs at a specific drug admin-

istration rate. To analyze this undesirable condition further, we examine the following arguments. First, the term ϵr_s governs the degree to which the mutation of drug-sensitive cells contributes to the drug-resistant population. It is, therefore, reasonable to treat this term as a positive constant. Second, it is reasonable to assume that the cell mutation rate is quite small compared to the net growth rates of both the drug-sensitive and drug-resistant cells. This assumption implies that ϵr_s is likely to be much smaller in magnitude than λ_1 or λ_2. Together, these arguments/assumptions imply that the loss of observability coincides with $\lambda_1 \approx \lambda_2$. In other words, when the net growth rates of the sensitive and resistant cells are approximately equal, one can no longer estimate the sizes of these two populations simultaneously. This condition coincides with the loss of diagonalizability of the system's $\mathbf{A}$ matrix, as indicated below:

$$\begin{aligned} \lambda_1 &= \lambda_2 \Rightarrow Loss\, of\, Diagonalizability \\ \alpha D &= (1-\epsilon)r_s - \mu_s - r_r + \mu_r \end{aligned} \tag{3.14}$$

3.6 State Observability for Nonlinear Tumor Dynamics

Fisher identifiability analysis provides a pathway for generalizing the above state observability results to the nonlinear tumor model. To perform Fisher analysis, recall the sensitivity definitions in Eq. (3.5). Assuming the model's parameters to be known, only the sensitivities of the output with respect to $S(0)$ and $R(0)$ are needed in this section, given its focus on initial state estimation. To perform Fisher analysis for the two ini-

tial states, define a sensitivity vector $\mathbf{s}(t)$, such that $\mathbf{s}(k\delta t) = [s_1(k\delta t), s_2(k\delta t)]^T$ (where the definitions of s_1 and s_2 are given in Eq.(3.5)). Then the corresponding 2x2 Fisher information matrix is given by:

$$\mathbf{F} = \frac{1}{\sigma^2} \sum_{k=1}^{N} \mathbf{s}(k\delta t)\mathbf{s}^T(k\delta t), \tag{3.15}$$

One convenient mathematical simplification is to approximate the expression for the Fisher information matrix using integration, as opposed to summation, with respect to time. Specifically, as the sampling time δt approaches zero, the Fisher information matrix approaches the approximation below.

$$\mathbf{F} \approx \frac{1}{\sigma^2 \delta t} \int_0^{N\delta t} \mathbf{s}(\tau)\mathbf{s}(\tau)^T d\tau \tag{3.16}$$

Fisher analysis can be used for assessing state observability, parameter identifiability, or combined state/parameter identifiability. To use it for analyzing state observability, consider the nonlinear tumor dynamics model presented in Eq. (3.3). Let the vector of parameters to be estimated consist of the initial sizes, $S(0)$ and $R(0)$, of the drug-sensitive and drug-resistant cell populations, respectively. Let the true/nominal values of these two parameters be S_o and R_o, respectively. Moreover, denote the time-dependent populations corresponding to these nominal initial conditions by $S_{ref}(t)$ and $R_{ref}(t)$, respectively. Now consider a situation where the initial drug-sensitive population is perturbed slightly by some $\delta S(0)$, i.e., $S(0) = S_o + \delta S(0)$. Let the resulting perturbed drug-sensitive and drug-resistant cell populations be $S(t) + \delta S(t)$ and $R(t) + \delta R(t)$, respectively. Then the

true rate of change of the drug-sensitive cell population is given by:

$$\dot{S}(t) = \dot{S}_{ref}(t) + \delta\dot{S}(t) \tag{3.17}$$

Combining Eq. (3.3) and Eq. (3.17) then gives:

$$\begin{aligned}
\dot{S}(t) &= \lambda_1(S_{ref}(t) + \delta S(t)) \\
&\quad -(\frac{1}{P_c})(\lambda_1 + \alpha D)(S_{ref}(t) + \delta S(t))^2 \\
&\quad -(\frac{1}{P_c})(\lambda_1 + \alpha D)(S_{ref}(t) + \delta S(t))(R_{ref}(t) + \delta R(t))
\end{aligned} \tag{3.18}$$

Also, since S_{ref} and similarly R_{ref} are nominal solutions for the $\dot{S}$ and $\dot{R}$ equations, the following equation is obtained:

$$\begin{aligned}
\dot{S}_{ref}(t) &= \lambda_1 S_{ref}(t) - (\frac{1}{P_c})(\lambda_1 + \alpha D)S_{ref}(t)^2 \\
&\quad -(\frac{1}{P_c})(\lambda_1 + \alpha D)S_{ref}(t)R_{ref}(t)
\end{aligned} \tag{3.19}$$

Subtracting the expression for $\dot{S}_{ref}$ from the expression for $\dot{S}$ and neglecting higher-order terms gives the following differential sensitivity equation:

$$
\begin{aligned}
\delta\dot{S}(t) \quad &\approx [\lambda_1 - (\frac{2}{P_c})(\lambda_1 + \alpha D)S_{ref}(t) \\
&-(\frac{1}{P_c})(\lambda_1 + \alpha D)R_{ref}(t)]\delta S(t) \\
&+[-(\frac{1}{P_c})(\lambda_1 + \alpha D)S_{ref}(t)]\delta R(t)
\end{aligned} \tag{3.20}
$$

Repeating the same procedure for $\delta\dot{R}$ gives the following:

$$
\begin{aligned}
\delta\dot{R}(t) \quad &\approx [\varepsilon r_s - (\tfrac{1}{P_c})(\lambda_2 + \varepsilon r_s)R_{ref}(t) \\
&-(\tfrac{1}{P_c})(2\varepsilon r_s)S_{ref}(t)]\delta S(t) \\
&+[\lambda_2 - (\tfrac{1}{P_c})(\lambda_2 + \varepsilon r_s)S_{ref}(t) \\
&-(\tfrac{1}{P_c})(2\lambda_2)R_{ref}(t)]\delta R(t)
\end{aligned} \tag{3.21}
$$

The sensitivity of the output with respect to a perturbation in the initial sensitive cell population, $s_1(t)$, is obtained by solving the above two equations for a nonzero initial $\delta S(0)$ plus a zero initial perturbation $\delta R(0)$. Summing the resulting $\delta S(t)$ and $\delta R(t)$ then furnishes the desired sensitivity. Stated mathematically:

$$
s_1(t) = \frac{[\delta S(t) + \delta R(t)]_{\delta S(0)\neq 0, \delta R(0)=0}}{\delta S(0)} \tag{3.22}
$$

Similarly, the sensitivity of the output to a perturbation in the initial resistant cell

population is given by:

$$s_2(t) = \frac{[\delta S(t) + \delta R(t)]_{\delta S(0)=0, \delta R(0)\neq 0}}{\delta R(0)} \tag{3.23}$$

Together, these two sensitivities constitute the vector of sensitivities $\mathbf{s}(t)$ needed for computing the Fisher information matrix. The diagonal terms of the inverse of this matrix represent the variances with which the best possible unbiased parameter estimator can determine the initial values of the drug-sensitive and drug-resistant cell populations. Please note that the governing equations for $\delta S(t)$ and $\delta R(t)$, namely, Eqs. (3.20,3.21), are linear and time-varying. As a result, their solutions scale linearly with $\delta S(0)$ and $\delta R(0)$. The implication is that the solutions of Eqs. (3.22,3.23) do not change with the choice of $\delta S(0)$ and $\delta R(0)$.

Fig. (3.5) performs the above Fisher information analysis for the nonlinear cancer dynamics model for two different carrying capacities. The vertical axes in the subplots are the variances of the cell population estimation errors, normalized with respect to the true initial population values. The worst-case estimation errors are obtained at a drug administration rate almost identical to the rate at which the linearized cancer model loses observability. Moreover, as seen in the subplots, changing the cell mutation rate has almost no effect on this worst-case scenario. In summary, the results of this Fisher analysis are consistent with the earlier findings using the approximate linearized model.

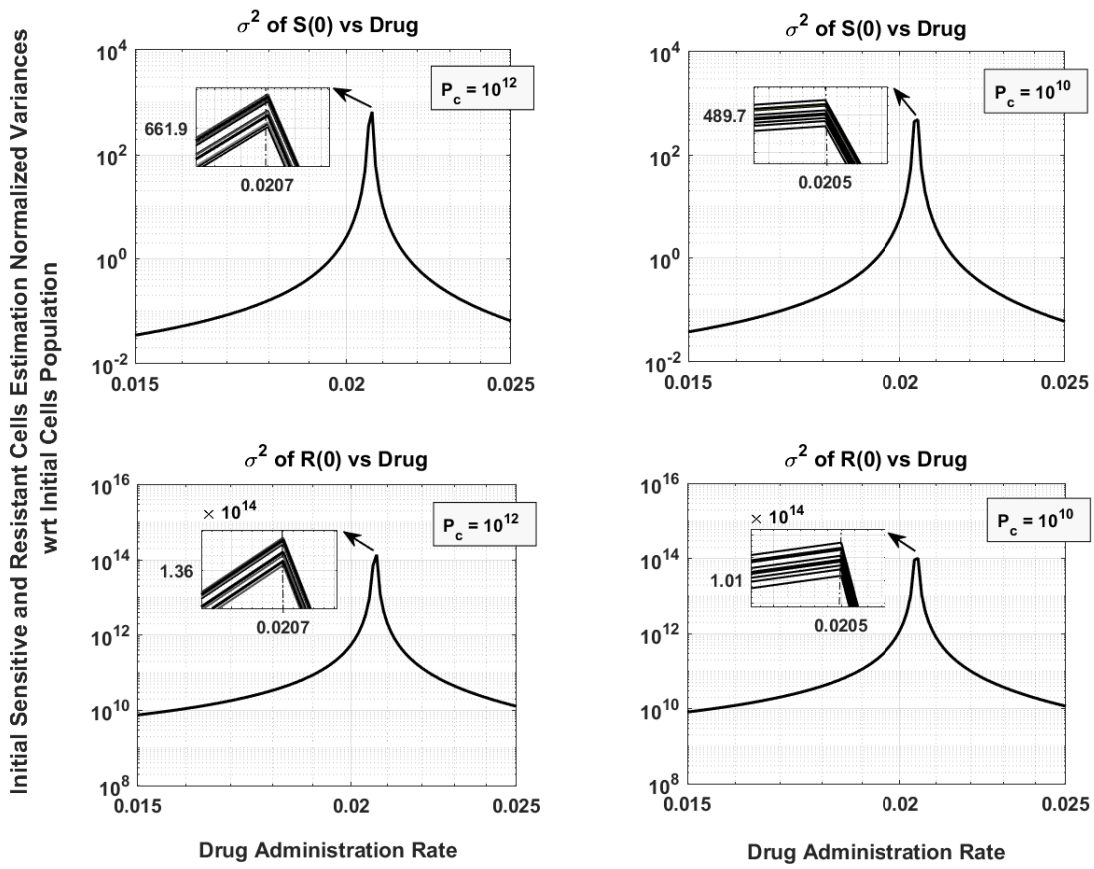

Figure 3.5: Normalized nonlinear drug-sensitive and drug-resistant initial population size observabilities. The mutation rate (ϵ) is changing from 0 to 10^{-6} in 10 increments.

3.7 Parameter identifiability analysis

The chapter's next goal is to analyze parameter identifiability for the linear cancer dynamics model and compare the results with a practical parameter identifiability study for the nonlinear model. Towards this goal, the work in this chapter uses Eq. (3.9) to examine how parameter perturbations affects the model's output measurements. In order to derive sensitivity equations, the two states equations are solved assuming given initial populations $x_{1,0}$ and $x_{2,0}$ as follows:

$$
\begin{aligned}
x_1(t) &= x_{1,0}e^{\lambda_1 t} \\
x_2(t &= \epsilon r_s x_{1,0} \int_0^t e^{\lambda_1 \tau} e^{\lambda_2 (t-\tau)} d\tau + x_{2,0} e^{\lambda_2 t} \\
&= \epsilon r_s x_{1,0} e^{\lambda_2 t} \int_0^t e^{(\lambda_1 - \lambda_2)\tau} d\tau + x_{2,0} e^{\lambda_2 t} \\
&= \epsilon r_s x_{1,0} e^{\lambda_2 t} \frac{1}{\lambda_1 - \lambda_2} [e^{(\lambda_1 - \lambda_2)t} - 1] + x_{2,0} e^{\lambda_2 t} \\
y_(t) &= x_1(t) + x_2(t) \qquad (3.24)
\end{aligned}
$$

In the above equation, $x_1(t)$ and $x_2(t)$ are the analytic solutions of the linearized cancer dynamics model. These solutions are expressed in terms of the initial pathogen population sizes as well as the constant model parameters, λ_1 and λ_2. To perform parameter identifiability analysis on this model, we begin by perturbing these two parameters and analyzing the sensitivity of the above analytic model solution to these perturbations. Specifically, we perturb the parameter λ_1 in a manner conducive to performing a normalized Fisher analysis, by setting its perturbed value to $\lambda_1(1 + \epsilon_1)$. Similarly, we replace λ_2 by $\lambda_2(1 + \epsilon_2)$. The use of normalization upfront within Fisher analysis furnishes normalized parameter error bounds. This is convenient for the purpose of performing apples-to-apples comparisons of parameter estimation errors. Moreover, the main conclusion of this section is easier to observe mathematically through this normalization. Applying the λ_1 perturbation to the linearized tumor dynamics model furnishes the following sensitivity function:

$$
\begin{aligned}
x_1(t)|_{pert.(\lambda_1)} &= x_{1,0}e^{\lambda_1(1+\varepsilon_1)t} \\
x_2(t)|_{pert.(\lambda_1)} &= \epsilon r_s x_{1,0}e^{\lambda_2 t}\frac{1}{\lambda_1(1+\varepsilon_1)-\lambda_2} \\
&\quad \times[e^{(\lambda_1(1+\varepsilon_1)-\lambda_2)t}-1]+x_{2,0}e^{\lambda_2 t} \\
y_(t)|_{pert.(\lambda_1)} &= x_1(t)|_{pert.(\lambda_1)}+x_2(t)|_{pert.(\lambda_1)} \\
s_{l,1}(t) &= \frac{y_(t)|_{pert.(\lambda_1)}-y(t)|_{nominal}}{\varepsilon_1}
\end{aligned} \tag{3.25}
$$

A similar perturbation analysis can be used to solve for sensitivity of the output with respect to perturbations in λ_2, producing the equations below:

$$
\begin{aligned}
x_1(t)|_{pert.(\lambda_2)} &= x_{1,0}e^{\lambda_1 t} \\
x_2(t)|_{pert.(\lambda_2)} &= \epsilon r_s x_{1,0}e^{\lambda_2(1+\varepsilon_2)t}\frac{1}{\lambda_1-\lambda_2(1+\varepsilon_2)} \\
&\quad \times[e^{(\lambda_1-\lambda_2(1+\varepsilon_2))t}-1]+x_{2,0}e^{\lambda_2(1+\varepsilon_2)t} \\
y_(t)|_{pert.(\lambda_2)} &= x_1(t)|_{pert.(\lambda_2)}+x_2(t)|_{pert.(\lambda_2)} \\
s_{l,2}(t)|_{pert.(\lambda_2)} &= \frac{y_(t)|_{pert.(\lambda_2)}-y(t)|_{nominal}}{\varepsilon_2}
\end{aligned} \tag{3.26}
$$

The above two sensitivity functions, $s_{l,1}(t)$ and $s_{l,2}(t)$, are conceptually analogous to the sensitivity functions $s_1(t)$ and $s_2(t)$ in Eq. (3.5), with two important caveats. First, the above derivation assumes a linearized tumor dynamics model, whereas Eq. (3.5) applies to the full nonlinear tumor dynamics model. Second, the fact that the denominators

in these sensitivity equations are non-dimensional (e.g., ϵ_1 instead of $\epsilon_1\lambda_1$) means that the resulting Fisher information analysis will automatically furnish normalized estimation variances. In other words, one will not need to divide the parameter estimation variances by the corresponding nominal parameter values squared in order to obtain normalized results.

Given the sensitivity expressions in Eqs. (3.25,3.26), one can use Fisher information analysis to analyze the identifiability of the linear model's parameters, as shown below. The Fisher information matrix corresponding to the parameters λ_1 and λ_2 is as follows:

$$\mathbf{F} \cong \frac{1}{\sigma^2 \delta t} \begin{bmatrix} \int_0^{N\delta t} s_{l,1}(t)^2 d\tau & \int_0^{N\delta t} s_{l,1}(t) s_{l,2}(t) d\tau \\ \int_0^{N\delta t} s_{l,2}(t) s_{l,1}(t) d\tau & \int_0^{N\delta t} s_{l,2}(t)^2 d\tau \end{bmatrix} \tag{3.27}$$

Inverting the above Fisher matrix furnishes the best-achievable estimation covariance matrix for the parameters λ_1 and λ_2, normalized with respect to the nominal values of these parameters. The diagonal terms in this matrix represent the best-achievable normalized variances for λ_1 and λ_2.

Fig. (3.6) plots the above normalized estimation variances versus different values of the drug administration rate, D for two different carrying capacities. The solid lines in all figures represent the normalized parameter estimation variances for the linearized drug administration model, which neglects the logistic effect. The dashed lines in all the figures represent the normalized parameter estimation variances computed numerically

for the nonlinear tumor dynamics model, accounting for the logistic effect. As shown in the Fig. (3.6), the two different carrying capacities are assumed to be $P_c = 10^{12}$ and $P_c = 10^{10}$, 100 times smaller. The intent is to gain insight into the degree to which the value of the carrying capacity affects the applicability of the linear model identifiability analysis to the nonlinear case. Normalization is performed with respect to the nominal parameter values in the figures.

Three important conclusions are visible from these figures and results. First, the identifiability of the parameters of the tumor dynamics model is quite poor, even when

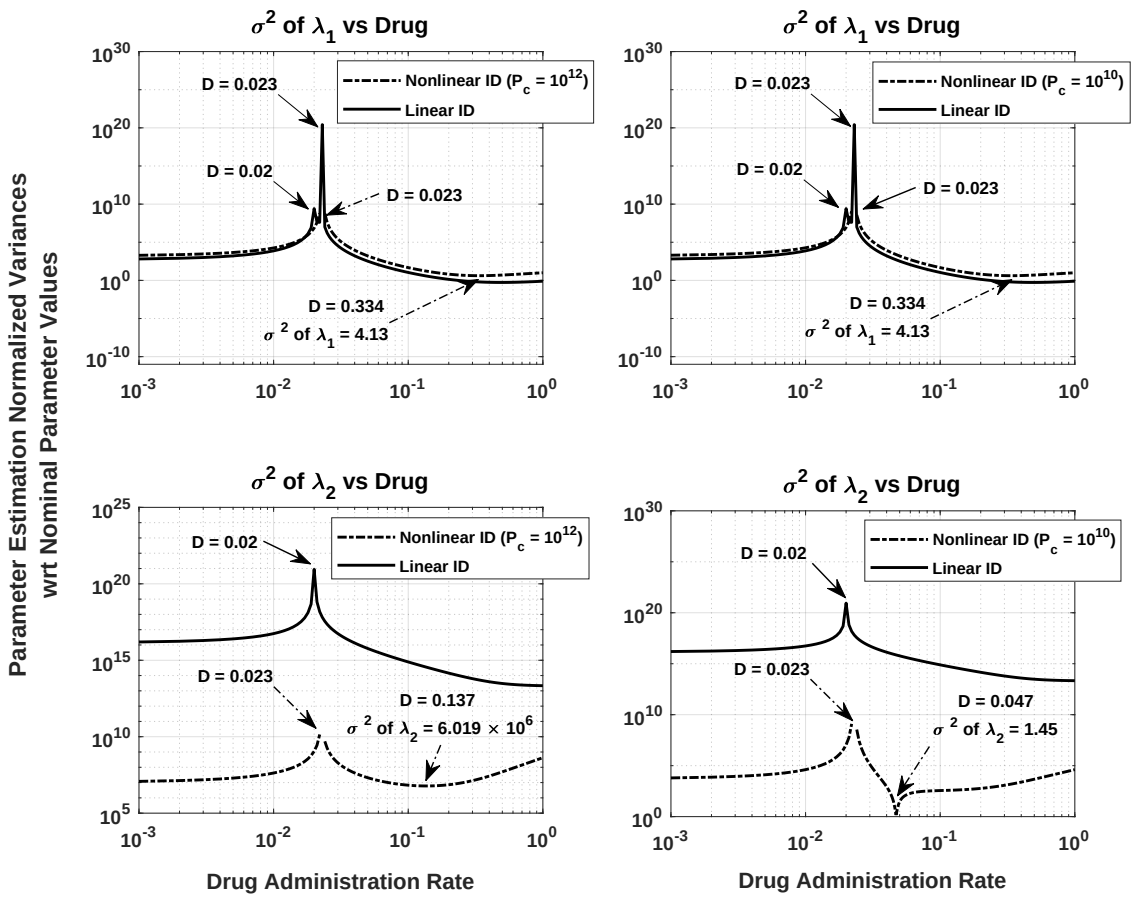

Figure 3.6: Comparing uncertainty of both drug-sensitive and drug resistant cells net growth rate estimation for two different nominal carrying capacities of $P_c = 10^{12}$ and $P_c = 10^{10}$ cells.

the drug-sensitive and drug-resistant cell populations are assumed to be directly measurable. For example, when the tumor has a carrying capacity of 10^{12} cells, the best achievable normalized estimation error squared for λ_1 is 4.13 which corresponds to $D = 0.334$, meaning that the error in estimating λ_1 is almost 2 times the nominal value of λ_1. Moreover, a drug administration rate of $D = 0.137$ minimizes the estimation variance of λ_2 down to 6.019×10^6, meaning that one cannot estimate the drug resistance net growth rate better than 2453 times its nominal value. This highlights the difficulty of estimating the parameters of drug resistance in a cancer dynamics model solely from total tumor size measurements. Second, the linear and nonlinear identifiability analyses produce consistent results when the tumor carrying capacity is large. When the tumor carrying capacity is reduced, the primary difference between these two analyses is a reduction in the best-achievable normalized estimation variance for λ_2. Even with this reduction, the identifiability of the model's parameters remains poor. Third, as with combined state/parameter identifiability, we see two peak scenarios where parameter identifiability is particularly poor. One of these two peaks corresponds to the loss of observability of the cancer dynamics, as explained earlier in this research. The second peak corresponds to a drug administration rate of $D = 0.023$. The remainder of this section provides insight into the significance of this peak by continuing the above linear model parameter identifiability analysis.

One benefit of using a linearized model of tumor dynamics to analyze Fisher parameter identifiabiltiy is the fact that it makes it possible to compute the resulting Fisher information matrix analytically. Specifically, the sensitivies in Eq. (3.25,3.26) can be computed analytically. Moreover, one can use this analytic computation to derive an

expression for the Fisher information matrix in Eq. (3.27), under the assumption that $\lambda_1 = 0$. The significance of assuming that $\lambda_1 = 0$ in the analysis below is twofold. First, as the analysis will show, the specific scenario where $\lambda_1 = 0$ coincides with one of the two worst-case conditions for poor parameter identifiability. Second, setting $\lambda_1 = 0$ furnishes a treatment protocol where the goal is to maintain a constant sensitive cell population size. Such a protocol is conceptually close to the "containment" protocols examined in earlier literature, and therefore sheds light on the potential impact of tumor containment on identifiability. Performing this analysis produces the results below:

$$
\begin{aligned}
y(t) &= x_{1,0}\, e^{\lambda_1 t} + x_{2,0}\, e^{\lambda_2 t} + \epsilon r_s\, x_{1,0} \int_0^t e^{\lambda_1 t} e^{\lambda_2 (t-\tau)} d\tau \\
\lambda_1 &= \lambda_{1,0}(1+\varepsilon_1) \\
s_1(t) &= \frac{\partial y}{\partial \varepsilon_1} \\
\frac{\partial y}{\partial \varepsilon_1} &= \lambda_{1,0} t\, x_{1,0}\, e^{\lambda_{1,0}(1+\varepsilon_1)t} \\
&\quad + \epsilon r_s\, x_{1,0} \int_0^t \lambda_{1,0} t\, e^{\lambda_{1,0}(1+\varepsilon_1)t} e^{\lambda_2 (t-\tau)} d\tau \\
&= \lambda_{1,0} t\, (y - x_{2,0}\, e^{\lambda_2 t}) \\
&\quad if\ \lambda_{1,0} = 0 \ \Rightarrow s_1(t) = 0 \\
&\quad \Rightarrow \mathbf{F} \cong \frac{1}{\sigma^2 \delta t} \int_0^{N\delta t} \begin{bmatrix} 0 & 0 \\ 0 & s_2(t)^2 d\tau \end{bmatrix}
\end{aligned}
\tag{3.28}
$$

The above Fisher information matrix is singular, and therefore not invertible. This singularity implies the loss of parameter identifiability. The singularity occurs when $\lambda_1 = 0$, which occurs when $D = 0.023$. Therefore, we arrive at the important insight that when

the drug administration rate is tailored such that the net growth rate of the drug-sensitive pathogen cell population equals zero, parameter identifiability is lost. This conclusion can be seen using an analytic derivation for the parameter identifiability of the linearized tumor dynamics model. Moreover, it is consistent with the practical identifiability results for the nonlinear tumor dynamics model. The practical implication of this conclusion is that drug administration rates that are conducive to sensitive population containment make it especially difficult to estimate the parameters of the underlying tumor dynamics model.

One important caveat in the field of identifiability analysis is the fact that the larger the set of quantities one seeks to estimate, the less accurately one can estimate these quantities, and *vice versa*. Table (3.4) illustrates this insight by listing the normalized estimation variances of the nonlinear tumor dynamics model's initial conditions and constant parameters for two different drug administration rates. The rows of the table for each one of the drug administration rates show: (i) the parameter estimation variances one obtains if the model's initial conditions are known; (ii) the state estimation variances if the model's parameters are known; and (iii) the combined state/parameter estimation variances one obtains through combined state/parameter identifiability analysis. A visible worsening is seen in both state and parameter estimation accuracy when one analyzes combined state/parameter identifiability. This illustrates the important point that the availability of more accurate means of measuring the prevalence of drug resistance in a cancerous tumor (i.e., the sizes of the drug-sensitive and drug-resistant populations) can be valuable for quantifying the uncertainties in that tumor's underlying dynamics.

Table 3.4: Normalized CRLBs two drug administration rates of D = 0.015 and D = 0.035.

D	Identifiability of:	λ_1	λ_2	S(0)	R(0)
D = 0.015	Parameters	1.3×10^5	1.26×10^8	-	-
	States	-	-	0.034	7.5×10^9
	Combined	1.4×10^{10}	2.5×10^{12}	5.46×10^6	1.12×10^{18}
D = 0.035	Parameters	3.4×10^4	7.6×10^7	-	-
	States	-	-	0.0066	1.1×10^9
	Combined	5.3×10^8	3.5×10^{11}	3.5×10^4	7.3×10^{15}

3.8 Conclusion

This chapter examines the problem of estimating the initial conditions and parameters of a model of drug-resistance cancerous dynamics. The chapter analyzes this model's combined state/parameter identifiability using Fisher information analysis. This analysis is performed numerically for a nonlinear model of the tumor's dynamics. To gain further insights into the results of this analysis, the chapter then linearizes the tumor dynamics model, and uses the linearized model to analyze state observability and parameter identifiability independently. The results of these simplified analyses are shown to hold for the original model, especially for tumors with large carrying capacities. One conclusion from this analysis is that it is extremely difficult to obtain accurate estimates of the tumor dynamics model's initial conditions and parameters, especially if the mutation rate of the drug-sensitive pathogen cell population is unknown. Another conclusion is that two scenarios exist where combined state/parameter identifiability is particularly poor. The first scenario occurs when the rate of drug administration causes the net growth rates of the drug-sensitive and drug-resistant pathogen cell populations to be approximately equal, leading to the loss of observability. The second scenario occurs when the rate of drug

administration causes the net growth rate of the drug-sensitive cell population to equal zero.

From a high-level perspective, the fundamental message of this chapter is that poor input shaping can jeopardize the identifiability of multi-compartment dynamic system model parameters. The next chapter explores the opposite side of this fundamental coin by showing the degree to which optimal input shaping can potentially improve multi-compartment dynamic system model identifiability.

Chapter 4: Periodic Optimal Input Shaping for Maximizing Lithium-Sulfur Battery Parameter Identifiability

4.1 Overview

This chapter investigates the problem of optimal periodic cycling for maximizing the identifiability of the unknown states and parameters of a Lithium-Sulfur (Li-S) battery model. This research is motivated by the need for more accurate Li-S battery modeling and diagnostics. Li-S batteries offer higher energy density levels compared to more traditional lithium-ion batteries, making them an attractive option for energy storage applications. However, the monitoring and control of Li-S batteries is challenging because of the complexity of the underlying multi-step reaction chain. The existing literature addresses poor battery parameter identifiability through a variety of tools including optimal input shaping for Fisher information maximization. However, this literature's focus is predominantly on the identifiability of lithium-sulfur battery model parameters. The main purpose of this study is to optimize Li-S battery Fisher identifiability through optimal input shaping. The study shows that such optimal input shaping has the potential to improve the accuracy of Li-S battery state and parameter estimation significantly.

Broadly speaking, the problems examined in Chapters 3 and 4 of this dissertation

can be seen as two sides of the same coin. On the one hand, Chapter 3 illustrates the fact that poor input shaping has the potential to lead to poor dynamic system parameter identifiability. On the other hand, this chapter illustrates the degree to which optimal input shaping has the potential to improve multi-compartment dynamic system parameter identifiability. The compartments in a Li-S battery model represent the various species involved in the battery discharge reaction chain. Moreover, the identifiability optimization problem for Li-S batteries is complicated by the multiplicity of species involved in this reaction chain. [1]

4.2 Introduction

This chapter present a simulation-based study that demonstrates how the input current trajectory can be optimized to maximize the parameter identifiability of a physics-based zero-dimensional electrochemical model of a lithium-sulfur (Li-S) battery. This research uses Fisher information as the metric for quantifying parameter identifiability. Li-S batteries are attractive due to their potential to achieve very high specific energy levels (2600 watts/kg) and specific charge capacities (1672Ah/kg). [104]. Prototype Li-S cells have achieved specific energies well over 700 Watts/kg [105]. Li-S technology, however, suffers from limitations such as complex reaction kinetics and high self-discharge rates [106, 107, 108]. The literature presents several efforts focusing on improving Li-S battery performance through electrodes, separator and electrolyte design [109, 110, 111, 112]. Building on this existing research, this chapter focuses on improving battery performance by maximizing the identifiability of Li-S battery model parameters,

[1] The work in this chapter is currently in preparation for potential archival publication.

with the goal of ultimately enabling optimal model-based diagnosis and control.

Maximizing the identifiability of the lithium-ion batteries' states and parameters through optimal input shaping is a well-established topic of inquiry in the literature [12, 14, 15, 18, 113, 114]. However, the challenge of applying this topic of inquiry to the Li-S chemistry remains relatively unexplored. This open gap in the literature can be attributed at least in part to the complexity of the electrochemical models for Li-S batteries. The discharge of a lithium-sulfur battery involves multiple electrochemical reduction reactions and intermediate reaction products/species, unlike the discharge of a typical lithium-ion battery, where only one major reduction/oxidation step takes place. This complicates Li-S battery management, diagnostics, and (in the context of this work) identifiability optimization.

The Li-S battery model used in this research is a zero-dimensional (0D) electrochemical model, meaning that it captures the multiplicity of underlying oxidation-reduction reactions but neglects the spatial diffusion of ions within the battery in favor of the simplifying assumption that all ion distributions are spatially uniform within each battery electrode. This model builds on an extensive existing Li-S battery modeling literature that examines equivalent circuit models [115, 116, 117, 118] and more complex models of the underlying coupled diffusion-reaction dynamics [119, 120, 121, 122, 123, 124]. The equivalent circuit models presented in this literature are typically used for online state of charge estimation, given their appealing computational tractability [125, 126, 127]. In contrast, the literature's coupled diffusion-reaction models, usually expressed in terms of systems of partial differential algebraic equations (PDAEs), are typically more accurate but computationally prohibitive for applications such as identifiability optimization. The

zero-dimensional model used in this study represents a middle ground between these two extremes, in the sense that it captures key underlying battery physics while remaining computationally tractable [128, 129].

The literature already presents multiple Li-S battery state and parameter estimation methods and studies [125, 126, 127, 130, 131, 132]. This includes previous work by one of the author's collaborators on Li-S battery model parameterization and sensitivity analysis [133, 134]. The intent of this article is to extend the above work significantly by using identifiability optimization to maximize the accuracy with which one can potentially estimate the state and parameters of Li-S batteries. *Identifiability* is a well-established concept in control theory, with important mathematical connections to other key concepts in control theory such as observability and controllability [19, 20]. To say that a battery model has good identifiability is to assert that it is possible to estimate the model's states and parameters uniquely and accurately from input-output cycling data. Moreover, to achieve such good identifiability, one often needs to optimize the underlying battery test protocol.

Different approaches exist in the literature for testing electrochemical batteries, including both destructive and non-destructive testing approaches. Non-destructive battery tests include both thermal and electrical cycling tests. The focus of this chapter is specifically on optimizing a periodic electric cycling test for an Li-S battery cell. Simple electric battery cycling tests include both galvanostatic (i.e. constant current) and potentiostatic (i.e., constant voltage) tests. The family of test protocols examined in this chapter goes further than either the galvanostatic or potentiostatic testing approaches. Specifically, the chapter considers a scenario where an Li-S battery cell is attached to a flexible cycler at

room temperature. Suppose the cycler is able to dictate a time-varying charge/discharge current as an input to the battery. Moreover, supposed that this current is periodic, leading to a repeatable or periodic test cycle/protocol. Finally, suppose that one is able to measure the terminal voltage of the battery cell while it is being cycled. The main question addressed in this chapter is: *what is the optimal shape of the input current applied to this battery cell, if the goal is to estimate its underlying parameters uniquely and accurately from the resulting cycling data?*

The remainder of this chapter is organized as follows. Section (4.3) presents the 0D physics-based Li-S battery model used in this study. The chapter then proceeds to two bodies of work. First, section (4.4) summarizes the steps needed for applying identifiability analysis to Li-S batteries. Specifically, the application of tools such as sensitivity-based Fisher information analysis to Li-S battery cell models is discussed. Second, section (4.5) uses numerical optimization to design a battery input current trajectory that maximizes the Fisher identifiability of Li-S battery states and parameters. Finally, Section (4.6) summarizes the chapter's findings and conclusions.

4.3 Li-S Battery Model

This section describes the zero-dimensional physics-based Li-S battery model used throughout this chapter, building on earlier modeling efforts in the literature [128, 129]. This model serves as a foundation for subsequent identifiability analysis and optimal input shaping. Similar to lithium-ion batteries, Li-S battery cells consist of a separator sandwiched between two electrically conductive, porous positive and negative electrodes. The

components are soaked in electrolyte to allow for the transport of Lithium ions between both electrodes. However, the voltage performance characteristics of Li-S batteries are fundamentally different from Lithium-ion cells. Figure (4.1) shows a typical Li-S battery discharge voltage curve. The curve exhibit a high plateau region and a low plateau region, separated by a "dipping point" where the precipitation of the final reduction reaction product is triggered. During Li-S battery operation, cathode-side sulfur reacts with lithium to form different sulfide species, including $S_8^{2-}, S_6^{2-}, S_4^{2-}, S_2^{2-}$, and finally S^{2-} [135]. At the same time, lithium is oxidized to furnish lithium ions in the negative electrode.

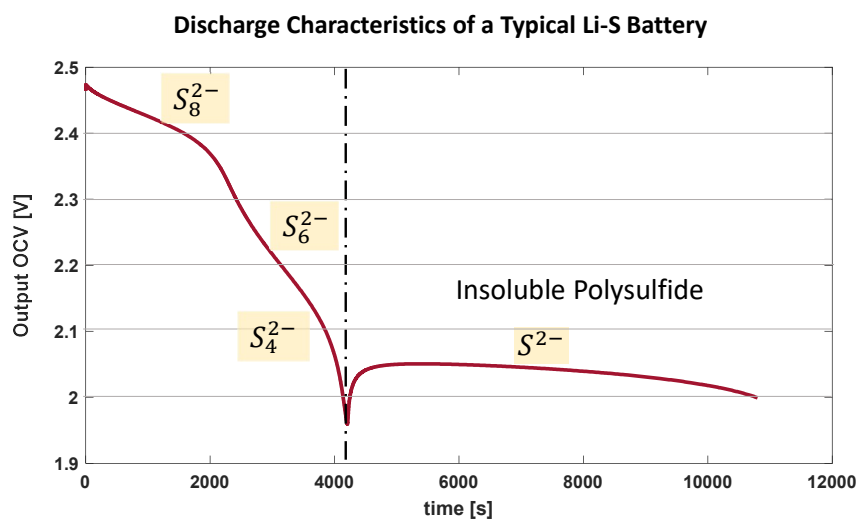

Figure 4.1: Li-S battery voltage curve during discharge

Table (4.1) shows five dissolved sulfur species ($S_8, S_8^{2-}, S_6^{2-}, S_4^{2-}$ and S^{2-}) in four reduction reactions in Li-S batteries. These reactions form the 0D model assuming that there exists no mass transport due to the dissolved species diffusion/migration. Only the electrochemical reaction and precipitation change the masses of the dissolved and precipitated sulfur.

The zero-dimensional model is presented in Figure (4.3). The model shows the state

variables, state equations (Eq. (4.1-4.3)) and algebraic constraints (Eq. (4.4-4.7)) for Li-S batteries [133, 136]. The state equations in this model governs the rate of change of the masses for five different dissolved sulfur species and for the precipitated sulfur, plus the rate of change of cathode material porosity. These dynamics form the state space model for Li-S batteries. The model's input is discharge current I, and the model's output is the voltage measurement across the battery V. The Nerst equation for reduction potentials and the Butler-Volmer equation for reaction kinetics are the physics-based algebraic constraints in this model. Fig. (4.2) shows a simple schematic of the Li-S battery's governing dynamics and constraints from an input-output perspective.

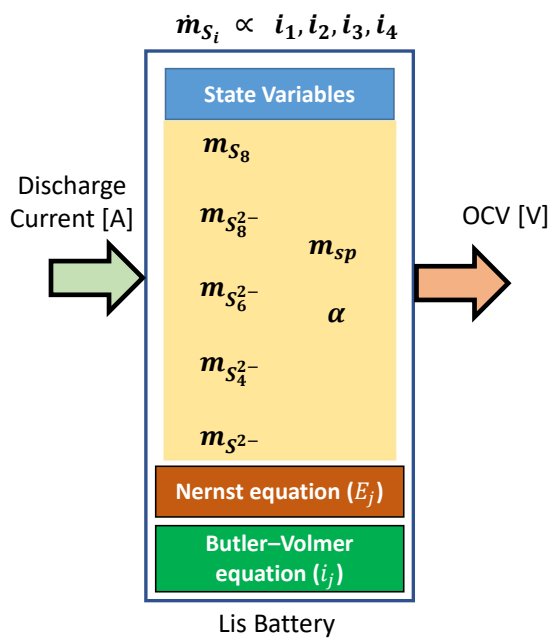

Figure 4.2: Schematic of an Li-S battery cell during discharge

The above model is based on three main assumptions. First, the only redox reactions that take place in the Li-S battery are the ones listed in Table (4.1). Second, the only sulfide species that participates out of solution is Li_2S. Third, The model does not

Table 4.1: Reduction reactions considered in the 0D model

Reduction Reactions # j	$\#1: \frac{1}{2}S_8 + e^- \rightleftharpoons \frac{1}{2}S_8^{2-}$ $\#2: \frac{3}{2}S_8^{2-} + e^- \rightleftharpoons 2S_6^{2-}$ $\#3: S_6^{2-} + e^- \rightleftharpoons \frac{3}{2}S_4^{2-}$ $\#4: \frac{1}{6}S_4^{2-} + e^- \rightleftharpoons \frac{2}{3}S^{2-}$
Dissolved Sulfur Species # i	$S_8,\ S_8^{2-}, S_6^{2-}, S_4^{2-}, S^{2-}$

Input variable: current I

Output variable: cell voltage V

State Variables	Mass of dissolved sulfur species (m_i)	**State Equations** $\dot{m}_i = \begin{cases} \sum_j \frac{n_{si}M_s}{n_jF} s_{i,j}\, i_j & for\ i = 1, \dots, 4 \\ \sum_j \frac{n_{si}M_s}{n_jF} s_{i,j} i_j - \dot{m}_{sp} & for\ i = 5 \end{cases}$	(4.1)
	Mass of precipitated sulfur (m_{sp})	$\dot{m}_{sp} = k_p m_{sp}(m_5 - S_{sat})$	(4.2)
	Cathode material porosity (α)	$\dot{\alpha} = -\omega \dot{m}_{sp}$	(4.3)
Constraints	Nerst equation for reduction potential (E_j)	$E_j = E_j^0 - \frac{RT}{n_jF}\sum_i s_{i,j}\, ln(\frac{m_i}{n_{si}M_s v})$	(4.4)
	Butler–Volmer equation for reaction current (i_j)	$i_j = -a_v^0\, \alpha^\gamma\, i_j^0 \left\{ \prod_i \left(\frac{m_i}{m_i^0}\right)^{p_{i,j}} e^{\left(\frac{F}{2RT}\eta_j\right)} - \prod_i \left(\frac{m_i}{m_i^0}\right)^{q_{i,j}} e^{\left(-\frac{F}{2RT}\eta_j\right)} \right\}$	(4.5)
		$where\ \eta_j = V - E_j$	(4.6)
	Total discharge current (I)	$\sum_j i_j = I$	(4.7)

Figure 4.3: Li-S battery state variables, stat equations and constraints.

consider the polysulfide shuttle effect in the Li-S battery: a relatively slow process that causes the battery to self-discharge and potentially age/degrade. This assumption reflects the author's interest in the identifability of the initial states and paraemeters pertaining

Table 4.2: List of all the parameters and initial values for the Li-S DAE model

Param.	Description	Values	Unit
E_j^0	Standard potential	2.4673, 2.3742, 2.3420, 2.0693	$[V]$
i_j^0	Exchange current density	2.00, 0.02, 0.02, 0.02	$[A/m^2]$
S_{sat}	Saturation mass of S^{2-}	0.0001	$[g]$
k_p	Precipitation rate constant	22	$[1/(g\ s)]$
m_i^0, m_{Sp}^0	Initial mass of species i, Initial mass of sulfur precipitate	3.0377, 0.216, 0.078, 0.0055, 1.84E-07, 5.77E-07	$[g]$
ω	Porosity change rate constant	0.6133	$[1/g]$
γ	Power of the relative porosity	0.4832	–
M_s	Molar mass of a sulfur atom	32	$[g/mol]$
$s_{i,j}$	Stoichiometric coefficients of the reactions	Table II	–
n_{si}	Number of sulfur atoms in species i	8, 8, 6, 4, 1	–
n_j	Number of electrons exchanged in reaction j	1, 1, 1, 1	–
v	Cell volume	0.0114	$[L]$
R	Gas constant	8.3145	$[J/(K\ mol)]$
T	Room temperature	298	$[k]$
F	Faraday's constant	9.649E4	$[C/mol]$
a_v^0	Initial active reaction area	1	$[m^2]$
$p_{i,j}, q_{i,j}$	Number of species / reactions	Table II	–

to the battery's voltage performance as opposed to its health. This list of assumptions is consistent with earlier modeling work in the literature that forms an important foundation for the current research ([120, 128, 129, 134]).

Tables (4.2,4.3) list all the parameters and initial conditions that one needs to estimate for the above Li-S battery model, along with nominal values of these quantities obtained from earlier work by one of the author's collaborators [133].

The model presented so far is a differential algebraic equation (DAE) model. However, the optimization and identifiability study in this work relies on Fisher information theory, which is more established in the literature for ordinary differential equation (ODE) models [12, 14, 19, 20]. Previous work in the literature shows that the DAE model's algebraic loop can be eliminated by analytically solving the reaction current I_j in Eq. (4.7), thereby allowing this DAE model to be reformulated to an ODE model [133]. The result-

Table 4.3: Stoichiometric coefficients of the reactions and corresponding parameters

Param.	**Values**
s_{ij}	$\begin{pmatrix} -1/2 & 0 & 0 & 0 \\ 1/2 & -3/2 & 0 & 0 \\ 0 & 2 & -1 & 0 \\ 0 & 0 & 3/2 & -1/6 \\ 0 & 0 & 0 & 2/3 \end{pmatrix}$
p_{ij}	$= s_{ij}\ (for\ s_{ij} \geq 0)$; otherwise 0
q_{ij}	$= -s_{ij}\ (for\ s_{ij} \leq 0)$; otherwise 0

ing ODE model can then be written in the following standard state-space form:

$$\begin{aligned} \dot{X} &= f(X, I) \\ V &= h(X, I) \end{aligned} \tag{4.8}$$

The state vector for the above model consists of seven state variables:

$$X = [m_1,\ \ldots,\ m_5,\ m_{S_p},\ \alpha]^T \tag{4.9}$$

This model provides a foundation for the sensitivity analysis, identifiability and the subsequent input optimization study presented in the remainder of the chapter.

4.4 Combined State and Parameter Identifiability for Li-S Batteries: An Overview

Consider the problem of estimating the unknown parameters and initial masses of sulfur species in the above Li-S model. Table (4.4) lists all the 19 unknown initial states

and parameters including the initial masses of $S_8,\ S_8^{2-}, S_6^{2-}, S_4^{2-},\ S^{2-}$, the initial mass of precipitated sulfur, the precipitation rate constant, the cathode porosity parameters, the saturation mass of S_{2-}, the cell volume, each reaction's standard potential, and each reaction's exchange current densities. This section analyzes the theoretical Cramér-Rao bounds on the accuracy of estimating these unknown parameters for a given discharge current profile. This analysis makes a number simplifying assumptions, but the underlying methods can be generalized to relax these assumptions. In particular, we assume that: (i) the true dynamics of sulfur species masses and cathode porosity are governed by Eq. (4.8); (ii) this ODE model is known; (iii) its parameters and initial states are known; (iv) the model's output (namely, the cell voltage) is measured at regular time intervals δt; and (v) this measurement is corrupted by zero-mean, independent, identically distributed Gaussian noise with variance σ^2. In light of these assumptions, Fisher information analysis provides a general method for estimating the accuracy with which initial states and parameters can be determined: [137].

To perform Fisher information analysis, we begin by defining an output variable, $Y(t, \boldsymbol{\theta})$, equal to the true open circuit cell voltage, V, at time t, for a given set of values of a combined unknown initial state and parameter vector, $\boldsymbol{\theta}$. Measurements of this output variable are noisy, but the symbol $Y(t, \boldsymbol{\theta})$ refers to the true output, uncorrupted by noise. The vector $\boldsymbol{\theta}$ is, in turn, defined as $\boldsymbol{\theta} = [\theta_1,\ \theta_2,\ \theta_3,\ \ldots,\ \theta_{19}]^T$

Suppose that the above output $Y(t, \boldsymbol{\theta})$, is measured at moments in time separated by a sampling time δt in seconds. Moreover, suppose that the measured output at every sampling instant is equal to the true output plus an independent, identically distributed measurement noise signal with a zero mean and some variance σ^2. For a given set of

Table 4.4: Parameters for identifiability

#	**Param.**	**Description**	**Unit**
1	$m^0_{s_8}$	Initial mass of S_8	$[g]$
2	$m^0_{s_8^{2-}}$	Initial mass of s_8^{2-}	$[g]$
3	$m^0_{s_6^{2-}}$	Initial mass of s_6^{2-}	$[g]$
4	$m^0_{s_4^{2-}}$	Initial mass of s_4^{2-}	$[g]$
5	$m^0_{s^{2-}}$	Initial mass of s^{2-}	$[g]$
6	m^0_{Sp}	Initial mass of Sp	$[g]$
7	ω	Porosity change rate constant	$[1/g]$
8	γ	Power of the relative porosity	$-$
9	kp	Precipitation rate constant	$[1/(gs)]$
10	$Ssat$	Saturation mass of S^{2-}	$[g]$
11	v	Cell volume	$[L]$
12	E^0_1	Standard potential for reaction #1	$[V]$
13	E^0_2	Standard potential for reaction #2	$[V]$
14	E^0_3	Standard potential for reaction #3	$[V]$
15	E^0_4	Standard potential for reaction #4	$[V]$
16	i^0_1	Exchange current density for reaction #1	$[A]$
17	i^0_2	Exchange current density for reaction #2	$[A]$
18	i^0_3	Exchange current density for reaction #3	$[A]$
19	i^0_4	Exchange current density for reaction #4	$[A]$

unknowns, $\boldsymbol{\theta}$ the sensitivity function $s_i(k\delta t)$, can be defined as follows:

$$s_i(k\delta t) = \lim_{\delta\theta_i \to 0} \frac{Y(k\delta t, \theta + \mathbf{e_i}\delta\theta_i) - Y(k\delta t, \theta)}{\delta\theta_i}, \tag{4.10}$$

where $\delta\theta_i$ represents an infinitesimal change in the ith unknown parameter, and the $\mathbf{e}_i$ represents a selector that only perturbs one parameter at a time. Given the above sensitivity function, one can construct the following sensitivity matrix:

$$\mathbf{S} = \begin{bmatrix} s_1(\delta t) & \dots & s_{19}(\delta t) \\ \vdots & \ddots & \vdots \\ s_1(N\delta t) & \dots & s_{19}(N\delta t) \end{bmatrix}, \tag{4.11}$$

where N is the total number of samples over which identifiability analysis is performed. Each column of the sensitivity matrix in Eq. (4.11) represents the sensitivity of the output voltage to small perturbation in the corresponding parameter estimate over the total measurement time. The Fisher information matrix can be constructed from the above sensitivity matrix as follows:

$$\boldsymbol{F} = \frac{1}{\sigma^2}\mathbf{S}^T\mathbf{S} \tag{4.12}$$

The above computation furnishes a 19×19 matrix. We implemented this combined parameter and initial states sensitivity analyses numerically for all the unknown states and parameters listed in the table (4.4). The sensitivity analysis in this research is based on normalized perturbation in the parameter vector $\boldsymbol{\theta}$ by multiplying θ_i with $(1 + \epsilon_i)$. The reason we normalize the perturbations is that it makes it possible to obtain normalized

parameter error bounds directly from Fisher analysis. In this way, parameter estimation errors can be compared for different parameters.

One can quantify the identifiability of the model's parameters from their covariance matrix. Eq. (4.15) presents the covariance matrix derived from the expected values of estimation accuracies. The diagonal elements of this matrix are the expected errors squared for parameter vector $\boldsymbol{\theta}$.

$$\boldsymbol{\theta} = [\theta_1, \theta_2, \ \ldots, \ \theta_i]^T \tag{4.14}$$

where θ_i is the ith parameter in this vector.

$$Cov(\hat{\boldsymbol{\theta}}) = \begin{pmatrix} E\{(\hat{\theta}_1 - \theta_{1,t})^2\} & \ldots & E\{(\hat{\theta}_1 - \theta_{1,t})(\hat{\theta}_i - \theta_{i,t})\} \\ \vdots & \ddots & \vdots \\ E\{(\hat{\theta}_i - \theta_{i,t})(\hat{\theta}_1 - \theta_{1,t})\} & \ldots & E\{(\hat{\theta}_i - \theta_{i,t})^2\} \end{pmatrix}, \tag{4.15}$$

where $\hat{\theta}_i$ is the ith estimated parameter and the $\theta_{i,t}$ is the true value for the ith parameter.

The Cramér-Rao theorem states that the best covariance matrix achievable by any unbiased estimator is equal to the inverse of the Fisher information matrix. This theorem is mathematically expressed in Eq. (4.16):

$$Cov(\hat{\boldsymbol{\theta}}) \geq CRLB = \mathbf{F}^{-1} \tag{4.16}$$

The diagonal elements of the inverse of the Fisher information matrix provide the best-achievable estimation variance for each element of the vector $\boldsymbol{\theta}$. Dividing each parameter's variance by the nominal value of the parameter squared provides a normalized estimation variance, useful for comparing the accuracy levels with which different parameters can be estimated [114].

In order to have a benchmark for comparing the results of identifiability study in this chapter, we first solve for the $CRLBs$ for 19 parameters and initial states for a fully charged Li-S battery which is undergoing a cyclic input current of constant current discharge and charge for 8 hours. Then we optimize the current profile for maximizing the parameters and initial states identifiability in the next section.

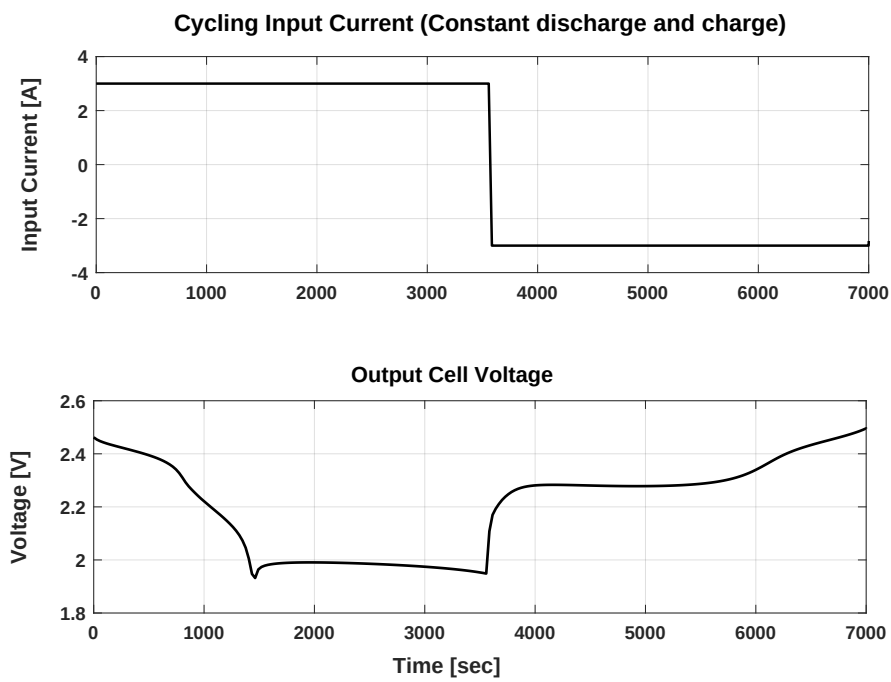

Figure 4.4: One period of cycling Li-S battery with a constant current of $\pm$ 3[A].

Figure (4.4) shows a periodic constant discharging input (-3 $[A]$) followed by a constant charging input (3 $[A]$) profile for 8 hours and the corresponding cell voltage for

an Li-S battery with a capacity of $3.2[Ah]$. The cell is initialized at its fully charged state prior to the application of the constant discharge current. We simulate the battery output voltage by numerically solving the zero-dimensional model presented in Section (4.3). We then solve for the model's Fisher identifiability matrix by perturbing the parameters and initial states and then determining the sensitivity of the simulated output to those perturbations numerically. Using the parameters and initial state sensitivity profiles, one can calculate the Fisher information matrix and Cramér-Rao lower bound. The first column of Table (4.5) represents the normalized estimation variances for all the 19 unknown parameters and initial states that we obtained numerically.

4.5 Periodic Optimal Input Current Design

In this section, we aim to derive a periodic current input trajectory that maximizes the combined identifiability of the nineteen parameters and initial states of the 0D electrochemical Li-S battery model. One way to do that is to maximize the determinant of the Fisher information matrix subject to the battery dynamics and inequality bounds on the input current. This approach makes intuitive sense because the Fisher information matrix places a bound on the best-achievable parameter estimation accuracy for any unbiased estimator. Therefore, maximizing the determinant of this matrix leads to maximizing identifiability of the parameter vector $\boldsymbol{\theta}$ [138, 139]. The resulting optimal input current would be a periodic trajectory that returns the battery back to the same origin of its initial states, if periodicity constraints are imposed on this trajectory optimization problem. One can solve this trajectory optimization problem using a number of different methods, in-

cluding numerical methods involving the use of a truncated Fourier series to approximate and parameterize the optimal input trajectory. For example, Eq. (4.13) presents the input current as a cyclic Fourier series with three harmonics, and we optimize its coefficients over a bounded domain for maximizing Fisher identifiability. Alternative approaches for trajectory optimization do exist, including the use of the Pontryagin minimum principle to analyze the fundamental structure of the optimal trajectory: an approach highlighted in the next chapter of this dissertation.

$$
\begin{aligned}
I(\boldsymbol{\phi}, k\delta t) = \phi_1 sin(\phi_2.k\delta t) + \phi_3 cos(\phi_2.k\delta t) \\
+ \phi_4 sin(2\phi_2.k\delta t) + \phi_5 cos(2\phi_2.k\delta t) \\
+ \phi_6 sin(3\phi_2.k\delta t) + \phi_7 cos(3\phi_2.k\delta t)
\end{aligned}
\tag{4.13}
$$

The goal of this section is to minimize the theoretical lower bound on the Li-S battery parameters estimation covariance matrix with respect to input current. Minimizing the CRLB is analogous to maximizing the determinant of Fisher information matrix. We address this minimization problem in two different approaches. First, we optimize the periodic current coefficients by maximizing the determinant of FIM within bounded optimization domain in order to prevent infinitely large charge and discharge currents $3\ C$. However, the problem of maximizing the FIM is a non-convex optimization problem, causing the solution to be a boundary-optimal solution that brings some or all of the optimization variables to the edges of the optimization domain. This motivates the second problem formulation, which is to formulate a Pareto optimization problem that

optimizes a weighted sum of a Fisher information maximization objective and an input current trajectory L_2 norm minimization problem. By optimizing both objectives simultaneously, through linear scalarization, one hopes to protect the battery from excessive current without hitting potentially arbitrary, or ad-hoc, optimization bounds. Both optimization problem formulations are explored in this work.

Eq. (4.17) defines the first optimization problem and its constraints.

$$
\begin{aligned}
&\min_{\mathbf{I}(\boldsymbol{\phi})} \; J_1 = -Det(\boldsymbol{F}) \\
&where : \boldsymbol{\phi} = [\phi_1,\ \phi_2, \ldots,\ \phi_7] \\
&Subject\ to : \\
&\qquad \dot{X} = f(\mathbf{x}, I) \\
&\qquad V = h(\mathbf{x}, I) \\
&where : \mathbf{x} = [m_1,\ \ldots,\ m_5,\ m_{S_p},\ \alpha]^T \\
&-3 \leq \boldsymbol{\phi}_i \leq 3
\end{aligned}
\tag{4.17}
$$

We use a particle swarm optimization (PSO) algorithm to solve this optimization problem. This algorithm scans the optimization domain with 10 particles to find the optimum, and runs for 60 iterations. In the first approach of optimizing the input current trajectory, we only aimed for maximizing the determinant of Fisher information matrix under certain bounds on the variables that keep the battery in safe cycling region. Eq. (4.18) shows the resulting optimal periodic input current ($I_{Opt}\#1$) with the optimized

variable vector ϕ_{opt} as a result of the first approach.

$$
\begin{aligned}
I(\phi_{opt}, k\delta t)\#1 = & -2.99 \times sin(1.65\ k\delta t) - 2.39 \times cos(1.65\ k\delta t) \\
& - 1.77 \times sin(3.3\ k\delta t) - 0.67 \times cos(3.3\ k\delta t) \\
& - 0.88 \times sin(4.95\ k\delta t) + 3 \times cos(4.95\ k\delta t)
\end{aligned} \tag{4.18}
$$

We simulated cycling the Li-S battery's 0D electrochemical model using the optimal periodic input current in Eq. (4.18), corresponding to almost eight cycles over 8 hours. Figure (4.5) shows that one cycle of the optimal current input and the corresponding output cell voltage has a period of approximately 1 hour.

We now numerically analyze the normalized CRLB based on the sensitivity profiles for the above optimal trajectory. Integration of each parameter's sensitivity squared furnishes the Fisher information matrix's diagonal elements. The remaining elements in the Fisher information matrix are obtained through numerical integration of off-diagonal products of the sensitivities in sensitivity matrix. The CRLB matrix is then obtained by solving the inverse of the FIM. The second column of Table (4.5) represents the CRLB for individual parameters and initial states after cycling the Li-S battery based on this input trajectory for 8 hours. The arrows in this table show the change in the CRLB for an optimal periodic input current versus a baseline, non-optimized periodic discharge-charge current. According to the second column of Table (4.5) the estimation accuracies for 18 out of 19 parameters and initial states of the Li-S battery improve as a result of the first optimal input trajectory ($I_{Opt}\#1$). Specifically, the Fisher identifiability improvement for

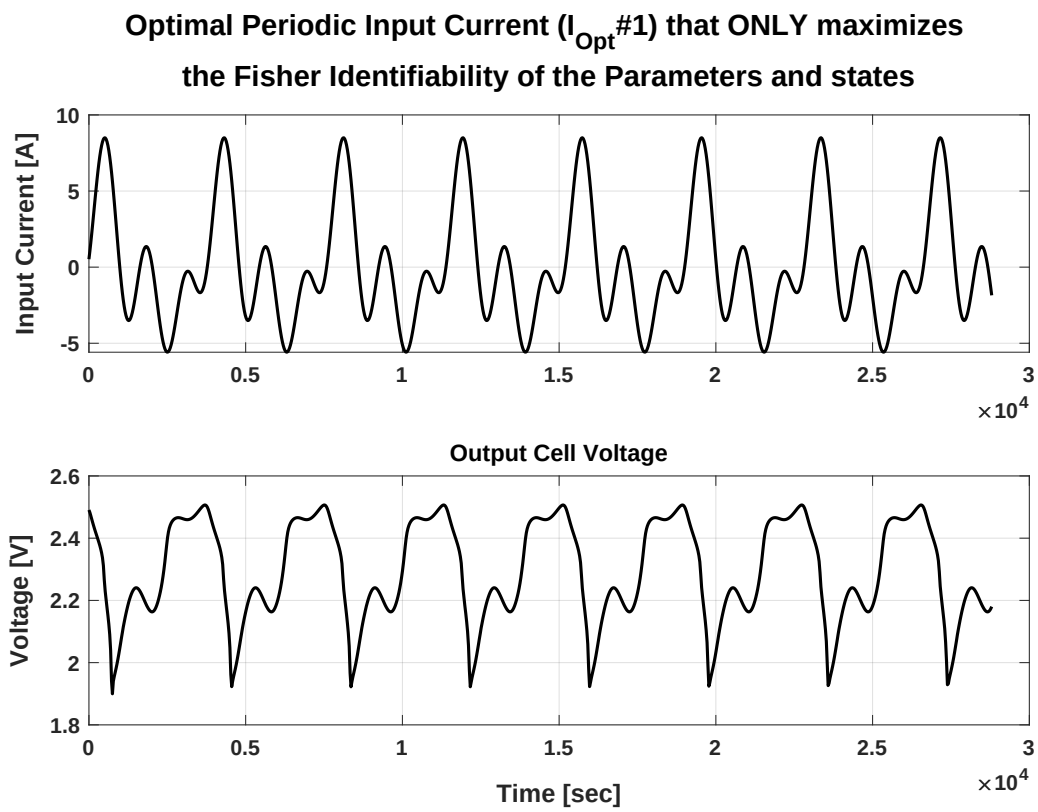

Figure 4.5: Li-S battery optimal cycling current and voltage curves.

initial precipitated sulfur m^0_{Sp} is $\%67.2$, for S_sat is $\%73.9$, for $\%K_p$ is $\%81.3$, and for the initial mass pf the lowest polysulfide $m^0_{s^{2-}}$ that precipitates as Li_2S is $\%74.2$.

The bottom line is that after cycling the battery with the optimized periodic input current for 8 hours, the estimation error shrinks by one to two orders of magnitude for all the Li-S unknown parameters and initial states except the porosity ratio ω, whose identifiability remains almost the same compared to the test of cycling the battery with a constant charge/discharge current. Interestingly, the improvement in the estimation errors is occurring mostly because the optimal cycling current trajectory tends to linger on the low plateau, particularly during battery charging. Figure (4.6) shows one cycle

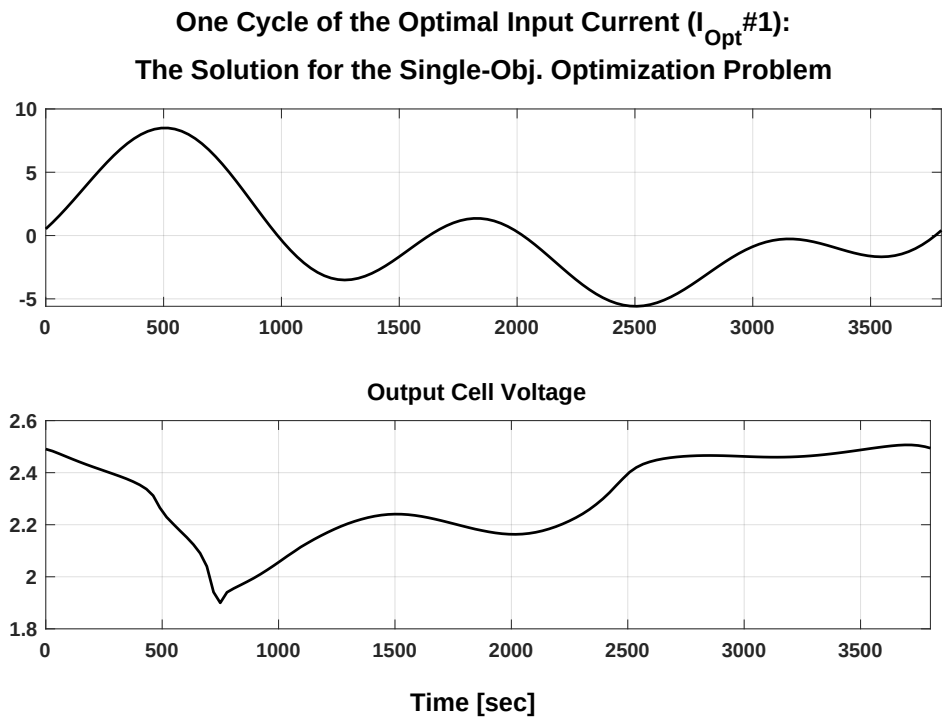

Figure 4.6: One cycle of the optimal input current trajectory.

of this current input and its corresponding voltage output. According to this figure, the input trajectory drains the fully charged battery down to its dip point more than three times faster than charging it back to its initial state. A possible explanation lies in the poorly identifiable precipitation parameters and initial states whose dynamics are mostly triggered during the low voltage plateau. Therefore, the optimal input current causes the battery to linger more on its low voltage plateau to capture more information about the

less identifiable parameters.

$$
\begin{aligned}
&\min_{\mathbf{I}(\boldsymbol{\phi})} \; J_2 = -Det(\boldsymbol{F}) + \int_0^{N.\delta t} w \times I_{opt}^2 dt \\
&where : \boldsymbol{\phi} = [\phi_1,\ \phi_2, \ldots,\ \phi_7] \\
&-10 \leq \boldsymbol{\phi}_i \leq 10
\end{aligned}
\tag{4.19}
$$

In the second approach of optimizing the input current for maximizing the Fisher identifiability, we include the fact that we are not allowed to cycle the battery beyond its safe limits into our optimization problem. Eq. (4.19) represents the second optimization problem with an additional term that minimizes the magnitude of the optimal current as well as maximizing the determinant of FIM. These two objectives are in opposition, so the problem is a Pareto optimization problem. Using weighted integration, we make the effect of input squared comparable with the FIM determinant. Therefore, the w is chosen to be in the order of magnitude of 50. Moreover, we introduce a large optimization domain to protect the Particle swarm optimization algorithm from deliberately finding the optimal solutions near the bounds. Eq. (4.20) is the optimal three harmonics input current where its coefficients are optimized based on running the particle swarm optimization algorithm for 10 particles and 60 iterations. Figure (4.7) shows this optimal input current trajectory and its corresponding voltage curve that both maximizes the Fisher identifiability of the Li-s battery parameters and initial states and also minimizes the integration of the input current squared for protecting the battery.

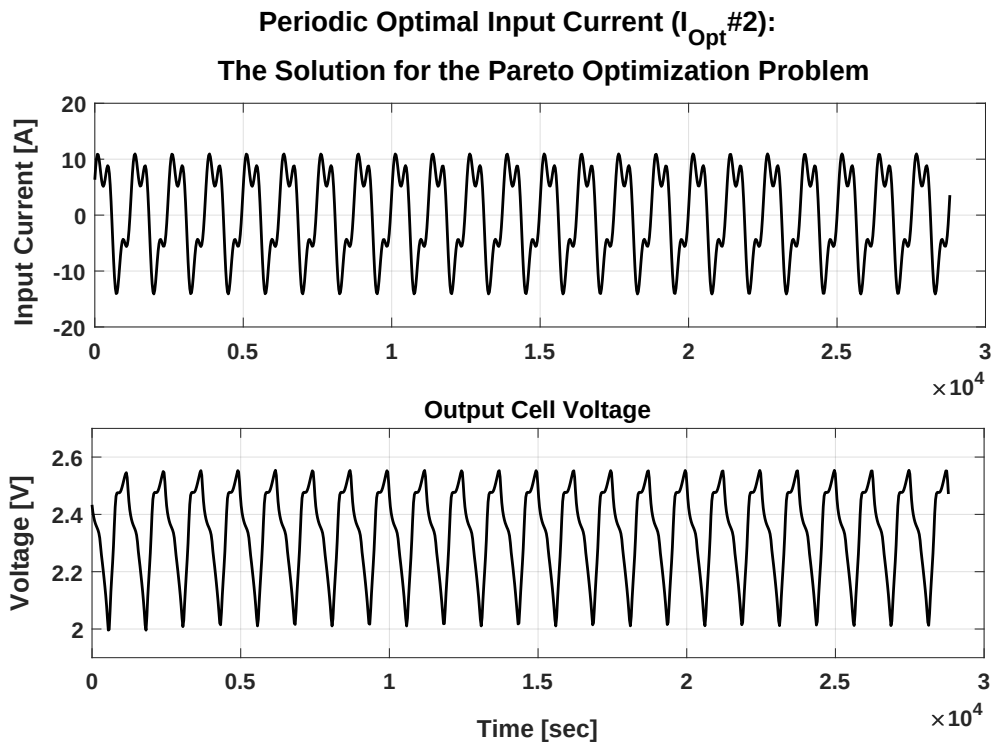

Figure 4.7: Li-S battery optimal cycling current and voltage curves.

$$
\begin{aligned}
I(\phi_{opt}, k\delta t)\#2 = & -3.99 \times sin(1.74\, k\delta t) + 0.013 \times cos(1.74\, k\delta t) \\
& - 0.5465 \times sin(3.48\, k\delta t) - 2.53 \times cos(3.48\, k\delta t) \\
& + 0.145 \times sin(4.95\, k\delta t) + 0.6877 \times cos(4.95\, k\delta t)
\end{aligned} \tag{4.20}
$$

Two interesting differences between ($I_{Opt}\#2$) and ($I_{Opt}\#1$) are (i) the Pareto optimized current has a higher frequency and (ii) it does not make the battery to linger on the low voltage plateau as much as the first optimal current does for maximizing Fisher identifiability. Significant improvements in Fisher identifiability are obtained for almost all parameters with the Pareto formulation compared to the single-objective formulation,

reflecting the more generous bounds on the optimization variables employed in the Pareto formulation.

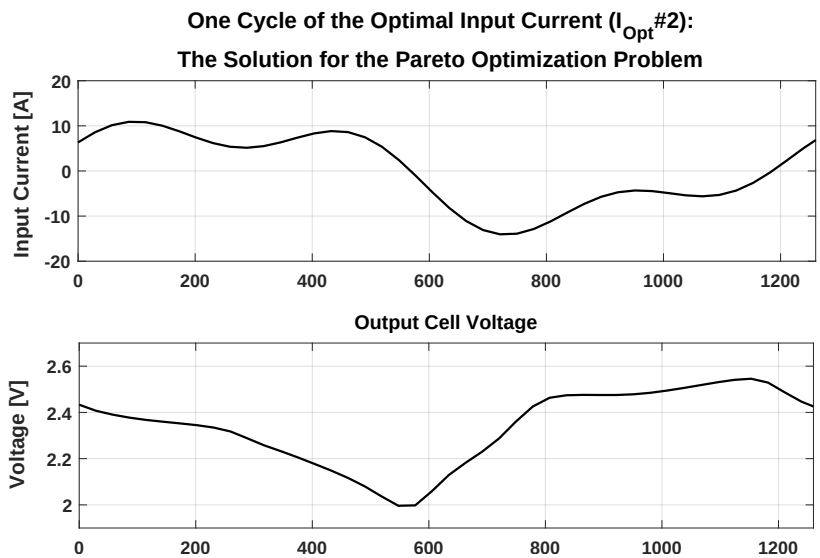

Figure 4.8: One cycle of the Pareto optimization result

4.6 Conclusion

The work presented in this chapter includes the derivation and simulation of an optimized periodic current trajectory to maximize identifiability of the states and parameters of the 0D electrochemical Li-S battery model. The current trajectory is designed to maximize the Fisher identifiability of the total set of 19 parameters of the model. With a cycling time of eight hours, the parameters estimation variances are reduced by a significant amount using the optimal periodic current input.

One important note is that the precipitation parameters such as the precipitated mass m_{S_p} do not directly affect the output battery voltage V. Instead, the impact of precipitation on this output voltage takes place indirectly, through other species dynamics. This

causes the observability of the precipitation parameters to be fairly weak. These parameters are more involved in the dynamics of the battery on its low voltage plateau region. Perhaps this explains the fact that the single-objective optimal battery input trajectory lingers in the low plateau region.

Table 4.5: Normalized variances for 19 parameters and initial states of the Li-S battery model for non-optimized vs optimized currents.

Params.	**Periodic $\pm$ 3 [A]**	**Periodic Single-Obj.**	**Change**
	CRLB		
$m^0_{s_8}$	2.45E-07	1.21E-07	$\downarrow$
$m^0_{s_8^{2-}}$	0.0103	0.001	$\downarrow$
$m^0_{s_6^{2-}}$	0.093	0.014	$\downarrow$
$m^0_{s_4^{2-}}$	13.956	4.518	$\downarrow$
$m^0_{s^{2-}}$	1.43E10	3.68E09	$\downarrow$
E^0_1	6.56E-09	2.73E-09	$\downarrow$
E^0_2	3.13E-07	1.17E-07	$\downarrow$
E^0_3	1.09E-07	3.33E-08	$\downarrow$
E^0_4	3.72E-08	2.61E-08	$\downarrow$
i^0_1	5.79E-05	2.29E-05	$\downarrow$
i^0_2	2.805	0.328	$\downarrow$
i^0_3	1.212	0.238	$\downarrow$
i^0_4	0.251	0.221	$\downarrow$
K_p	8.13E-07	1.52E-07	$\downarrow$
S_{sat}	3.62E04	9.45E03	$\downarrow$
$m^0_{S_p}$	2.68E09	8.79E08	$\downarrow$
v	5.739	0.752	$\downarrow$
ω	2.22E-04	9.44E-04	$\uparrow$
γ	0.0018	7.96E-04	$\downarrow$

Table 4.6: Normalized variances for 19 parameters and initial states of the Li-S battery model for single-objective vs Pareto optimized currents.

Params.	**Periodic Single-Obj.**	**Periodic Pareto-Obj.**	**Change**
	CRLB		
$m^0_{s_8}$	1.21E-07	5.16E-08	$\downarrow$
$m^0_{s_8^{2-}}$	0.001	4.28E-04	$\downarrow$
$m^0_{s_6^{2-}}$	0.014	0.0035	$\downarrow$
$m^0_{s_4^{2-}}$	4.518	0.9105	$\downarrow$
$m^0_{s^{2-}}$	3.68E09	6.31E08	$\downarrow$
E^0_1	2.73E-09	2.37E-09	$\downarrow$
E^0_2	1.17E-07	4.09E-08	$\downarrow$
E^0_3	3.33E-08	1.80E-08	$\downarrow$
E^0_4	2.61E-08	4.09E-08	$\uparrow$
i^0_1	2.29E-05	4.79E-06	$\downarrow$
i^0_2	0.328	0.066	$\downarrow$
i^0_3	0.238	0.0491	$\downarrow$
i^0_4	0.221	0.0581	$\downarrow$
K_p	1.52E-07	5.78E-08	$\downarrow$
S_{sat}	9.45E03	2.73E03	$\downarrow$
$m^0_{S_p}$	8.79E08	2.93E08	$\downarrow$
v	0.752	0.181	$\downarrow$
ω	9.44E-04	3.42E-04	$\downarrow$
γ	7.96E-04	4.17E-04	$\downarrow$

Chapter 5: On the Structure of the Optimal Input for Maximizing Lithium-Ion Battery Thermal Parameter Identifiability

5.1 Overview

This chapter investigates input trajectory optimization for parameter identifiability in a lithium-ion battery temperature cycling experiment. Such optimal experimental design can improve battery parameterization speeds and accuracies significantly. These potential improvements are well-established in the literature for thermal, electrochemical, and multi-physics battery models. However, to the best of the author's knowledge, the fundamental structure of the resulting optimal test trajectories is relatively less-explored. The chapter examines the problem of optimizing the trajectory of thermal chamber temperature versus time in a lithium-ion battery temperature cycling test. This is posed as a Pareto-optimal control problem, with the competing objectives being the maximization of the Fisher identifiability of the battery's thermal time constant versus the minimization of the L_2 norm of the control input. Pontryagin analysis reveals that the optimal trajectory is a switching trajectory constrained within battery cell temperature bounds, where the rate at which the solution proceeds from one bound to another is governed by the Pareto weight. Solving this problem numerically, using dynamic programming, supports these

insights from Pontryagin analysis.

From a high-level, fundamental perspective, this chapter represents the conclusion of a progression of key ideas pertaining to multi-compartment dynamic system parameter identifiability. Specifically, while Chapters 2, 3, and 4 illustrated the importance of identifiability analysis, the degree to which poor input shaping can worsen identifiability, and the degree to which optimal input shaping can improve identifiability, the goal in this chapter is to utilize a fundamental tool from optimal control theory to better understand the structure of the identifiability-optimizing input profile for a given dynamic system. To the best of the author's knowledge, the use of Pontryagin methods to perform this analysis is novel, particularly in the context of optimal battery cycling. Therefore, in a sense, this chapter represents a progression from the application of identifiability analysis to pratical research problems on the one hand to the pursuit of new fundamental mathematical frameworks for identifiability analysis on the other hand. [1]

5.2 Introduction

This chapter examines the thermal cycling of a lithium-ion battery. This is a well-established test process where a battery cell is placed in a thermal chamber that varies ambient temperature and measures response signals such as cell voltage, surface temperature, core temperature, etc. Thermal cycling is typically used for estimating battery parameters such as entropy coefficients and thermal time constants. Such estimation is typically performed offline, in a laboratory, as a precursor to the design of online model-

[1] This work already appears as a peer-reviewed publication in the Proceedings of the 2020 American Control Conference.

based battery management systems.

The literature already provides models of the temperature dynamics of lithium-ion batteries. This includes work by Guo *et al.* [140] and Kumaresan *et al.* [141]. Studies by Maleki *et al.* [142], Tian *et al.* [143], and others already parameterize battery models from experimental data. Moreover, work by researchers including Marcicki *et al.* [144] already uses experimentally-parameterized models for online battery estimation/control applications. Beneath these successes lies a fundamental challenge, evident from references including Schmidt *et al.* [145]: lithium-ion battery parameters are not always *identifiable* from experimental data. Tools such as sensitivity analysis and Fisher information analysis can furnish analytic bounds on battery parameter identifiability. See, for example, research by: Sharma and Fathy [146]; Zhang *et al.* [147]; and Lin and Stefanopoulou [148]. Moreover, one can optimize battery test protocols in order to improve parameter identifiability. Examples of such optimization include work by Forman *et al.* [10], Rothenberger *et al.* [12], Mendoza *et al.* [14], and Park *et al.* [15].

In summary, there is a growing literature on the optimization of battery experiments for parameter identifiability. Such optimization has the potential to improve parameter estimation speeds and accuracies considerably, leading to better utilization of costly laboratory test setups and time. These potential benefits are well-established in the literature for thermal, electrochemical, and multi-physics battery models. However, to the best of the author's knowledge, fundamental insights into the structure of information-maximizing battery test protocols are still relatively scarce in the literature.

The goal of this research is to address the above gap, in the specific context of thermal battery cycling. The chapter presents an analytic examination of the structure

of the solution to a battery thermal cycle optimization problem. It poses a thermal cycle optimization problem where the competing Pareto objectives are Fisher identifiability optimization and control input minimization. Battery cell temperature is constrained in this problem formulation, reflecting the need to avoid undesirable phenomena such as thermal runaway. The chapter examines this problem using Pontryagin methods for two scenarios, one where the battery cell temperature constraint is active, and one where this constraint is inactive. The chapter follows the approach presented in Geering [149, 150] when analyzing the constrained solution arc. This analysis reveals that the optimal solution trajectory has a switching structure. The chapter observes this switching structure numerically, using a dynamic programming study. Finally, the chapter end by summarizing the conclusions of this work.

5.3 Problem Formulation

Thermal cycling experiments can be used for estimating the parameters governing a battery cell's thermal behavior, such as the cell's thermal time constant. They can also be used for estimating the parameters governing the coupling between the cell's thermal and electrochemical behavior, such as the cell's ohmic resistance and entropy coefficient. The entropy coefficient of a lithium-ion battery quantifies the sensitivity of its open-circuit voltage with respect to its underlying temperature, and has a direct impact on the rate of reversible heat generation during charge/discharge. For simplicity, the focus of this research is on estimating a parameter governing the thermal behavior of a battery - namely, its thermal time constant. However, the chapter begins this analysis with a general model

that can be used for both thermal and thermo-electrochemical parameter identification. Specifically, consider the following first-order lumped-parameter model of lithium-ion battery cell temperature, by Bernardi *et al.* [151]:

$$\frac{dT}{dt} = \frac{hA}{mC_p}(T_{amb} - T) + \frac{C(SOC)}{mC_p}IT + \frac{R}{mC_p}I^2 \tag{5.1}$$

The above model captures four key phenomena. First, the term $mC_p\frac{dT}{dt}$ represents the battery cell's thermal energy storage ability, where T, m, and C_p denote the cell's temperature, mass, and specific heat capacity, respectively. Second, the term $hA(T_{amb} - T)$ represents convective heat transfer between the battery cell and the surrounding thermal chamber, where h, A, and T_{amb} denote the convection heat transfer coefficient, convection area, and chamber temperature, respectively. Third, the term $C(SOC)IT$ represents reversible heat generation due to entropic effects. Fourth, irreversible heat generation is represented by I^2R, where R is the cell's Ohmic resistance. Nominal parameters for this model, corresponding to a commercial 26650-sized $LiFePO_4$ battery cell, are taken from previous research by Mendoza *et al.* [113] and shown in Table (5.1) below.

This research examines the Fisher identifiability of the lumped thermal parameter hA/mC_p in a thermal cycling experiment. Thermal cycling experiments involve setting the battery charge/discharge current, I, to zero, and adjusting the ambient chamber temperature, T_{amb} as a controllable quantity. One can then measure either the battery cell temperature, T, or open-circuit voltage, or both. Given our focus on estimating the cell's thermal time constant, we choose cell temperature, T, as a measured output. This leads

Table 5.1: Battery thermal model parameters

Parameter	values, Unit
h	13.45 $[J/s.m^2K]$
A	0.004 $[m^2]$
m	50e-3 $[kg]$
Cp	1000 $[J/Kg.k]$
I	0 $[Amp]$
R	2.21e-2 $[\Omega]$

to the state-space model below:

$$\begin{aligned} \dot{x}_1(t) &= u \\ \dot{x}_2(t) &= \theta(x_1(t) - x_2(t)) \\ y(t) &= x_2(t), \end{aligned} \tag{5.2}$$

where θ represents thermal parameter of the battery (hA/mCp). This parameter's reciprocal is the time constant of the battery temperature dynamics. The state variables $x_1(t)$ and $x_2(t)$ denote the temperatures T_{amb} and T, respectively, and the output $y(t)$ denotes the battery temperature measurement. The work in this research treats the rate of change of ambient temperature as the input variable $u(t)$ in order to explore physically feasible battery thermal cycling tests with reasonable values of this rate.

To optimize the battery thermal test trajectory for identifiability, one must first com-

pute the sensitivity of output temperature measurement to the parameter θ. We use Eq. (5.2) to perform this sensitivity analysis. To derive an equation for the desired sensitivity, the two states equations are solved assuming given initial temperatures $x_{1,0}$ and $x_{2,0}$ as follows:

$$
\begin{aligned}
x_1(t) &= (x_{1,0}) + \int_0^t u(\tau) d\tau \\
x_2(t) &= (x_{2,0})\, e^{-\theta t} + (x_{1,0}) \int_0^t \theta x_1(\tau)\, e^{-\theta(t-\tau)} d\tau \\
y(t) &= x_2(t) \\
s(t) &= \frac{\partial y(t)}{\partial \theta} \\
&= -t(x_{2,0})\, e^{-\theta t} + (x_{1,0}) \int_0^t x_1(\tau)\, e^{-\theta(t-\tau)} d\tau \\
&\quad + (x_{1,0}) \int_0^t -\theta(t-\tau) x_1(\tau)\, e^{-\theta(t-\tau)} d\tau
\end{aligned}
\tag{5.3}
$$

Given this sensitivity analysis, one can use Fisher analysis to determine the theoretical Cramér-Rao bound on the accuracy with which the parameter θ can be estimated. In performing this Fisher analysis, we assume that the model in Eq. (5.2) provides an accurate representation of the true battery temperature dynamics. Moreover, we assume that the output temperature, $y(t)$, is measured at discrete sampling instants separated by a fixed sampling time δt. Noise can affect these output measurements, and an assumed noise model is needed in order to perform Fisher information analysis. In this work, we assume that this measurement noise is a zero-mean, white, Gaussian process with a variance σ^2. Given these assumptions, one can employ Fisher information analysis to de-

termine the best-achievable battery parameter estimation accuracy, assuming an unbiased estimator [137],[152]. The Fisher information matrix in this case is a scalar since there is only one unknown parameter in Eq. (5.2). It is given by:

$$\mathbf{F} = \frac{1}{\sigma^2} \sum_{k=1}^{N} \mathbf{s}(k\delta t)\mathbf{s}(k\delta t)^T, \tag{5.4}$$

where N is the number of measurements of the battery temperature and $\mathbf{s}(t)$ is a vector containing the sensitivities of the model's output, $y(t)$, to small perturbations in the parameters.

The Fisher information metric in Eq. (5.4) can be approximated as an integral with respect to time for sufficiently small sampling time δt.

$$\mathbf{F} \approx \frac{1}{\sigma^2 \delta t} \int_0^{N\delta t} \mathbf{s}(\tau)\mathbf{s}(\tau)^T d\tau \tag{5.5}$$

Since there is only one sensitivity equation corresponding to one parameter perturbation in this work, Eq. (5.5) can be written in form of a scalar sensitivity function:

$$\mathbf{F} \approx \frac{1}{\sigma^2 \delta t} \int_0^{N\delta t} s(\tau)^2 d\tau \tag{5.6}$$

where $s(t)$ is the sensitivity as a function of time derived in Eq. (5.3). Given this approximate expression for Fisher information, one can formulate the following test trajectory

optimization problem:

$$
\begin{aligned}
\min_{u} \quad & \int_0^T -s^2 + \alpha u^2 dt \\
\text{s.t.} \quad & \dot{x}_1 = u \\
& \dot{x}_2 = \theta(x_1 - x_2) \\
& \boldsymbol{x}(0) : Given \\
& T_{min} \leq x_2 \leq T_{max}
\end{aligned}
\tag{5.7}
$$

The optimization objective is a Pareto-weighted summation of two competing objectives, namely, maximizing Fisher information and minimizing the L_2 norm of the control input, with α serving as the Pareto weight. Penalizing the control input is important because of the physical limitations on the rate at which a thermal chamber can adjust its temperature versus time. Moreover, the imposition of upper and lower bounds on chamber temperature is important for battery safety. Constraining chamber temperature is relatively less critical considering the fact that the range of operating chamber temperatures is typically far in excess of battery safety limits.

In the standard formulation of an optimal control problem, the optimization objective is assumed to be an explicit function of the state and input trajectories versus time [153]. However, in the Eq.(5.7), the objective function is not in this standard form. In particular, Eq. (5.3) shows that the sensitivity, $s(t)$ is not an explicit function of states and input. Therefore, there is a need to introduce the sensitivity, $s(t)$ into the optimal control

problem as a new state variable, as shown in Eq.(5.8).

$$
\begin{aligned}
s(t) + tx_2(t) &= \int_0^t (1+\tau\theta)x_1(\tau)e^{-\theta(t-\tau)}d\tau \\
\dot{s}(t) + t\dot{x}_2(t) + x_2(t) &= (1+\theta t)x_1(t) - \theta(s(t) + tx_2(t)) \\
\dot{s}(t) &= x_1(t) - x_2(t) - \theta s(t)
\end{aligned}
\tag{5.8}
$$

Given the above state equation for the sensitivity variable, the optimal control problem can now be written as follows:

$$
\begin{aligned}
\min_u \quad & \int_0^T -x_3^2 + \alpha u^2 dt \\
\text{s.t.} \quad & \dot{x}_1 = u \\
& \dot{x}_2 = \theta(x_1 - x_2) \\
& \dot{x}_3 = x_1 - x_2 - \theta x_3 \\
& \boldsymbol{x}(0) : Given \\
& T_{min} \leq x_2 \leq T_{max}
\end{aligned}
\tag{5.9}
$$

The main goal of this research is to use Pontryagin analysis to investigate the structure of the solution to this trajectory optimization problem.

5.4 Pontryagin Analysis for Optimal Input Design

This section applies Pontryagin analysis to: (i) the scenario where the constraints on battery cell temperature are inactive; (ii) the scenario where one of these constraints (either the upper or lower cell temperature bound) ia active; and (iii) the transitions between these two solution arcs. When the battery cell temperature constraints are inactive, the Hamiltonian is given by:

$$\begin{aligned} H = &-x_3^2 + \alpha u^2 + \lambda_1 u + \lambda_2 \theta (x_1 - x_2) \\ &+ \lambda_3 (x_1 - x_2 - \theta x_3) \end{aligned} \tag{5.10}$$

Differentiating this Hamiltonian with respect to the three state variables furnishes the following co-state equations:

$$\begin{aligned} \dot{\lambda}_1 &= -H_{x_1} = -\lambda_2 \theta - \lambda_3 \\ \dot{\lambda}_2 &= -H_{x_2} = \lambda_2 \theta + \lambda_3 \\ \dot{\lambda}_3 &= -H_{x_3} = 2x_3 + \lambda_3 \theta \end{aligned} \tag{5.11}$$

The optimal battery temperature trajectory must minimize the above Hamiltonian with respect to the control input, $u(t)$, at every instant in time. Because the Pareto weight, α, is positive by construction of the multi-objective optimization problem, the Hamiltonian is convex with respect to $u(t)$. Therefore, an interior optimum exists, corresponding

to the condition $\partial H/\partial u = 0$, i.e.,

$$u^* = -\frac{\lambda_1}{2\alpha} \tag{5.12}$$

Substituting the above optimal control input into the state equations couples the state and co-state dynamics. The end result is an autonomous linear system of state and co-state equations, as shown below:

$$\begin{bmatrix} \dot{\mathbf{x}} \\ \dot{\lambda} \end{bmatrix} = \begin{bmatrix} 0 & 0 & 0 & \frac{-1}{2\alpha} & 0 & 0 \\ \theta & -\theta & 0 & 0 & 0 & 0 \\ 1 & -1 & -\theta & 0 & 0 & 0 \\ 0 & 0 & 0 & 0 & -\theta & -1 \\ 0 & 0 & 0 & 0 & \theta & 1 \\ 0 & 0 & 2 & 0 & 0 & \theta \end{bmatrix} \begin{bmatrix} \mathbf{x} \\ \lambda \end{bmatrix} \tag{5.13}$$

where $\mathbf{x}(t)$ and $\lambda(t)$ are the vectors of state and co-state variables, respectively. The characteristic equation corresponding to these state and co-state dynamics can be written as follows, in terms of the Laplace variable s:

$$s^6 - 2\theta^2 s^4 + (\theta^4 - \frac{1}{\alpha})s^2 = 0 \tag{5.14}$$

The above characteristic equation is unstable for all possible (i.e., finite and positive) values of the Pareto weight, α. Two of the eigenvalues of this characteristic equation are zero regardless of α, and one can show using a parametric root locus plot that either one or two of the four remaining eigenvalues will exhibit instability, depending on the value of α. Moreover, the above autonomous dynamic system is observable from the state variable

x_2: a fact that can be shown by computing the system's observability test matrix with x_2 as the output. This means that the trajectories of all of this autonomous system's state variables can be expressed in terms of $x_2(t)$ and its time derivatives. Therefore, if the above autonomous system's initial condition excites its underlying instability, the time history of $x_2(t)$ will contain an unstable, exponentially growing component. Together, these observations indicate that the battery cell temperature bounds cannot remain inactive indefinitely, for arbitrary initial conditions of the above system's state and co-state variables. The optimal cell temperature trajectory migrates from one bound to another at a rate that depends on the eigenvalues of the above autonomous system of equations, which are in turn dependent on the Pareto weight α. This concludes our analysis of the scenario where the battery cell temperature bounds are inactive. When one of the bounds is active, Pontryagin analysis can proceed as follows (see references such as Geering [149] for more details). Let the battery cell temperature be constrained as follows: $x_2 \in [T_{min}, T_{max}]$. The upper and lower bounds on this temperature are mutually exclusive. Therefore, only one of these bounds can be active at a given moment in time. Without loss of generality, consider the case where the upper bound is active. Then the constraint function $G(x) = x_2 - T$ must equal zero, where $T = T_{max}$ is a constant. The Hamiltonian must now be augmented with the lowest-order time derivative of this constraint function in which the input variable, $u(t)$, appears explicitly. Two derivatives of the constraint

function are needed for this purpose, as shown below:

$$
\begin{aligned}
G(x) &= x_2 - T \\
\frac{d}{dt}G(x) &= \dot{x}_2 \\
&= \theta(x_1 - x_2) \\
\frac{d}{dt}(\frac{d}{dt}G(x)) &= \theta\dot{x}_1 - \theta\dot{x}_2 \\
&= u\theta - \theta^2(x_1 - x_2)
\end{aligned}
\tag{5.15}
$$

The Hamiltonian must now be augmented with the above second derivative of the constraint function, using a non-negative Lagrange multiplier $\mu_2(t)$. Based on this aug-

mented Hamiltonian, a new set of Pontryagin optimallity conditions arises:

$$
\begin{aligned}
\bar{H} &= -x_3^2 + \alpha u^2 + \lambda_1 u + \lambda_2 \theta (x_1 - x_2) \\
&\quad + \lambda_3 (x_1 - x_2 - \theta x_3) + \mu_2 (u\theta - \theta^2 (x_1 - x_2)) \\
u^* &= \frac{-1}{2\alpha}(\lambda_1 + \mu_2 \theta), \;\; \mu_2(t) \geq 0 \\
\dot{x}_1 &= u \\
\dot{x}_2 &= \theta (x_1 - x_2) \\
\dot{x}_3 &= x_1 - x_2 - \theta x_3 \\
\dot{\lambda}_1 &= -H_{x_1} + \mu_2 \frac{\partial}{\partial x_1}(u\theta - \theta^2 (x_1 - x_2)) \\
&= -\lambda_2 \theta - \lambda_3 - \mu_2 \theta^2 \\
\dot{\lambda}_2 &= -H_{x_2} + \mu_2 \frac{\partial}{\partial x_2}(u\theta - \theta^2 (x_1 - x_2)) \\
&= \lambda_2 \theta + \lambda_3 + \mu_2 \theta^2 \\
\dot{\lambda}_3 &= -H_{x_3} + \mu_2 \frac{\partial}{\partial x_3}(u\theta - \theta^2 (x_1 - x_2)) \\
&= 2x_3 + \lambda_3 \theta
\end{aligned}
\tag{5.16}
$$

If the battery cell temperature constraint is active for a nonzero amount of time, then $x_2(t)$ must be constant over that duration of time. This implies that $\dot{x}_2$ equals zero for this duration of time. Furthermore, because $\dot{x}_2 = \theta(x_1 - x_2)$, the chamber temperature $x_1(t)$ must also be constant and equal to the temperature bound during the above finite duration

of time. This, in turn, implies that $\dot{x}_1$ must equal zero. Therefore, the optimal control input, $u^*(t)$, must equal zero. These facts simplify the above Pontryagin conditions as follows:

$$
\begin{aligned}
x_2 &= T_{max} \\
u^* &= 0 \\
\mu_2 &= \frac{-1}{\theta}\lambda_1 \\
\dot{x}_1 &= u^* = 0 \\
\dot{x}_2 &= \theta(x_1 - x_2) = 0 \\
\dot{x}_3 &= -\theta x_3 \\
\dot{\lambda}_1 &= -\lambda_2\theta - \lambda_3 + \lambda_1\theta \\
\dot{\lambda}_2 &= \lambda_2\theta + \lambda_3 - \lambda_1\theta \\
\dot{\lambda}_3 &= 2x_3 + \lambda_3\theta
\end{aligned}
\tag{5.17}
$$

It is interesting to examine the value, from an information-theoretic perspective, of this solution arc. Suppose the solution trajectory enters the arc at some time $t = t_1$, and without loss of generality, let $t_1 = 0$ for simplicity. Then the trajectory of $x_3(t)$, over the course of this constrained solution arc, is given by:

$$x_3(t) = x_3(0)e^{-\theta t} \tag{5.18}$$

Moreover, recall that our (approximate) expression for Fisher information is proportional to the integral of $-x_3^2$ with respect to time. Together with Eq. (5.18), this implies that the total amount of (Fisher) information that can be collected over the course of this constrained solution arc is bounded, regardless of how long the solution lingers on this arc. Moreover, the rate at which (Fisher) information is gathered by lingering on this solution arc diminishes exponentially with time.

This concludes our analysis of the state-constrained solution arc. Next, we examine the transitions between the above two solution arcs. At least three observations can be made regarding these transitions. First, in order for the state-constrained solution arc to persist for a nonzero amount of time, it is necessary for both the battery cell temperature, $x_2(t)$ and the thermal chamber temperature $x_1(t)$ to hit the corresponding temperature bound (T_{min} or T_{max}) at the same moment in time. Otherwise, the Pontryagin conditions in Eq. (5.17) are impossible to fulfill. Second, departures from the constrained solution arc occur when the Lagrange multiplier, $\mu_2(t)$, is no longer greater than or equal to zero. This implies that such departures occur when λ_1 is no longer less than or equal to zero, since $\mu_2 = -\lambda/\theta$ (Eq. (5.17)). The time history of $\lambda_2(t)$ can be determined analytically over the course of the constrained solution arc. Plugging Eq. (5.18) into the differential

equation for λ_3 and solving for λ_3 gives:

$$\begin{aligned}
\lambda_3(t) &= \lambda_3(0)e^{\theta t} + \int_0^t 2x_3(\tau)e^{\theta(t-\tau)}d\tau \\
&= \lambda_3(0)e^{\theta t} + 2\int_0^t x_3(0)e^{-\theta\tau}e^{\theta(t-\tau)}d\tau \\
&= \lambda_3(0)e^{\theta t} - \frac{1}{\theta}x_3(0)(e^{-\theta t} - e^{\theta t})
\end{aligned} \tag{5.19}$$

Eq. (5.17) shows that $\dot{\lambda_1} + \dot{\lambda_2} = 0$. One can define two variables $z_1 = \lambda_1 + \lambda_2$ and $z_2 = \lambda_1 - \lambda_2$, and solve for z_2 as follow:

$$\begin{aligned}
z_2 &= \lambda_1 - \lambda_2 \\
\dot{z}_2 &= 2\theta\lambda_1 - 2\theta\lambda_2 - 2\lambda_3 \\
&= 2\theta z_2 - 2\lambda_3 \\
z_2(t) &= e^{2\theta t}z_2(0) - 2\int_0^t \lambda_3(\tau)e^{2\theta(t-\tau)}d\tau
\end{aligned} \tag{5.20}$$

Substituting Eq. (5.19) into the above expression gives us the following equation:

$$
\begin{aligned}
z_2(t) &= z_2(0)e^{2\theta t} \\
&\quad - 2e^{2\theta t}\int_0^t \lambda_3(0)e^{-\theta\tau} - \frac{1}{\theta}x_3(0)(e^{-3\theta\tau} - e^{-\theta\tau})\, d\tau \\
&= z_2(0)e^{2\theta t} - 2e^{2\theta t}[\frac{-1}{\theta}\lambda_3(0)(e^{-\theta t} - 1) + \\
&\frac{1}{3\theta^2}x_3(0)(e^{-3\theta t} - 1) - \frac{1}{\theta^2}x_3(0)(e^{-\theta t} - 1)]
\end{aligned}
\tag{5.21}
$$

Equation (5.21) provides a pathway for determining the time history of the co-state variable λ_1. Specifically, $\lambda_1 = \frac{1}{2}(z_1 + z_2)$, where z_1 is constant throughout the duration of the state-constrained solution arc. Departure from this solution arc occurs when λ_1 is no longer zero or negative.

Our third and final observation regarding the transitions between the unconstrained and constrained solution arcs pertains to the instantaneous co-state jumps associated with these transitions. Consider a time window $[t_1, t_2]$ such that one of the battery cell temperature bounds is active during this window, but inactive before and after this window. Then the three state variables – namely, chamber temperature, battery temperature, and sensitivity $x_3(t) = s(t)$ are continuous but not necessarily differentiable at t_1 and t_2. In contrast, however, the co-state variables may undergo jump discontinuities at these two moments in time. Without loss of generality, consider the moment in time $t = t_2$. Then

there exist two non-negative Lagrange multipliers, μ_0 and μ_1, such that:

$$
\begin{aligned}
\overrightarrow{\lambda}^*(t_{2-}) &= \overrightarrow{\lambda}^*(t_{2+}) + \sum_{i=0}^{L-1} \mu_i^* \overrightarrow{\nabla}_x G^{(i)}(x^*(t_2), t_2) \\
\Rightarrow \overrightarrow{\lambda}^*(t_{2-}) &= \overrightarrow{\lambda}^*(t_{2+}) + \mu_0^* \begin{bmatrix} 0 \\ 1 \end{bmatrix} + \mu_1^* \begin{bmatrix} \theta \\ -\theta \end{bmatrix} \\
\Rightarrow \lambda_1^*(t_{2+}) &= \lambda_1^*(t_{2-}) - \mu_1^* \theta, \\
\lambda_2^*(t_{2+}) &= \lambda_2^*(t_{2-}) - \mu_0^* + \mu_1^* \theta, \\
\lambda_3^*(t_{2+}) &= \lambda_3^*(t_{2-})
\end{aligned}
\tag{5.22}
$$

The above results show that the third Lagrange multiplier, λ_3, does not experience a jump discontinuity when temperature constraint activity changes. Moreover, the fact that the Lagrange multiplier λ_1, switches from a negative value to a positive value when the upper battery temperature bound becomes inactive suggests that μ_1 equals zero at that particular moment of transition.

Altogether, the above analyses point to a **switching** optimal thermal battery testing procedure. The policy switches between two linear systems, both of them dynamically unstable. When the battery cell temperature constraints are inactive, the rate at which the optimal policy navigates the corresponding interior-optimal but unstable solution arc depends on the Pareto weight, α. When battery temperature hits either an upper or lower bound, an instantaneous co-state jump occurs. In order for the battery to remain for a nonzero amount of time on either the upper or lower temperature bound, the temperatures

of both the test chamber and battery cell must be equal when that bound is hit. Only a finite amount of additional (Fisher) information can be gathered while one of the battery cell temperature bounds is active, regardless of how long the battery cell lingers at that bound. Finally, departure from a state-constrained solution arc occurs when the first co-state variable, λ_1, switches sign. The dynamics of this co-state variable, over the course of the constrained solution arc, are unstable.

5.5 Numerical Solution of the Battery Test Trajectory Optimization Problem

This section presents a dynamic programming-based numerical solution of the battery test trajectory optimization problem in Eq. (5.9). The only constraint applied for this problem is the constraint on cell temperature $x_2 \in [-10, 50] \circ C$. The mesh size for the ambient temperature x_1 is intentionally bigger than the limits of the battery temperature to make sure that the DP solution is not affected by a artificial numerical constraint on x_1. Therefore $x_1 \in [-15, 55] \circ C$. Also $u \in [-3/60, 3/60] \circ C/sec$. The time step for executing dynamic programming is 60 seconds which is 24% of the battery's thermal time constant θ^{-1}.

The Pontryagin analysis presented earlier suggests that the solution for $u(t)$ is a switching optimal solution that makes the cell temperature migrate from one boundary on temperature to another. The DP results in Fig. (5.1) are consistent with this analysis, showing an optimal solution trajectory that oscillates between the upper and lower battery cell temperature bounds. The majority of the test cycle time involves switching between

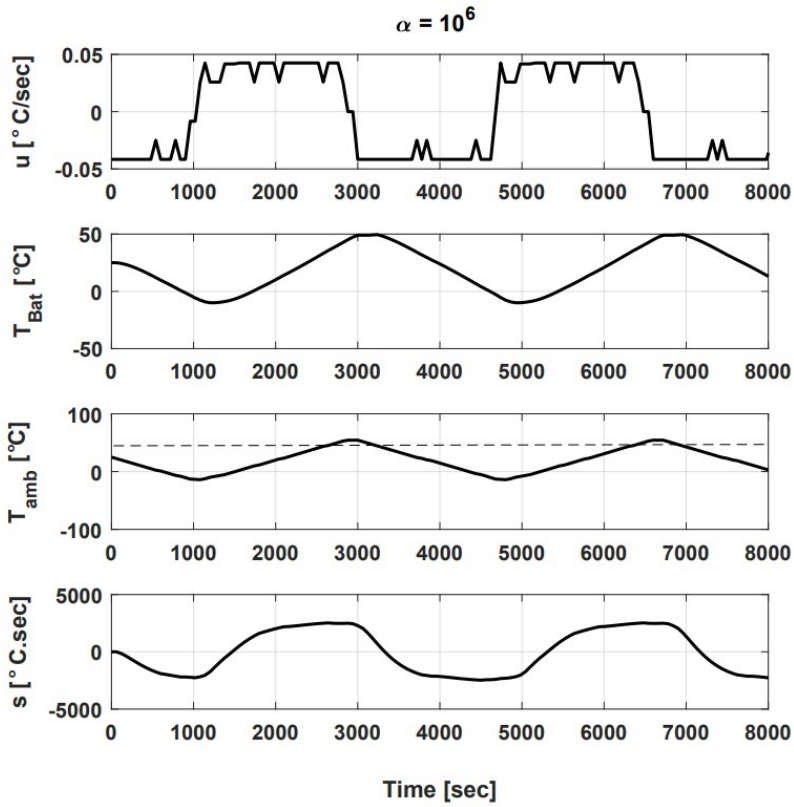

Figure 5.1: DP for $\alpha = 10^6$.

these temperature bounds as opposed to adhering to one of the bounds: an observation that is consistent with the limited information-theoretic value of adhering to these bounds. This is true for different values of the Pareto weight, as seen in Fig. (1-2). Changing the Pareto weight, α, has an impact on the resulting solution trajectory, but this impact is fairly small, at least for values of α in the range of 10^3 to 10^6, as shown in Fig. (3). Increasing the value of α increases the optimization cost/penalty associated with control actuation. Fig. (3) shows a slight slowdown of the thermal cycling trajectory in association with this heavier penalization of control actuation.

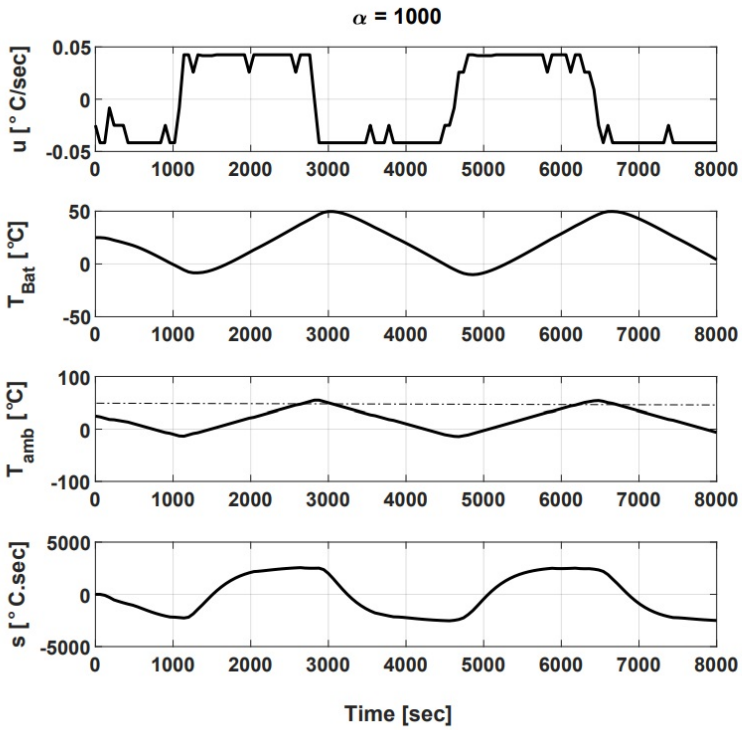

Figure 5.2: DP for $\alpha = 1000$.

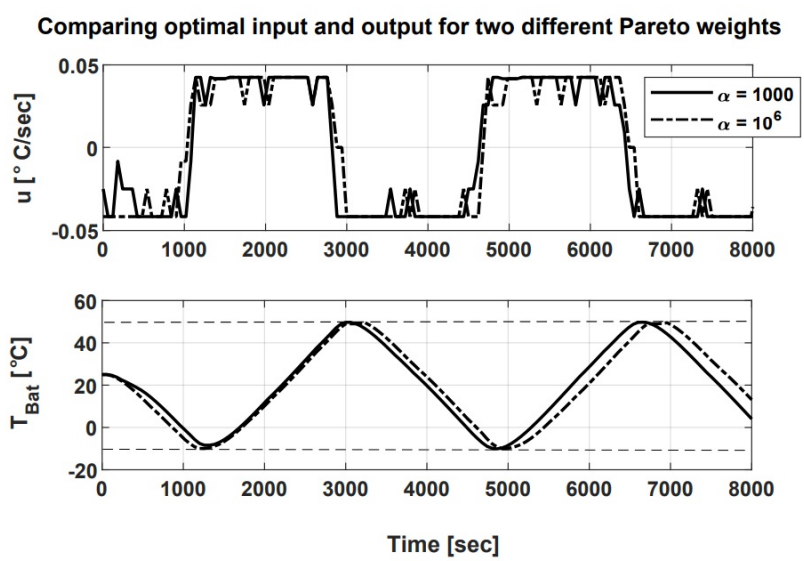

Figure 5.3: Comparing DP results for two different $\alpha = 10^6$ and $\alpha = 1000$.

5.6 Conclusion

This chapter presents a Pontryagin-based analysis to obtain insights into the structure of the optimal input solution trajectory for maximizing Fisher identifiability of lithium ion battery thermal parameter. Our analysis reveals that the optimal solution trajectory switches between two sets of solution arcs, where the battery cell temperature bounds are either active or inactive. Both sets of solution arcs are governed by unstable linear and time-invariant dynamics. Moreover, the constrained solution arc can only generate a finite additional amount of (Fisher) information, regardless of how long the test lingers on this solution arc.

Chapter 6: The Dissertation's Conclusions and Outcomes

In this chapter we summarize the main conclusions and results from five bodies of work in this dissertation for analysing and optimizing input trajectories for parameter identifiability in multi-compartment dynamic system models. This dissertation focuses on the following questions for biomedical applications and electrochemical batteries: (i) How accurately can one estimate the state variables and parameters of a dynamic system from input/output data? (ii) How does the value of the input to a dynamic system impact its observability and/or identifiability? (iii) What is the structure and shape of the optimal input for maximizing identifiability?

The research in this dissertation builds on insights from the existing literature on practical identifiability analysis. The focus of this dissertation is on Fisher Information Matrix and Cramér-Rao theoretical bounds on the best-achievable estimation accuracy. Particularly, the dissertation uses the Pontryagin Minimum Principle method to gain insights into the trajectory of the optimized input for maximizing identifiability for the first time in the literature. From a fundamental perspective, the main contributions of this work are threefold:

- First, Fisher analysis helps show that the parameter identifiability can be problematic for many dynamic systems. While this identifiability challenge is well-

described in the literature, its implications within contexts such as "third lung" gas exchange dynamics, drug-resistant cancer dynamics, and lithium-sulfur battery electrochemical dynamics, are not well-characterized. The dissertation examines theoretical bounds on parameter identifiability of (i) the CO_2 gas transport in the "thirs lung" ventilation for a hypercarbic test animal along the design and development of the data aquisition and control unit for the "third lung" setup [154], (ii) drug-resistant cancerous cells initial population and growth rates [114, 152], (iii) and a novel contribution to the lithium-sulfur electrochemical model parameters and initial states.

- Second, the above theoretical identifiability bounds are input-dependent. Therefore, the precise shape of a system's input trajectory has the potential to either improve or worsen identifiability substantially. Using Fisher analysis, one can analyze the specific input conditions for which identifiability is particularly poor, for problems such as drug resistance estimation in cancerous tumors [155].

- Third, knowing that identifiability in many dynamic systems is very poor, and at the same time very strongly input dependent, we examine optimizing the identifiability of dynamic systems parameters. By analysing the optimization problem we try to figure out conditions under which the shape of input can be improved, and what the structure of that input can be for identifiability. To fulfill this contribution, for the first time in literature, we examine the structure of optimal input trajectory using the Pontryagin minimum principle for maximizing thermal parameter identifiability of a lithium-ion battery[18].

Bibliography

[1] Sette Diop and Michel Fliess. Nonlinear observability, identifiability, and persistent trajectories. In *[1991] Proceedings of the 30th IEEE Conference on Decision and Control*, pages 714–719. IEEE, 1991.

[2] Lennart Ljung and Torkel Glad. On global identifiability for arbitrary model parametrizations. *Automatica*, 30(2):265–276, 1994.

[3] Antonio Anzueto, Fernando Frutos-Vivar, Andres Esteban, Inmaculada Alía, Laurent Brochard, Thomas Stewart, Salvador Benito, Martin J Tobin, Jose Elizalde, Fernando Palizas, et al. Incidence, risk factors and outcome of barotrauma in mechanically ventilated patients. *Intensive care medicine*, 30(4):612–619, 2004.

[4] Silvana F Marasco, George Lukas, Michael McDonald, James McMillan, and Benno Ihle. Review of ecmo (extra corporeal membrane oxygenation) support in critically ill adult patients. *Heart, Lung and Circulation*, 17:S41–S47, 2008.

[5] Deirdre A Murphy, Lisen E Hockings, Robert K Andrews, Cecile Aubron, Elizabeth E Gardiner, Vincent A Pellegrino, and Amanda K Davis. Extracorporeal membrane oxygenation—hemostatic complications. *Transfusion medicine reviews*, 29 (2):90–101, 2015.

[6] Brett Cullis, Mohamed Abdelraheem, Georgi Abrahams, Andre Balbi, Dinna N Cruz, Yaacov Frishberg, Vera Koch, Mignon McCulloch, Alp Numanoglu, Peter Nourse, et al. Peritoneal dialysis for acute kidney injury. *Peritoneal dialysis international*, 34(5):494–517, 2014.

[7] George P Biro, Pierre Blais, and Arthur L Rosen. Perfluorocarbon blood substitutes. *Critical reviews in oncology/hematology*, 6(4):311–374, 1987.

[8] Steven G Kramer, David Hwang, Gholam A Peyman, Joel A Schulman, and Brian Sullivan. Perfluorocarbon liquids in ophthalmology. *Survey of ophthalmology*, 39 (5):375–395, 1995.

[9] Michael M Gottesman. Mechanisms of cancer drug resistance. *Annual review of medicine*, 53(1):615–627, 2002.

[10] Joel Forman, Jeffrey Stein, and Hosam Fathy. Optimization of dynamic battery paramter characterization experiments via differential evolution. In *2013 American Control Conference*, pages 867–874. IEEE, 2013.

[11] Michael J Rothenberger, Joel Anstrom, Sean Brennan, and Hosam K Fathy. Maximizing parameter identifiability of an equivalent-circuit battery model using optimal periodic input shaping. In *ASME 2014 Dynamic Systems and Control Conference*. American Society of Mechanical Engineers Digital Collection, 2014.

[12] Michael J Rothenberger, Donald J Docimo, Mohammad Ghanaatpishe, and Hosam K Fathy. Genetic optimization and experimental validation of a test cycle that maximizes parameter identifiability for a li-ion equivalent-circuit battery model. *Journal of Energy Storage*, 4:156–166, 2015.

[13] Ji Liu, Michael Rothenberger, Sergio Mendoza, Partha Mishra, Yun-sik Jung, and Hosam K Fathy. Can an identifiability-optimizing test protocol improve the robustness of subsequent health-conscious lithium-ion battery control? an illustrative case study. In *2016 American Control Conference (ACC)*, pages 6320–6325. IEEE, 2016.

[14] Sergio Mendoza, Michael Rothenberger, Ji Liu, and Hosam K Fathy. Maximizing parameter identifiability of a combined thermal and electrochemical battery model via periodic current input optimization. *IFAC-PapersOnLine*, 50(1):7314–7320, 2017.

[15] Saehong Park, Dylan Kato, Zach Gima, Reinhardt Klein, and Scott Moura. Optimal experimental design for parameterization of an electrochemical lithium-ion battery model. *Journal of The Electrochemical Society*, 165(7):A1309, 2018.

[16] Andrea Pozzi, Gabriele Ciaramella, Krishnakumar Gopalakrishnan, Stefan Volkwein, and Davide M Raimondo. Optimal design of experiment for parameter estimation of a single particle model for lithiumion batteries. In *2018 IEEE Conference on Decision and Control (CDC)*, pages 6482–6487. IEEE, 2018.

[17] Andrea Pozzi, Xiangzhong Xie, Davide M Raimondo, and René Schenkendorf. Global sensitivity methods for design of experiments in lithium-ion battery context. *arXiv preprint arXiv:2004.09668*, 2020.

[18] Mahsa Doosthosseini and Hosam K Fathy. On the structure of the optimal input for maximizing lithium-ion battery thermal parameter identifiability. In *2020 American Control Conference (ACC)*, pages 379–385. IEEE, 2020.

[19] William S Levine. *The control handbook*. CRC press, 1996.

[20] Thomas L Vincent and Walter J Grantham. *Nonlinear and optimal control systems*. John Wiley & Sons, 1997.

[21] Hongyu Miao, Xiaohua Xia, Alan S Perelson, and Hulin Wu. On identifiability of nonlinear ode models and applications in viral dynamics. *SIAM review*, 53(1): 3–39, 2011.

[22] Milena Anguelova. *Observability and identifiability of nonlinear systems with applications in biology*. Chalmers Tekniska Hogskola (Sweden), 2007.

[23] Claudio Cobelli and Giorgio Romanin-Jacur. Controllability, observability and structural identifiability of multi input and multi output biological compartmental systems. *IEEE Transactions on Biomedical Engineering*, (2):93–100, 1976.

[24] Ror Bellman and Karl Johan Åström. On structural identifiability. *Mathematical biosciences*, 7(3-4):329–339, 1970.

[25] M Grewal and Keith Glover. Identifiability of linear and nonlinear dynamical systems. *IEEE Transactions on automatic control*, 21(6):833–837, 1976.

[26] Hannu Pohjanpalo. System identifiability based on the power series expansion of the solution. *Mathematical biosciences*, 41(1-2):21–33, 1978.

[27] Eric Walter and Yves Lecourtier. Unidentifiable compartmental models: what to do? *Mathematical biosciences*, 56(1-2):1–25, 1981.

[28] Michael J Chappell and Keith R Godfrey. Structural identifiability of the parameters of a nonlinear batch reactor model. *Mathematical Biosciences*, 108(2):241–251, 1992.

[29] Lennart Ljung. Convergence analysis of parametric identification methods. *IEEE transactions on automatic control*, 23(5):770–783, 1978.

[30] Ljung Lennart. System identification: theory for the user. *PTR Prentice Hall, Upper Saddle River, NJ*, pages 1–14, 1999.

[31] Andrea Saltelli, Karen Chan, M Scott, et al. Sensitivity analysis. probability and statistics series. *John and Wiley & Sons, New York*, 2000.

[32] Maria Rodriguez-Fernandez, Jose A Egea, and Julio R Banga. Novel metaheuristic for parameter estimation in nonlinear dynamic biological systems. *BMC bioinformatics*, 7(1):483, 2006.

[33] Michael J Rothenberger. Optimal input shaping for fisher identifiability of control-oriented lithium-ion battery models. 2016.

[34] J. P. Norton. *An Introduction to Identification*. Dover Publications, Inc., Mineola, 1st edition, 1986.

[35] G.C. Goodwin and R.L. Payne. *Dynamic System Identification: Experiment Design and Data Analysis*. Academic Press, New York, 1977.

[36] T. M. Cover and J. A. Thomas. *Elements of Information Theory*. John Wiley and Songs, Hoboken, 2nd edition, 2006.

[37] Efe Eworuke, Jacqueline M Major, and Lydia I Gilbert McClain. National incidence rates for acute respiratory distress syndrome (ards) and ards cause-specific factors in the united states (2006–2014). *Journal of critical care*, 47:192–197, 2018.

[38] Y Aissaoui, I En-Nafaa, K Chkoura, M Boughalem, and N Drissi Kamili. Pneumomediastinum: an aspect of pulmonary barotrauma during mechanical ventilation of acute respiratory distress syndrome. *Revue de pneumologie clinique*, 70(3):177–180, 2014.

[39] Mohamed Boussarsar, Guillaume Thierry, Samir Jaber, Françoise Roudot-Thoraval, François Lemaire, and Laurent Brochard. Relationship between ventilatory settings and barotrauma in the acute respiratory distress syndrome. *Intensive care medicine*, 28(4):406–413, 2002.

[40] R Bruce Gammon, Myung S Shin, and Scott E Buchalter. Pulmonary barotrauma in mechanical ventilation: patterns and risk factors. *Chest*, 102(2):568–572, 1992.

[41] R Bruce Gammon, Myung S Shin, RH Groves Jr, J Michael Hardin, Chuanchieh Hsu, and Scott E Buchalter. Clinical risk factors for pulmonary barotrauma: a multivariate analysis. *American journal of respiratory and critical care medicine*, 152(4):1235–1240, 1995.

[42] Vinod Mishra, Jan L Svennevig, Jan F Bugge, Sølvi Andresen, Agnete Mathisen, Harald Karlsen, Ishtiaq Khushi, and Terje P Hagen. Cost of extracorporeal membrane oxygenation: evidence from the rikshospitalet university hospital, oslo, norway. *European journal of cardio-thoracic surgery*, 37(2):339–342, 2010.

[43] Jean G Riess. Understanding the fundamentals of perfluorocarbons and perfluorocarbon emulsions relevant to in vivo oxygen delivery. *Artificial cells, blood substitutes, and biotechnology*, 33(1):47–63, 2005.

[44] Camila Irene Castro and Juan Carlos Briceno. Perfluorocarbon-based oxygen carriers: review of products and trials. *Artificial organs*, 34(8):622–634, 2010.

[45] Ivo P Torres Filho. Mini-review: Perfluorocarbons, oxygen transport, and microcirculation in low flow states: in vivo and in vitro studies. *Shock*, 52(1S):19–27, 2019.

[46] Jonathan S Jahr, Nicole R Guinn, David R Lowery, Linda Shore-Lesserson, and Aryeh Shander. Blood substitutes and oxygen therapeutics: a review. *Anesthesia & Analgesia*, 132(1):119–129, 2020.

[47] Bruce D Spiess. Perfluorocarbon gas transport: an overview of medical history with yet unrealized potentials. *Shock*, 52(1S):7–12, 2019.

[48] Christopher Bialas, Christopher Moser, and Carrie A Sims. Artificial oxygen carriers and red blood cell substitutes: A historic overview and recent developments toward military and clinical relevance. *Journal of Trauma and Acute Care Surgery*, 87(1S):S48–S58, 2019.

[49] Claudia S Cohn and Melissa M Cushing. Oxygen therapeutics: perfluorocarbons and blood substitute safety. *Critical care clinics*, 25(2):399–414, 2009.

[50] Scott E Curtis, Bradley P Fuhrman, Donna F Howland, Maria DeFrancisis, and ETSURO K Motoyama. Cardiac output during liquid (perfluorocarbon) breathing in newborn piglets. *Critical care medicine*, 19(2):225–230, 1991.

[51] Ronald B Hirschl, Thomas Pranikoff, Constance Wise, Michael C Overbeck, Paul Gauger, Robert J Schreiner, Ronald Dechert, and Robert H Bartlett. Initial experience with partial liquid ventilation in adult patients with the acute respiratory distress syndrome. *Jama*, 275(5):383–389, 1996.

[52] Corinne Lowe Leach, Jay S Greenspan, S David Rubenstein, Thomas H Shaffer, Marla R Wolfson, J Craig Jackson, Robert DeLemos, and Bradley P Fuhrman. Partial liquid ventilation with perflubron in premature infants with severe respiratory distress syndrome. *New England Journal of Medicine*, 335(11):761–767, 1996.

[53] Ronald B Hirschl, Steven Conrad, Roger Kaiser, Joseph B Zwischenberger, Robert H Bartlett, Frank Booth, and Victor Cardenas. Partial liquid ventilation in adult patients with ards: a multicenter phase i-ii trial. adult plv study group. *Annals of surgery*, 228(5):692, 1998.

[54] Thomas H Shaffer, Marla R Wolfson, and Leland C Clark Jr. Liquid ventilation. *Pediatric pulmonology*, 14(2):102–109, 1992.

[55] Marla R Wolfson and Thomas H Shaffer. Liquid ventilation: an adjunct for respiratory management. *Pediatric Anesthesia*, 14(1):15–23, 2004.

[56] Kimberly S Staffey, Raghuveer Dendi, Leonard A Brooks, Andrew M Pretorius, Laynez W Ackermann, KD Zamba, Eric Dickson, and Richard E Kerber. Liquid ventilation with perfluorocarbons facilitates resumption of spontaneous circulation in a swine cardiac arrest model. *Resuscitation*, 78(1):77–84, 2008.

[57] Suman Sarkar, Anil Paswan, and S Prakas. Liquid ventilation. *Anesthesia, essays and researches*, 8(3):277, 2014.

[58] Ronald B Hirschl, Martin Croce, Dennis Gore, Herbert Wiedemann, KEN Davis, Joseph Zwischenberger, and Robert H Bartlett. Prospective, randomized, controlled pilot study of partial liquid ventilation in adult acute respiratory distress syndrome. *American journal of respiratory and critical care medicine*, 165(6): 781–787, 2002.

[59] Shamus R Carr, Joshua P Cantor, Atul S Rao, Thiru V Lakshman, Joshua E Collins, and Joseph S Friedberg. Peritoneal perfusion with oxygenated perfluorocarbon augments systemic oxygenation. *Chest*, 130(2):402–411, 2006.

[60] MCK Khoo, Richard E Kronauer, Kingman P Strohl, and Arthur S Slutsky. Factors inducing periodic breathing in humans: a general model. *Journal of applied physiology*, 53(3):644–659, 1982.

[61] MCK Khoo and RE Kronauer. Estimation of cardiopulmonary parameters using quasi-optimal inputs. In *1983 American Control Conference*, pages 46–51. IEEE, 1983.

[62] Jerry J Batzel, Franz Kappel, Daniel Schneditz, and Hien T Tran. *Cardiovascular and respiratory systems: modeling, analysis, and control*. SIAM, 2007.

[63] Zuckerman L. Goldstick TK, Ciuryla VT. Diffusion of oxygen in plasma and blood. *Advances in experimental medicine and biology*, 75:183–190, 1976.

[64] EL Seames, JW Moncrief, and RP Popovich. A distributed model of fluid and mass transfer in peritoneal dialysis. *American Journal of Physiology-Regulatory, Integrative and Comparative Physiology*, 258(4):R958–R972, 1990.

[65] MCl Khoo, Allan Gottschalk, and ALLAN I Pack. Sleep-induced periodic breathing and apnea: a theoretical study. *Journal of Applied Physiology*, 70(5):2014–2024, 1991.

[66] Pierre Yves Durand, Jacques Chanliau, Joel Gamberoni, Dominique Hestin, and Michele Kessler. Apd: clinical measurement of the maximal acceptable intraperitoneal volume. *Advances in peritoneal dialysis*, 10:63–63, 1994.

[67] Agnès Dejardin, Annie Robert, and Eric Goffin. Intraperitoneal pressure in pd patients: relationship to intraperitoneal volume, body size and pd-related complications. *Nephrology Dialysis Transplantation*, 22(5):1437–1444, 2007.

[68] B Buszewski. K [e ogonek] sy m.; ligor t.; amann a. *Human exhaled air analytics: biomarkers of diseases. Biomed. Chromatogr*, 21:553–566, 2007.

[69] Liana Hatoum. Diffusion modeling and device development for peritoneal membrane oxygenation. 2016.

[70] Roland N Pittman. Regulation of tissue oxygenation. In *Colloquium series on integrated systems physiology: from molecule to function*, volume 3, pages 1–100. Morgan & Claypool Life Sciences, 2011.

[71] Yannick J Heintz. *Carbon dioxide capture from fuel gas streams under elevated pressures and temperatures using novel physical solvents*. PhD thesis, University of Pittsburgh, 2012.

[72] Alona Ben-Tal. Simplified models for gas exchange in the human lungs. *Journal of theoretical biology*, 238(2):474–495, 2006.

[73] Azad Ghaffari. dspace and real-time interface in simulink. *San Diego State University*, 2012.

[74] Devendra Potnuru, Saibabu Ch, et al. Design and implementation methodology for rapid control prototyping of closed loop speed control for bldc motor. *Journal of Electrical Systems and Information Technology*, 5(1):99–111, 2018.

[75] Elsa Hansen, Robert J Woods, and Andrew F Read. How to use a chemotherapeutic agent when resistance to it threatens the patient. *PLoS biology*, 15(2):e2001110, 2017.

[76] John A Jacquez and Peter Greif. Numerical parameter identifiability and estimability: Integrating identifiability, estimability, and optimal sampling design. *Mathematical Biosciences*, 77(1-2):201–227, 1985.

[77] Genevieve Housman, Shannon Byler, Sarah Heerboth, Karolina Lapinska, Mckenna Longacre, Nicole Snyder, and Sibaji Sarkar. Drug resistance in cancer: an overview. *Cancers*, 6(3):1769–1792, 2014.

[78] HARISH KADKOL, VIKAS JAIN, and AMIT B PATIL. Multi drug resistance in cancer therapy-an overview. *J. Crit. Rev*, 6(6):1–6, 2019.

[79] Nikolaos I Stilianakis, Alan S Perelson, and Frederick G Hayden. Emergence of drug resistance during an influenza epidemic: insights from a mathematical model. *Journal of Infectious Diseases*, 177(4):863–873, 1998.

[80] Federica Eduati, Victoria Doldàn-Martelli, Bertram Klinger, Thomas Cokelaer, Anja Sieber, Fiona Kogera, Mathurin Dorel, Mathew J Garnett, Nils Blüthgen, and Julio Saez-Rodriguez. Drug resistance mechanisms in colorectal cancer dissected with cell type–specific dynamic logic models. *Cancer research*, 77(12): 3364–3375, 2017.

[81] Orit Lavi, Michael M Gottesman, and Doron Levy. The dynamics of drug resistance: a mathematical perspective. *Drug Resistance Updates*, 15(1-2):90–97, 2012.

[82] Xiaoqiang Sun and Bin Hu. Mathematical modeling and computational prediction of cancer drug resistance. *Briefings in bioinformatics*, 19(6):1382–1399, 2018.

[83] Larry Norton. A gompertzian model of human breast cancer growth. *Cancer research*, 48(24 Part 1):7067–7071, 1988.

[84] Lisette G De Pillis and Ami Radunskaya. A mathematical tumor model with immune resistance and drug therapy: an optimal control approach. *Computational and Mathematical Methods in Medicine*, 3(2):79–100, 2001.

[85] SC Ferreira Jr, ML Martins, and MJ Vilela. Reaction-diffusion model for the growth of avascular tumor. *Physical Review E*, 65(2):021907, 2002.

[86] Michael Bouvet, Jinwei Wang, Stephanie R Nardin, Rounak Nassirpour, Meng Yang, Eugene Baranov, Ping Jiang, AR Moossa, and Robert M Hoffman. Real-time optical imaging of primary tumor growth and multiple metastatic events in a pancreatic cancer orthotopic model. *Cancer research*, 62(5):1534–1540, 2002.

[87] Stephanie Alexander, Gudrun E Koehl, Markus Hirschberg, Edward K Geissler, and Peter Friedl. Dynamic imaging of cancer growth and invasion: a modified skin-fold chamber model. *Histochemistry and cell biology*, 130(6):1147–1154, 2008.

[88] Pamela K Kreeger and Douglas A Lauffenburger. Cancer systems biology: a network modeling perspective. *Carcinogenesis*, 31(1):2–8, 2010.

[89] Marios M Hadjiandreou and Georgios D Mitsis. Mathematical modeling of tumor growth, drug-resistance, toxicity, and optimal therapy design. *IEEE Transactions on Biomedical Engineering*, 61(2):415–425, 2013.

[90] Ignacio A Rodriguez-Brenes, Natalia L Komarova, and Dominik Wodarz. Tumor growth dynamics: insights into evolutionary processes. *Trends in ecology & evolution*, 28(10):597–604, 2013.

[91] Sébastien Benzekry, Clare Lamont, Afshin Beheshti, Amanda Tracz, John ML Ebos, Lynn Hlatky, and Philip Hahnfeldt. Classical mathematical models for description and prediction of experimental tumor growth. *PLoS Comput Biol*, 10(8): e1003800, 2014.

[92] Li-Gang Lin and Ming Xin. Guaranteed continuity and computational improvement in sdre controllers for cancer treatment analysis. *Journal of Dynamic Systems, Measurement, and Control*, 142(4), 2020.

[93] RB Martin, ME Fisher, RF Minchin, and KL Teo. Optimal control of tumor size used to maximize survival time when cells are resistant to chemotherapy. *Mathematical biosciences*, 110(2):201–219, 1992.

[94] Rory Martin and KL Teo. *Optimal control of drug administration in cancer chemotherapy*. World Scientific, 1994.

[95] Luis A Fernández and Cecilia Pola. Catalog of the optimal controls in cancer chemotherapy for the gompertz model depending on pk/pd and the integral constraint. *Discrete & Continuous Dynamical Systems-B*, 19(6):1563, 2014.

[96] Luis A Fernandez and Cecilia Pola. Optimal control problems for the gompertz model under the norton-simon hypothesis in chemotherapy. *Discrete & Continuous Dynamical Systems-B*, 24(6):2577, 2019.

[97] Galina Lebedeva, Anatoly Sorokin, Dana Faratian, Peter Mullen, Alexey Goltsov, Simon P Langdon, David J Harrison, and Igor Goryanin. Model-based global sensitivity analysis as applied to identification of anti-cancer drug targets and biomarkers of drug resistance in the erbb2/3 network. *European Journal of Pharmaceutical Sciences*, 46(4):244–258, 2012.

[98] A Raue, C Kreutz, T Maiwald, Ursula Klingmüller, and J Timmer. Addressing parameter identifiability by model-based experimentation. *IET systems biology*, 5 (2):120–130, 2011.

[99] Marisa C Eisenberg and Harsh V Jain. A confidence building exercise in data and identifiability: Modeling cancer chemotherapy as a case study. *Journal of theoretical biology*, 431:63–78, 2017.

[100] Hulin Wu, Haihong Zhu, Hongyu Miao, and Alan S Perelson. Parameter identifiability and estimation of hiv/aids dynamic models. *Bulletin of mathematical biology*, 70(3):785–799, 2008.

[101] Xiaohua Xia and Claude H Moog. Identifiability of nonlinear systems with application to hiv/aids models. *IEEE transactions on automatic control*, 48(2):330–336, 2003.

[102] Elsa Hansen Mahsa Doosthosseini and Hosam K. Fathy. On the accuracy of drug-resistant cell population estimation from total cancer size measurements. 5(2): 120–130, 2019.

[103] RB Martin, ME Fisher, RF Minchin, and KL Teo. A mathematical model of cancer chemotherapy with an optimal selection of parameters. *Mathematical biosciences*, 99(2):205–230, 1990.

[104] Mark Wild and Gregory J Offer. *Lithium-Sulfur Batteries*. John Wiley & Sons, 2019.

[105] H Yanin and E Peled. Low-rate lithium/sulfur organic battery. In *Proc.-Electrochem. Soc.;(United States)*, volume 84. Department of Chemistry, Tel-Aviv University, Tel-Aviv, 1983.

[106] Arumugam Manthiram, Yongzhu Fu, Sheng-Heng Chung, Chenxi Zu, and Yu-Sheng Su. Rechargeable lithium–sulfur batteries. *Chemical reviews*, 114(23): 11751–11787, 2014.

[107] Min-Kyu Song, Elton J Cairns, and Yuegang Zhang. Lithium/sulfur batteries with high specific energy: old challenges and new opportunities. *Nanoscale*, 5(6):2186–2204, 2013.

[108] Abbas Fotouhi, Daniel J Auger, Laura O'Neill, Tom Cleaver, and Sylwia Walus. Lithium-sulfur battery technology readiness and applications—a review. *Energies*, 10(12):1937, 2017.

[109] Zhiyong Zhang, Yanqing Lai, Zhian Zhang, Kai Zhang, and Jie Li. Al2o3-coated porous separator for enhanced electrochemical performance of lithium sulfur batteries. *Electrochimica Acta*, 129:55–61, 2014.

[110] Weikun Wang, You Wang, Yaqin Huang, Chongjun Huang, Zhongbao Yu, Hao Zhang, Anbang Wang, and Keguo Yuan. The electrochemical performance of lithium–sulfur batteries with liclo 4 dol/dme electrolyte. *Journal of Applied Electrochemistry*, 40(2):321–325, 2010.

[111] Demir-cakan Rezan. *Li-S Batteries: The Challenges, Chemistry, Materials, and Future Perspectives*. # N/A, 2017.

[112] Bolan Gan, Kaikai Tang, Yali Chen, Dandan Wang, Na Wang, Wenxian Li, Yong Wang, Hao Liu, and Guoxiu Wang. Concrete-like high sulfur content cathodes with enhanced electrochemical performance for lithium-sulfur batteries. *Journal of Energy Chemistry*, 42:174–179, 2020.

[113] Sergio Mendoza, Michael Rothenberger, Alison Hake, and Hosam Fathy. Optimization and experimental validation of a thermal cycle that maximizes entropy coefficient fisher identifiability for lithium iron phosphate cells. *Journal of Power Sources*, 308:18–28, 2016.

[114] Mahsa Doosthosseini and Hosam Fathy. Combined state and parameter identifiability for a model of drug-resistant cancer dynamics. *Journal of Dynamic Systems, Measurement, and Control*, 2021.

[115] VS Kolosnitsyn, EV Kuzmina, EV Karaseva, and SE Mochalov. A study of the electrochemical processes in lithium–sulphur cells by impedance spectroscopy. *Journal of Power Sources*, 196(3):1478–1482, 2011.

[116] Zhaofeng Deng, Zhian Zhang, Yanqing Lai, Jin Liu, Jie Li, and Yexiang Liu. Electrochemical impedance spectroscopy study of a lithium/sulfur battery: modeling and analysis of capacity fading. *Journal of The Electrochemical Society*, 160(4): A553–A558, 2013.

[117] Vaclav Knap, Daniel-Ioan Stroe, Remus Teodorescu, Maciej Swierczynski, and Tiberiu Stanciu. Electrical circuit models for performance modeling of lithium-sulfur batteries. In *2015 IEEE Energy Conversion Congress and Exposition (ECCE)*, pages 1375–1381. IEEE, 2015.

[118] Karsten Propp, Monica Marinescu, Daniel J Auger, Laura O'Neill, Abbas Fotouhi, Karthik Somasundaram, Gregory J Offer, Geraint Minton, Stefano Longo, Mark Wild, et al. Multi-temperature state-dependent equivalent circuit discharge model for lithium-sulfur batteries. *Journal of Power Sources*, 328:289–299, 2016.

[119] Karthikeyan Kumaresan, Yuriy Mikhaylik, and Ralph E White. A mathematical model for a lithium–sulfur cell. *Journal of The Electrochemical Society*, 155(8): A576–A582, 2008.

[120] David N Fronczek and Wolfgang G Bessler. Insight into lithium–sulfur batteries: Elementary kinetic modeling and impedance simulation. *Journal of power sources*, 244:183–188, 2013.

[121] Andreas F Hofmann, David N Fronczek, and Wolfgang G Bessler. Mechanistic modeling of polysulfide shuttle and capacity loss in lithium–sulfur batteries. *Journal of Power Sources*, 259:300–310, 2014.

[122] YX Ren, TS Zhao, M Liu, P Tan, and YK Zeng. Modeling of lithium-sulfur batteries incorporating the effect of li2s precipitation. *Journal of Power Sources*, 336: 115–125, 2016.

[123] Petru Andrei, Chao Shen, and Jim P Zheng. Theoretical and experimental analysis of precipitation and solubility effects in lithium-sulfur batteries. *Electrochimica Acta*, 284:469–484, 2018.

[124] Timo Danner and Arnulf Latz. On the influence of nucleation and growth of s8 and li2s in lithium-sulfur batteries. *Electrochimica Acta*, 322:134719, 2019.

[125] Abbas Fotouhi, Daniel J Auger, Karsten Propp, Stefano Longo, Rajlakshmi Purkayastha, Laura O'Neill, and Sylwia Waluś. Lithium–sulfur cell equivalent circuit network model parameterization and sensitivity analysis. *IEEE Transactions on Vehicular Technology*, 66(9):7711–7721, 2017.

[126] Abbas Fotouhi, Daniel J Auger, Karsten Propp, and Stefano Longo. Lithium–sulfur battery state-of-charge observability analysis and estimation. *IEEE Transactions on Power Electronics*, 33(7):5847–5859, 2017.

[127] Karsten Propp, Daniel J Auger, Abbas Fotouhi, Monica Marinescu, Vaclav Knap, and Stefano Longo. Improved state of charge estimation for lithium-sulfur batteries. *Journal of Energy Storage*, 26:100943, 2019.

[128] Monica Marinescu, Teng Zhang, and Gregory J Offer. A zero dimensional model of lithium–sulfur batteries during charge and discharge. *Physical Chemistry Chemical Physics*, 18(1):584–593, 2016.

[129] Teng Zhang, Monica Marinescu, Laura O'Neill, Mark Wild, and Gregory Offer. Modeling the voltage loss mechanisms in lithium–sulfur cells: the importance of electrolyte resistance and precipitation kinetics. *Physical Chemistry Chemical Physics*, 17(35):22581–22586, 2015.

[130] Mahmoudreza Ghaznavi and P Chen. Sensitivity analysis of a mathematical model of lithium–sulfur cells part i: Applied discharge current and cathode conductivity. *Journal of power sources*, 257:394–401, 2014.

[131] M. Ghaznavi and P. Chen,. Sensitivity analysis of a mathematical model of lithium–sulfur cells: Part ii: Precipitation reaction kinetics and sulfur content. *Journal of Power Sources*, 257:402–411, 2014.

[132] Mahmoudreza Ghaznavi and P Chen. Analysis of a mathematical model of lithium-sulfur cells part iii: Electrochemical reaction kinetics, transport properties and charging. *Electrochimica Acta*, 137:575–585, 2014.

[133] Chu Xu, Timothy Cleary, Daiwei Wang, Guoxing Li, Christopher Rahn, Donghai Wang, Rajesh Rajamani, and Hosam K Fathy. Online state estimation for a physics-based lithium-sulfur battery model. *Journal of Power Sources*, 489:229495, 2021.

[134] Chu Xu, Timothy Cleary, Guoxing Li, Donghai Wang, and Hosam Fathy. Parameter identification and sensitivity analysis for zero-dimensional physics-based lithium-sulfur battery models. *ASME Letters in Dynamic Systems and Control*, 1 (4):041001, 2021.

[135] M Wild, L O'neill, T Zhang, R Purkayastha, G Minton, M Marinescu, and GJ Offer. Lithium sulfur batteries, a mechanistic review. *Energy & Environmental Science*, 8(12):3477–3494, 2015.

[136] Guoxing Li Donghai Wang Hosam K Fathy Chu Xu, Timothy Cleary. Parameter identification and sensitivity analysis for zero-dimensional multi-physics lithium-sulfur battery models. 2020.

[137] Jerry Chao, E Sally Ward, and Raimund J Ober. Fisher information theory for parameter estimation in single molecule microscopy: tutorial. *JOSA A*, 33(7): B36–B57, 2016.

[138] Thomas M Cover. *Elements of information theory*. John Wiley & Sons, 1999.

[139] John P Norton. *An introduction to identification*. Courier Corporation, 2009.

[140] Meng Guo, Godfrey Sikha, and Ralph E White. Single-particle model for a lithium-ion cell: Thermal behavior. *Journal of The Electrochemical Society*, 158(2):A122–A132, 2011.

[141] Karthikeyan Kumaresan, Godfrey Sikha, and Ralph E White. Thermal model for a li-ion cell. *Journal of the Electrochemical Society*, 155(2):A164–A171, 2008.

[142] Hossein Maleki, Said Al Hallaj, J Robert Selman, Ralph B Dinwiddie, and H Wang. Thermal properties of lithium-ion battery and components. *Journal of the Electrochemical Society*, 146(3):947–954, 1999.

[143] Ning Tian, Huazhen Fang, and Yebin Wang. Parameter identification of the nonlinear double-capacitor model for lithium-ion batteries: From the wiener perspective. In *2019 American Control Conference (ACC)*, pages 897–902. IEEE, 2019.

[144] James Marcicki, Marcello Canova, A Terrence Conlisk, and Giorgio Rizzoni. Design and parametrization analysis of a reduced-order electrochemical model of graphite/lifepo4 cells for soc/soh estimation. *Journal of Power Sources*, 237:310–324, 2013.

[145] Alexander P Schmidt, Matthias Bitzer, Árpád W Imre, and Lino Guzzella. Experiment-driven electrochemical modeling and systematic parameterization for a lithium-ion battery cell. *Journal of Power Sources*, 195(15):5071–5080, 2010.

[146] Aabhas Sharma and Hosam K Fathy. Fisher identifiability analysis for a periodically-excited equivalent-circuit lithium-ion battery model. In *2014 American Control Conference*, pages 274–280. IEEE, 2014.

[147] Liqiang Zhang, Chao Lyu, Gareth Hinds, Lixin Wang, Weilin Luo, Jun Zheng, and Kehua Ma. Parameter sensitivity analysis of cylindrical lifepo4 battery performance using multi-physics modeling. *Journal of The Electrochemical Society*, 161 (5):A762–A776, 2014.

[148] Xinfan Lin and Anna G Stefanopoulou. Analytic bound on accuracy of battery state and parameter estimation. *Journal of The Electrochemical Society*, 162(9): A1879–A1891, 2015.

[149] Hans P Geering. *Optimal control with engineering applications*. Springer, 2007.

[150] Lorenzo Serrao, Simona Onori, and Giorgio Rizzoni. Ecms as a realization of pontryagin's minimum principle for hev control. In *2009 American control conference*, pages 3964–3969. IEEE, 2009.

[151] D Bernardi, E Pawlikowski, and John Newman. A general energy balance for battery systems. *Journal of the electrochemical society*, 132(1):5–12, 1985.

[152] Mahsa Doosthosseini, Elsa Hansen, and Hosam K Fathy. On the accuracy of drug-resistant cell population estimation from total cancer size measurements. In *2019 18th European Control Conference (ECC)*, pages 343–350. IEEE, 2019.

[153] D Subbaram Naidu. *Optimal control systems*. CRC press, 2002.

[154] Mahsa Doosthosseini, Kevin R Aroom, Majid Aroom, Melissa Culligan, Warren Naselsky, Chandrasekhar Thamire, Henry W Haslach Jr, Stephen A Roller, James Richard Hughen, Joseph S Friedberg, et al. Monitoring and control system development and experimental validation for a novel extrapulmonary respiratory support setup. *arXiv preprint arXiv:2107.02902*, 2021.

[155] Mahsa Doosthosseini and Hosam Fathy. Combined state and parameter identifiability for a model of drug-resistant cancer dynamics. *Journal of Dynamic Systems, Measurement, and Control*, 143(11):111005, 2021.